ARISTOTLE UNIVERSITY OF THESSALONIKI
SCHOOL OF GEOLOGY
DEPARTMENT OF GEOLOGY

POSTGRADUATE PROGRAM “APPLIED AND ENVIRONMENTAL GEOLOGY"
FIELD OF SPECIALIZATION: “APPLIED GEOPHYSICS"

ELECTRICAL RESISTIVITY TOMOGRAPHY MEASUREMENTS IN INCLINED BOREHOLES

MASTER THESIS

TZIMA ELENI
Geologist

THESSALONIKI
2023

TZIMA ELENI
ΤΖΗΜΑ ΕΛΕΝΗ
Πτυχιούχος Γεωλόγος

ELECTRICAL RESISTIVITY TOMOGRAPHY MEASUREMENTS IN INCLINED BOREHOLES

ΔΙΑΤΑΞΕΙΣ ΗΛΕΚΤΡΙΚΗΣ ΤΟΜΟΓΡΑΦΙΑΣ ΣΕ ΚΕΚΛΙΜΕΝΕΣ ΓΕΩΤΡΗΣΕΙΣ

Υποβλήθηκε στο Τμήμα Γεωλογίας στα πλαίσια του Προγράμματος Μεταπτυχιακών Σπουδών ‘Εφαρμοσμένη και Περιβαλλοντική Γεωλογία’, Κατεύθυνση ‘Εφαρμοσμένη Γεωφυσική και Σεισμολογία’

Ημερομηνία Προφορικής Εξέτασης: 06/11/2023
Oral Examination Date: 06/11/2023

Three-member Examining Board

Professor Panagiotis Tsourlos, Supervisor
Associate Professor George Vargemezis, Advisory Committee Member
Associate Professor Grigorios Tsokas, Advisory Committee Member

Τριμελής Εξεταστική Επιτροπή

Καθηγητής Παναγιώτης Τσούρλος, Επιβλέπων
Αναπληρωτής Καθηγητής Γεώργιος Βαργεμέζης, Μέλος Τριμελούς Εξεταστικής Επιτροπής
Αναπληρωτής Καθηγητής Γρηγόριος Τσόκας, Μέλος Τριμελούς Εξεταστικής Επιτροπής

ACKNOWLEDGEMENTS

I would like to wholeheartedly thank my Supervisor, Professor Panagiotis Tsourlos, for all his support and guidance throughout my studies. He was always by my side, consulting me every step of the way. His advice was insightful and on point, allowing me to overcome all and any obstacles that challenged this thesis. Without his contribution and trust, I would not have been able to complete this master's thesis.

I also thank my professors, George Vargemezis and Grigorios Tsokas, who equipped me with valuable knowledge and practical experience by allowing me to participate in field measurements. I would also like to thank Dr. Illias Fikos and Dr. Nectaria Diamanti for the constructive advice they provided me over these two years. I am also grateful to the Ph.D. candidates Prodromos Louvaris and Konstantinos Polydoropoulos, who assisted me with the conducted field measurements.

I would also like to thank my parents. Without their moral and economic support throughout my academic years, I would not have been able to make it as far as I have. In addition, I want to thank the rest of my family for their encouragement and assistance. Finally, I would like to express my gratitude to my best friends, who were always there for me through highs and lows.

ABSTACT

This master's thesis proposes a methodology for acquiring electrical resistivity tomography measurements applied in inclined boreholes combined with a surface or a second borehole. The existence of the boreholes provides additional information to the surface measurements, and this combined investigation would benefit the findings. However, because standard resistivity arrays are not directly applicable to these arbitrarily positioned electrodes, the need to investigate alternative electrode arrays for such cases is evident. In this study, schemes for generating complete and optimized protocols can be created for these measurement arrangements.

For this purpose, an algorithm was designed in the Matrix Laboratory (MATLAB) that can produce full and optimized datasets compatible with the resistivity meters. A graphic user interface was designed to render the algorithm more comprehensible and flexible in handling. The basic concept during the development of the code was to make it as practical and manageable in the field as possible.

The algorithm was tested with numerous synthetic models with diverse geometries (i.e., different borehole's inclination, unequal spacing between borehole and surface electrodes etc.), which were created and inverted for both the full and other optimized datasets. Some of these are presented and discussed in this thesis. Laboratory experiments were also conducted to further assess the algorithm's applicability. For this purpose, a structure that simulates the surface and borehole electrodes was inserted into a water tank. Some targets with different expected resistivities were tested for the generated protocols.

Finally, it was feasible to apply this algorithm to real data. Owing to maintenance reasons, some boreholes were drilled in the walls of the Rotunda church in Thessaloniki; therefore, the opportunity to investigate the interior of the walls using the protocols produced by the mentioned algorithm was given. Since the primary purpose was not to evaluate the wall's condition but to verify the algorithm's utility, only some of the results of the investigated boreholes will be presented and discussed.

According to the results, the algorithm was deemed capable of coping with any geometry of the electrodes (borehole - surface or borehole – borehole array), and the produced protocols accurately depicted the investigated area.

ΠΕΡΙΛΗΨΗ

Σκοπός αυτής της μεταπτυχιακής εργασίας είναι να προταθεί ένας τρόπος πραγματοποίησης μετρήσεων που να μπορεί να υποστηρίζει την εφαρμογή της ηλεκτρικής τομογραφίας σε κεκλιμένες γεωτρήσεις, συνδυασμένες επιπλέον με περαιτέρω ηλεκτρόδια στην επιφάνεια ή ακόμα και σε άλλη γεώτρηση. Οι γεωτρήσεις προσφέρουν επιπλέον πληροφορία στις επιφανειακές μετρήσεις, κάνοντας τον συνδυασμό τους πιο ωφέλιμο στην ταυτοποίηση των ευρημάτων. Επειδή όμως οι διατάξεις των ηλεκτροδίων που έχουν προταθεί δεν είναι απευθείας εφαρμόσιμες σε αυτή την αυθαίρετη τοποθέτηση των ηλεκτροδίων, εμφανίζεται η ανάγκη να τροποποιηθούν. Με αυτές τις μετατροπές και με κάποιες επιπλέον παρεμβάσεις είναι δυνατό να προταθεί ένα πλήρες και κάποια βέλτιστα πρωτόκολλα για τέτοιου είδους μετρήσεις.

Για αυτό τον λόγο δημιουργήθηκε ένας αλγόριθμος, ο οποίος σχεδιάστηκε στο Matrix Laboratory (MATLAB) και παράγει πλήρη αλλά και βελτιστοποιημένα δεδομένα, τα οποία μπορούν να μετατραπούν σε πρωτόκολλα συμβατά με το όργανο μέτρησης. Για να είναι ο αλγόριθμος πιο κατανοητός και εύκολος στον χειρισμό, δημιουργήθηκαν γραφικά παράθυρα αλληλεπίδρασης χρήστη (graphic user interface windows). Κατά την διάρκεια ανάπτυξης του κώδικα, σημαντική έμφαση δόθηκε στο να είναι όσο το δυνατόν πιο πρακτικός και διαχειρίσιμος στο πεδίο.

Για να δοκιμαστεί και να αξιολογηθεί το τελικό αποτέλεσμα που παράγεται από τον κώδικα, δημιουργήθηκαν και υποβλήθηκαν στην διαδικασία της αντιστροφής, πολλά συνθετικά μοντέλα με διάφορες γεωμετρίες (π.χ. διαφορετική κλίση γεώτρησης, άνισο άνοιγμα των ηλεκτροδίων της γεώτρησης σε σχέση με της επιφάνειας κ.α.) τόσο για το πλήρες όσο και για διάφορα βελτιστοποιημένα σύνολα δεδομένων. Μερικά από αυτά παρουσιάζονται και σχολιάζονται σε αυτή την μεταπτυχιακή εργασία. Πέρα από τα συνθετικά μοντέλα, για να αξιολογηθεί περαιτέρω η εφαρμοσιμότητα του αλγόριθμου έγινε απόπειρα μέτρησης με πείραμα στο εργαστήριο. Γι' αυτό το λόγο κατασκευάστηκε μια δομή, ικανή να κρατάει σταθερά τα ηλεκτρόδια της γεώτρησης και τη επιφανείας. Αυτή η δομή εισάχθηκε σε δεξαμενή γεμάτη με νερό και στόχοι με διαφορετικές αναμενόμενες αντιστάσεις βυθίστηκαν και στερεώθηκαν ανάμεσα στα επιφανειακά ηλεκτρόδια και της γεώτρησης, για να εξακριβωθεί αν θα εντοπιζόταν από το παραγόμενο πρωτόκολλο.

Τέλος, δόθηκε η δυνατότητα να πραγματοποιηθούν μετρήσεις και σε πραγματική έρευνα. Για λόγους συντήρησης, κάποιες γεωτρήσεις διανοίχθηκαν στους τοίχους του μνημείου της εκκλησίας της Ροτόντα στην Θεσσαλονίκη, οπότε και ήταν εφικτή η διασκόπηση του εσωτερικού των τοίχων με την αξιοποίηση του εν λόγω αλγορίθμου. Παρόλα αυτά, μιας και ο βασικός σκοπός δεν ήταν καθαυτό η αξιολόγηση της κατάστασης του τοίχου, αλλά η επιβεβαίωση της λειτουργικότητας και χρησιμότητας

του αλγορίθμου, μόνο μερικές από της μελετημένες γεωτρήσεις θα παρουσιαστούν σε αυτή την εργασία.

Σε γενικές γραμμές, σύμφωνα με τα αποτελέσματα που προέκυψαν, ο αλγόριθμος είναι ικανός όχι μόνο να αναπαράγει την επιθυμητή γεωμετρία (γεώτρηση - επιφάνεια ή γεώτρηση - γεώτρηση), αλλά και να προσφέρει μια καλή εκτίμηση της υπό μελέτη περιοχής.

CONTENTS

1. PREFACE

In this master's thesis, the electrical resistivity tomography method is applied. Traditionally, the surveys occur with the electrodes placed at the ground's surface. But, due to further advances in this field, many surveys have also been conducted between perpendicular boreholes and the surface or between two parallel boreholes (cross-hole). This combined investigation is a valuable tool because the boreholes are closer to the desired target and may provide more detailed information about the area. In many cases, the drilled boreholes are not always perpendicular to the ground but may have various degrees of inclination. So, the need to provide some possible measuring protocols for borehole-surface or borehole-borehole configurations with different degrees of tilt is evident.

For this reason, and since the standard configurations are not directly applicable to this arbitrary geometry, it was attempted to create an algorithm to generate efficient protocols for the borehole-surface and borehole-borehole measurements. The developed algorithm calculates the correct positions of the electrodes depending on the borehole's inclination. Then, it generates a series of measurements to form a full and optimized protocol.

This algorithm was evaluated and tested for its ability to handle diverse geometries between the borehole and the surface / second borehole electrodes and to provide a specific format of full and optimized protocols. The resulting protocols were examined with synthetic and experimental models and with field measurements. Especially for the optimized protocols, their efficiency in approaching the full protocol's results with diminished measurements was further discussed. Furthermore, according to each geometry, an attempt was made to specify a trusted area for the inversion process.

The outline of the thesis is as follows:

- The theory and basic principles of the electrical resistivity tomography method were referred. This presentation included the ways of acquiring the apparent resistivity data, the geometry of the common electrode configurations and the inversion and optimization process.
- The presentation of the generated algorithm and the proceedings led to the development of a full and optimized protocol.
- The results of synthetic models and laboratory experiments that were used to examine the applicability of this algorithm.

- Lastly, the outcomes of applying this algorithm in real data, which were conducted on the walls of Rotunda church in Thessaloniki, and the feasibility of this approach was further determined.

2. INTRODUCTION

This chapter presents some basic concepts concerning the electrical resistivity method, including the basic theory, the resistivity arrays, the electrical resistivity tomography, the inversion process and the array optimization. This information is mainly focused on concepts that formed the basis for the creation of the algorithm and the processing of the results of this thesis.

The basic theory contains the equations that lead to the calculation of apparent resistivity and explains how the measurements are acquired. Some of the standard resistivity arrays for the surface are presented, and the proposed arrays for cross-hole measurements are also referred. Furthermore, the data acquisition using electrical resistivity tomography is explained. Moreover, the basic principles of the inversion process and some array optimization techniques will be referred.

2.1 Basic theory

The electrical method can provide information on the distribution of electrical resistivity of the ground since it consists of geological formations and materials with different electrical properties. Due to this discrimination, it is possible to measure their electrical resistivity and associate it with the expected formations of the area. The technique injects direct current (DC) via two electrodes and measures the potential difference using two other electrodes. For a cylindrical body (Figure 2.1), the resistivity ρ (Ohm-m) is given by the equation:

$$\rho = R \cdot \frac{S}{L} \tag{2.1}$$

where R (Ohm) is the resistance, S (m^2) is the cylinder's cross-sectional area, and L (m) is its length. The electrical resistivity depends on many factors concerning the soil of the investigation, such as its nature (mineralogy, particle size distribution), void presence, water saturation, electrical properties of enclosed fluids and temperature (Samouëlian et al., 2005).

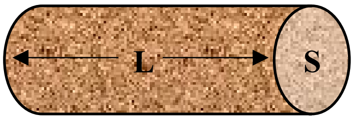

Figure 2.1: Cylindrical body of length L and cross-sectional area S.

The reciprocal of resistivity is called conductivity σ (Sm^{-1}) and describes the material's ability to conduct an electric current:

$$\sigma = \frac{1}{\rho} \tag{2.2}$$

Also, according to Ohm's law the electrical resistance of a body is given by the equation:

$$R = \frac{V}{I} \tag{2.3}$$

where V (V) is the potential and I (A) is the current.

Consider a homogenous and isotropic half-space and the current electrodes placed on the ground; the electrical equipotentials are hemispheric, so the resulting potential is equal to:

$$V = \frac{\rho I}{2\pi r} \tag{2.4}$$

Where ρ is the resistivity, I is the current, and r is the radius of the hemisphere. When the electrodes are buried into the ground, the denominator of equation 2.4 changes to «4πr» since the equipotentials turn spherical.

As mentioned above, the potential difference measurement occurs with the injection of DC electrical current. Four electrodes are needed for this measurement. Two (A and B) are the current electrodes, and the rest (M and N) are the potential electrodes. Let's consider the arrangement of Figure 2.2. According to equation 2.4 the potential in point M due to $A^{(+)}$ and $B^{(-)}$ is

$$V_M = \frac{\rho I}{2\pi}\left(\frac{1}{AM} - \frac{1}{BM}\right) \tag{2.5}$$

where AM and BM are the distances of M from A and B, accordingly. Likewise, for electrode N,

$$V_N = \frac{\rho I}{2\pi}\left(\frac{1}{AN} - \frac{1}{BN}\right) \tag{2.6}$$

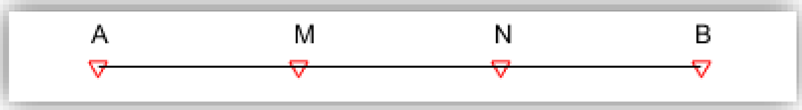

Figure 2.2: Arbitrary arrangement of 2 current electrodes ($A^{(+)}$ and $B^{(-)}$) and two potential electrodes (M and N).

So, taking into consideration the equations 2.5 and 2.6, the potential difference is equal to:

$$V_{MN} = \frac{\rho I}{2\pi}\left(\frac{1}{AM} - \frac{1}{BM} - \frac{1}{AN} + \frac{1}{BN}\right) \tag{2.7}$$

Solving for ρ, the equation 2.7 becomes:

$$\rho = \frac{V_{MN}}{I}\left(\frac{2\pi}{\frac{1}{AM} - \frac{1}{BM} - \frac{1}{AN} + \frac{1}{BN}}\right) = \frac{V_{MN}}{I} K \tag{2.8}$$

K is the geometric factor that depends on the distances between the electrodes.

Due to the fact that the underground is not homogenous but consists of different formations, the electrical resistivity of equation 2.8, is called apparent resistivity, «ρ_α». It represents an average of the resistivities of the formations in place and not their true resistivities. To obtain the true resistivities of the ground, the data should undergo the inversion process.

2.2 Resistivity arrays

Surface Measurements

As mentioned above, a prerequisite for taking measurements is the existence of at least four electrodes placed at known positions. Theoretically, these positions could be random, but moving the electrodes, in this case, would be more labour-intensive. For this reason and since it is more practical in the field, standard symmetrical arrays are preferred for the measurements. Such arrays are the Wenner, Schlumberger, Dipole-Dipole, Multiple-gradient, etc., mainly applied for surface measurements.

Wenner:

In this array, the current electrodes are placed on the outside and the potential electrodes on the inside, as shown in Figure 2.3. Their spacing is equal, AM=MN=BN=a and the apparent resistivity is calculated by equation 2.8, replacing the distances with «a»:

$$\rho_\alpha = \frac{V_{MN}}{I} K = \frac{V_{MN}}{I} 2\pi\alpha \qquad 2.9$$

Schlumberger:

The electrodes are placed as in the Wenner array, but their spacing differs. If the current electrodes are in the distance equal to $2L$, the potential electrodes are in the distance $2l$, and $L >> 10l$. The apparent resistivity is calculated by:

$$\rho_\alpha = \frac{\pi L^2}{2l}\frac{\Delta V}{I} \qquad 2.10$$

Dipole-dipole:

The current dipole (A-B) in this array is separated from the potential dipole (M-N). The dipoles have the same spacing, «a», and are separated in an integer multiple of their spacing distance, «na». The apparent resistivity results from the equation:

$$\rho_\alpha = -\pi n(n+1)(n+2)a\frac{\Delta V}{I} \qquad 2.11$$

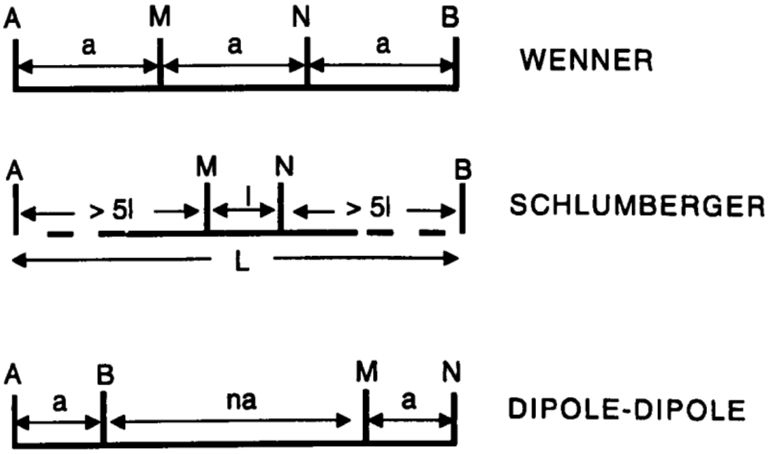

Figure 2.3: Schematic presentation of some of the most common electrode arrays. (Tsourlos, 1995)

Multiple-Gradient:

In the multiple-gradient configuration, the electrodes are placed in one line. Its length is divided into equal segments, «e», where the current electrodes are situated on the edges of each segment (Dahlin & Zhou, 2004; Martorana et al., 2017), and the in-between potential dipole can be placed in all the available internal positions. In Figure 2.4 an example is shown. For e=1, the current electrodes are placed only in the first and last position, and all the in-between positions are utilized from the potential electrodes. For e=2, the line is divided into two equal spaces; the current electrodes' available positions are now three and so on.

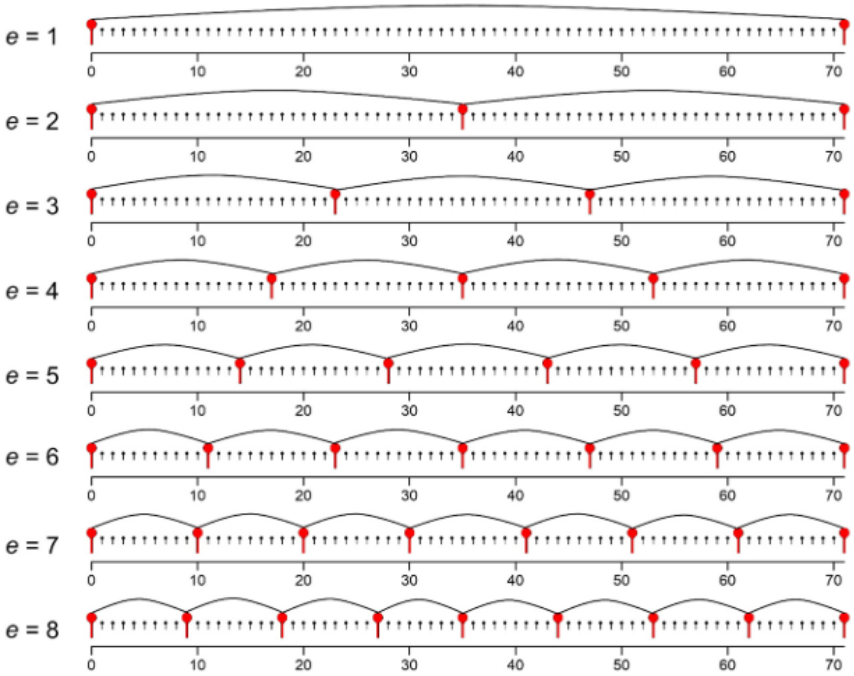

Figure 2.4: Illustration of a cross-hole Multiple-gradient configuration. (Martorana et al., 2017)

Cross-Hole Measurements

To realize cross-hole measurements, the boreholes should be at a close distance for better resolution in the area between them. The Wenner and Schlumberger are not optimum (Tsourlos et al., 2011), so other arrays have been preferred, such as the Dipole-Dipole and Pole-Tripole (Goes & Meekes, 2004), or the Bipole-Bipole (Bing & Greenhalgh, 2000). Some of them were also modified and applied in different investigations i.e. to long-term monitor CO_2 (Schmidt-Hattenberger et al., 2016), to detect ancient walls (Leontarakis & Apostolopoulos, 2013), or to investigate the subsurface for construction purposes (Almpanis, 2018).

Dipole-Dipole:

In the case of a cross-hole arrangement, the possible configurations are AM-BN, AM-NB, and AB-MN, where the first two electrodes are in one borehole and the other two in the second (Figure 2.5). According to Goes & Meekes (2004), the first two configurations have the advantage that the potential electrodes are in different boreholes and close to the current electrodes so that the potential difference will be significant and less sensitive to the background noise. Also, the current has to flow between the investigated area of the two boreholes.

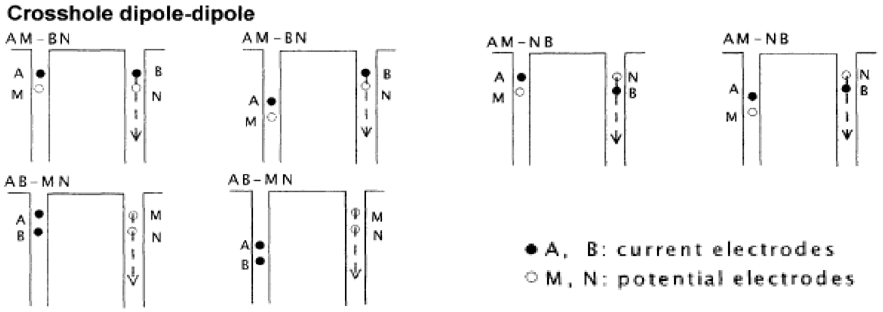

Figure 2.5: Illustration of a cross-hole Dipole-Dipole configuration. (Goes & Meekes, 2004)

Bipole-Bipole:

There are three independent configurations for the cross-hole measurements with the bipole-bipole array: AM-BN, AM-NB and AB-MN (Bing & Greenhalgh, 2000) (Figure 2.6). According to their research, the first two have similar results for the cross-hole measurements. The last one has significant differences since it is contaminated with noise, and the potential difference signal is very low.

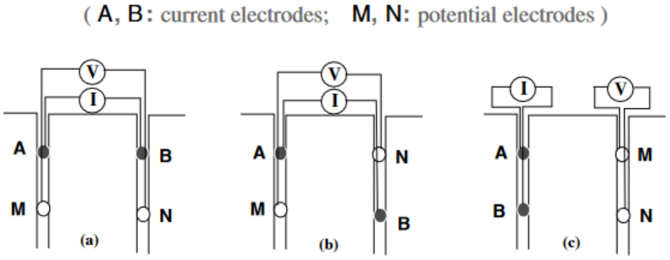

Figure 2.6: Illustration of a cross-hole Bipole-Bipole configuration. (Bing & Greenhalgh, 2000)

Pole-Tripole:

In the pole-tripole array, three electrodes are situated in one borehole, and the fourth is in the second (Figure 2.7). In this configuration, the direct line between the current electrodes is always such that it creates a wide angle with the horizontal layers, so the current would flow through all of them and would locate thin horizons (Goes & Meekes, 2004),.

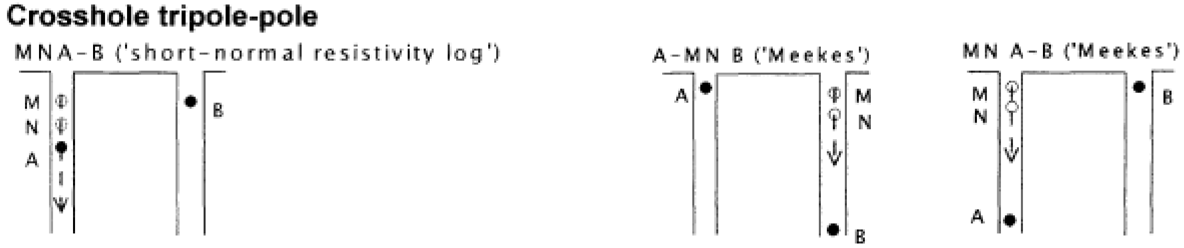

Figure 2.7: Illustration of a cross-hole Pole-Tripole configuration. (Goes & Meekes, 2004)

In many cases, though, the boreholes that may be drilled in a region are not at the appropriate distance for cross-hole measurements, so the area between them cannot be investigated adequately. For this reason, the need to combine borehole and surface electrodes has been proposed. In some cases, in-line measurements are acquired where the sequence starts from one borehole, continues up to the surface electrodes and maybe even end to the second borehole (Leontarakis & Apostolopoulos, 2013), or the surface electrodes are independent and act like a second borehole (Σιμυρδάνης, 2013). In both cases, the configurations used are modifications of the aforementioned basic cross-hole arrays.

2.3 Electrical resistivity tomography

Electrical resistivity tomography (ERT) is a widely used measurement procedure. Thanks to the advances in the development of instruments and processing techniques (Griffiths & Barker, 1993), obtaining crucial information regarding the subsurface is possible. The ERT-measured apparent resistivities are presented as pseudosection, where the measured apparent resistivity values are plotted between the centre of the quadrupoles. The ERT technique has been applied in many studies, such as in cases where there was the need to detect underground utilities or cavities, investigate old and ancient structures, determine fault zones and evaluate potential construction sites, assess hydrologic features and detect the bedrock or other targets (Ducut et al., 2022).

The number of electrodes that will be equipped can vary, depending on the instrument's availability and ability to place them. The electrodes are placed in a line, and the device takes measurements automatically using the desired array. Figure 2.8 (Fehdi et al., 2014) shows an example of an electrical resistivity tomography using the Wenner configuration. The current electrodes (A and B) and the potential electrodes (M and N) are in the position «Measure 1» for the first measurement, and the potential difference is measured at the centre of the arrangement, as indicated by the blackened bullet 1. Then automatically, the current and potential electrodes are moved one position to the right, where the measurement of the second bullet occurs. This routine continues up until the last four electrodes. Then, the spacing between the electrodes increases and becomes «2a» and «Measurement 17» occurs. Only this time, the depth increases; the measured point is shown with the blackened bullet 17. Again, the electrodes move to the following positions until the measurements are completed. This procedure is repeated until the acquisition of all the desired measurements.

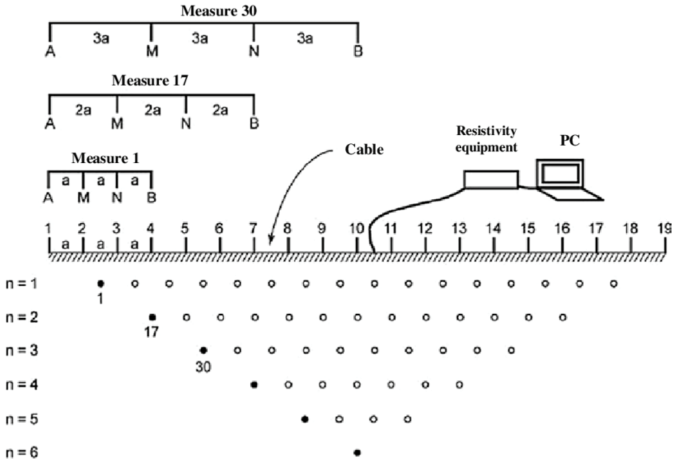

Figure 2.8: Example of the acquisition of measurements with the method of electrical resistivity tomography. (Fehdi et al., 2014)

One instrument manufactured to obtain these measurements is the multi-channel sounding and profiling system, Syscal pro, manufactured by IRIS instruments (http://www.iris-instruments.com/syscal-pro.html). It is capable of measuring resistivity with a maximum current injection 2500mA. A significant characteristic that improves the measurements' acquisition speed, is its ability to measure up to 10 channels automatically and simultaneously. The experimental and field data were collected using this instrument (Figure 2.9).

Figure 2.9: The Syscal pro instrument, that was used for the acquisition of the measurements.

2.4 Inversion

As mentioned above, the measured values are apparent resistivity, not true subsurface resistivity. The primary process in geophysical practice is to find the distribution of the true subsurface resistivity based on the measured apparent resistivities. The most common approach to achieve this is the inversion process. The inversion aims to find a subsurface resistivity model that would generate synthetic apparent resistivities as close as possible to the measured apparent resistivities. For this to be feasible, the forward problem should be solved first. The forward problem correlates the distribution of the subsurface resistivities with the measurements. More specifically, if x represents the resistivities distribution and y the measurements, then the solution of the forward model is the variable, T, so that:

$$y = T(x) \tag{2.12}$$

The solution of the inverse problem is the reverse formation T^{-1} that connects the known measurements y (measured on the field) with the unknown resistivity distribution, x, meaning:

$$x = T^{-1}(y) \tag{2.13}$$

There are two ways of handling the solution of the forward problem: the analytical and the numerical approach. The former is mainly used for simple structures (i.e., buried sphere) because they have known solutions. The latter can model even complex resistivity distributions as it involves advanced numerical procedures performed by computers. Usually, the numerical approach is implemented since the structure can be more complicated. (Tsourlos, 1995)

As for the inverse problem, its purpose is to identify the real resistivities of the subsurface, from the measured apparent resistivities. Different deterministic techniques to solve the inverse problem include the non-linear least-square, weighted least-square, Marquadt's method, smoothness constrained inversion (Occam), and inversion with apriori information (Tsourlos, 1995). Since the explanation of each of them is beyond the scope of this thesis, only one of them, the least-square method, will be referred to. The general equation that describes the resistivity problem is:

$$f(x) = y \tag{2.14}$$

where y is the observed data vector, x is the unknown parameter vector (resistivity distribution), and f(x) is the forward solver. Expanding this non-linear equation into a Taylor series and ignoring the higher-order terms, it turns out that:

$$f(x + dx) = f(x) + Jdx \tag{2.15}$$

dx is the resistivity correction vector, and J is the Jacobian matrix. The purpose is to find the minimum error between the observed and the predicted data. At the least-square method, the iterative process seeks to find the optimum dx vector for which the sum of errors becomes minimum. After some calculations, the resulting dx vector is equal to:

$$dx = (J^T J)^{-1} J^T dy \tag{2.16}$$

So, it is evident that calculating the Jacobian matrix (J) is significant in solving the inverse problem. Consider as *n,* the number of elements in the parameter vector, **x**, and *m* the number of elements in the observed data vector, ***d***. The Jacobian **J** is a mxn matrix and its ith,jth element is expressed as:

$$J_{ij} = \frac{\partial d_i}{\partial \rho_j} \tag{2.17}$$

where ρ_j is the resistivity of parameter x_j. The Jacobian matrix is also called the sensitivity matrix, since it provides information about the sensitivity of the measured values, viz. it shows how much the apparent resistivity changes if a minor variation in resistivity occurs. If the observed data are apparent resistivities, then the equation 2.17 turns to:

$$J_{ij} = \frac{\partial \rho\alpha_i}{\partial \rho_j} = -\frac{\partial \rho\alpha_i}{\partial \sigma_j} = \frac{2\pi}{GI}\frac{\partial \Delta V_i}{\partial \sigma_j} \tag{2.18}$$

where G is the geometric factor, and I is the intensity of the inserted current. These values are known, and the only one remaining to calculate the Jacobian matrix is the variable ($\partial \Delta V_i / \partial \sigma_j$). This can be calculated using the sensitivity, the adjoint equation and the perturbation technique (Tsourlos, 1995). For this thesis, it was calculated using the equation for homogenous half-space by (Loke & Barker, 1995). For a rectangular block of finite dimensions (Figure 2.10), the partial derivative ($\partial \Delta V / \partial \rho$) is:

$$\frac{\partial V}{\partial \rho} = \frac{I}{4\pi^2} \int_{Z1}^{Z2} \int_{X1}^{X2} \int_{-\infty}^{+\infty} \frac{x(x-a) + y^2 + z^2}{(x^2 + y^2 + z^2)^{1.5} \cdot [(x-a)^2 + y^2 + z^2]^{1.5}} dy\, dx\, dz \tag{2.19}$$

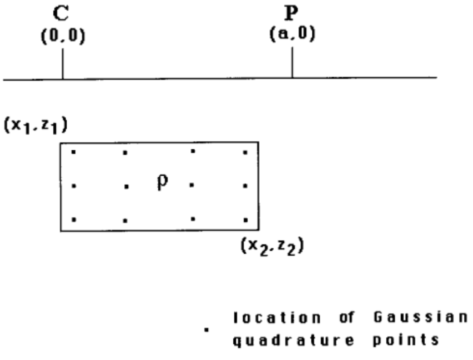

Figure 2.10: Parameters of a rectangular block that affects the calculation of the 2D partial derivative of the block. C is the current electrode and P the potential. (Loke & Barker, 1995)

The iterative inversion process, described in equation 2.16, stops when some conditions are met. One typical condition is the % relative root mean square (RMS) error: the error between the observed and the calculated data. RMS is calculated by the following equation:

$$\% \, RMS \, error = 100 \cdot \sqrt{\frac{1}{m}\sum_{i=1}^{m}\left(\frac{(d_{Oi}-d_{Ci})^2}{{d_{Oi}}^2}\right)} \tag{2.20}$$

Where m is the number of measurements, d_{Oi} is the observed data, and d_{Ci} is the calculated data. The iterative process ends when there is no improvement in this error, meaning that the computed data can no longer approach the observed, and the error remains approximately the same. This process can also be stopped if the error between the real and observed data increases, or if the predefined number of iterations has been reached, or if the misfit error is less than the observation error (Tsourlos, 1995).

The inversion of ERT data in this thesis were realized with the DC_2DPro software (Kim, 2017). The program performs an iterative smoothness-constrained inversion. Users can interfere with the data and adjust the inversion parameters (Figure 2.11). The software allows the alteration of the inversion block size and provides the choice to add apriori information for the synthetic models. After the inversion process, the RMS error appears, and if it's not optimal, the user can delete data points by misfits and rerun the inversion for better results.

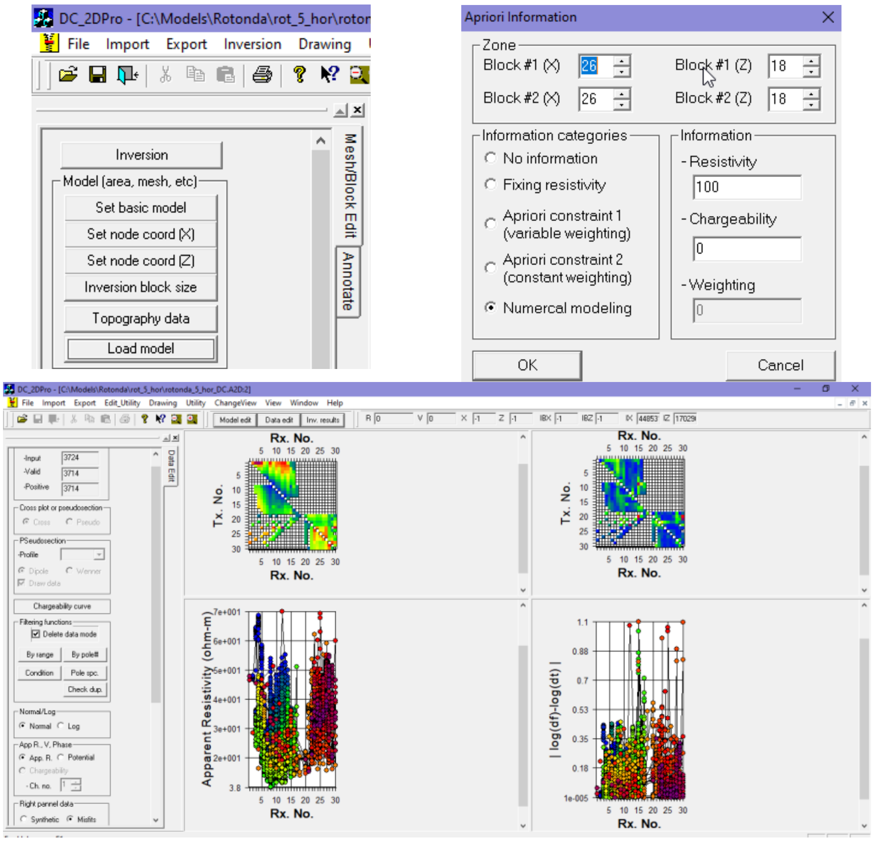

Apriori Information

Zone

Block #1 (X) 26 Block #1 (Z) 18

Block #2 (X) 26 Block #2 (Z) 18

Information categories

○ No information

○ Fixing resistivity

○ Apriori constraint 1 (variable weighting)

○ Apriori constraint 2 (constant weighting)

● Numercal modeling

Information

- Resistivity 100
- Chargeability 0
- Weighting 0

Figure 2.11: Windows that show some of the parameters that the user can alter in the DC_2DPro software.

2.5 Optimization

Recently, due to technological advances, geoelectrical measuring instruments can acquire a significant number of measurements automatically and quite rapidly. But sometimes, the survey conditions may require only a limited number of measurements to be collected, or the measurement needs to be obtained in the fastest possible way (i.e., monitoring experiments). In such cases, a measurement optimization process can be beneficial. The target is to select some of the measurements of the full measurement protocol that would provide similar results with fewer measurements and reduced acquisition time. For this reason, many methods have been proposed, and some of them will be presented in the following sections (Stummer et.al., 2004; Wilkinson et.al., 2006; Αθανασίου, 2009).

2.5.1 Stummer et al. (2004) methodology

Before referring to this methodology, the concept of the model resolution matrix, R, should be presented. This matrix is defined as:

$$m^{est} = Rm^{true} \tag{2.21}$$

where m^{est} are the estimated model parameters, and m^{true} are the actual model parameters that are unknown. Resolution matrix, is a m x m matrix that shows how well a particular estimated model parameter fits to the true one. If R=I, where I is the identity matrix, the model parameters are uniquely determined (perfect fit), and if not, they are weighted averages of the actual parameters. The matrix R is calculated by:

$$R = J^{-1}J \tag{2.22}$$

where J^{-1} is the generalized inverse matrix. (Menke, 2018)

The optimization is based on the model resolution matrix, considering the initial model a homogenous half-space. According to Noel & Xu (1991), for n electrodes equally spaced, there are:

$$nd = n \cdot (n-1) \cdot (n-2) \cdot (n-3)\ /\ 8 \tag{2.23}$$

possible, non-reciprocal four-electrode combinations. Rejecting some of them (n^{excl}) due to high geometric factors (i.e. low signal) or other reasons, the final measurements that Stummer et al. (2004) used was

$$nd' = (n \cdot (n-1) \cdot (n-2) \cdot (n-3)\ /\ 8) - n^{excl} \tag{2.24}$$

This set is named comprehensive data. Let's assume a nm inversion cell and the Jacobian of the comprehensive data, meaning all possible combinations, as J^{compr}. From the nd′ configurations, n^{base}

configurations are selected such that the Jacobian, J^{compr}, is subdivided into a $(n^{base} \cdot nm)$ matrix J^{base} and a $[(n^{base} - nd') \cdot nm]$ matrix J^{add}. At the beginning of the optimization, the n^{base} configurations are the ones that correspond to the array that was used for the initial data acquisition. The configurations that are contained in J^{add} matrix are ranked according to the goodness function:

$$GF(i) = \sum_{j=1}^{nm} \frac{\left|J_{ij}^{add}\right|}{J_j^{sum}} \left(1 - \frac{R_{jj}^{base}}{R_{jj}^{compr}}\right) \quad i = 1, \dots, (nd' - n^{base}) \tag{2.25}$$

where,

$$J_j^{sum} = \frac{1}{nd} \sum_{i=1}^{nd'} \left|J_{ij}^{compr}\right| \tag{2.26}$$

J_j^{sum} is a normalization factor that balances the high sensitivity of the near-surface cells with the ones deeper, which are imposed to less good sensitivity. R^{base} and R^{compr} are calculated using equation 2.22 for the equivalent Jacobian matrices.

Except for the goodness function, the candidate configurations are also checked for their linear independence from the base data set using the following equation:

$$LI(i) = \left| \frac{\sum_{j=1}^{nm} J_{ij}^{base} J_{kj}^{add}}{\left|J_i^{base}\right| \left|J_k^{add}\right|} \right| \quad i = 1, \dots, n^{base} \tag{2.27}$$

The LI values below a threshold will be added to $J^{base,}$ and the procedure repeats for each candidate configuration. After this process, the R^{base} is calculated again with the added values.

2.5.2 Wilkinson et al. (2006) methodology

Wilkinson et al. (2006) proposed a different version based on the Stummer's et al. (2004) methodology. The optimization starts with a data set (base) of configurations. From the comprehensive data set that contains all the possible configurations, each one of them that is not included in the base data set is ranked by a goodness function:

$$F(i) = \sum_{j=1}^{m} \frac{J_{ij}^2}{\left(J_j^{sum}\right)^2} \left(1 - \frac{R_{jj}^{base}}{R_{jj}^{compr}}\right) \tag{2.28}$$

where m is the number of model cells, and

$$J_j^{sum} = \frac{1}{nb} \sum_{k=1}^{nb} \left|J_{kj}\right| \tag{2.29}$$

Index k indicates all the nb configurations included in the base set. The difference between the proposed method by Stummer et al. (2004) is that equation 2.29 summarises only the base configurations and not the entire comprehensive data set, which provides a higher weighting to the configurations that are linearly independent of the data set. Also, with the implementation of both equation 2.28, which chooses configurations that enhance the poorly resolved regions of the model, and equation 2.29, the selected configurations are checked simultaneously for their linear independence from the base set. So, this excludes the time-consuming stage of calculating the equation 2.27.

2.5.3 Athanasiou (2009)

A different method was proposed by Αθανασίου (2009), where the optimized measurements were extracted from the full protocol using only the Jacobian matrix, J, and not the resolution matrix, R. This way, the process would be much quicker since the inversion would not have to occur.

More specifically, all the possible measurements are calculated. Then, some of them can be eliminated if their geometric factor is higher than a value, indicating a measurement with a low signal. From the remaining measurements, the Jacobian matrix is calculated. For instance, let's consider the example of Figure 2.12, which consists of four parameters and five apparent resistivity measurements. So, the Jacobian is a matrix of (five rows) x (four columns) that correspond to each measurement and parameter, respectively.

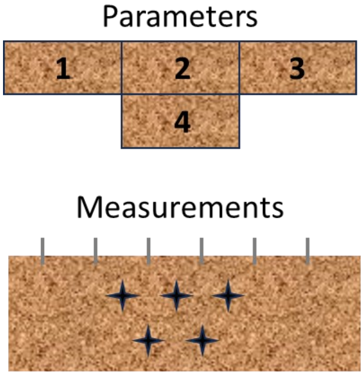

Jacobian Matrix

		Parameters			
		P1	**P2**	**P3**	**P4**
Measurements	**M1**	0.798	0.226	-0.025	0.128
	M2	0.625	-0.276	0.220	-0.028
	M3	-0.356	0.856	-0.986	~~0.935~~
	M4	0.832	-0.347	0.856	~~0.658~~
	M5	0.556	0.885	0.659	~~-0.663~~

Figure 2.12: Example of the optimization process for four parameters and five measurements proposed by Athanasiou. (Modified from Athanasiou, 2009)

The proposed method is that each time, the chosen measurement for each parameter is the one that results in the value with the highest absolute sensitivity and has not been selected by any other iteration. So, in Figure 2.12, for the P1 parameter, the highest value is the one noted with blue colour, which corresponds to the measurement M4. The chosen measurements for the P2 and P3 parameters are the M5 and M3, respectively. But for the parameter P4, the highest absolute value is this of M3, which was previously chosen for P3. So, the iterative process will seek the second higher value, that is, this of M5. Once again, this measurement has been chosen, so the process continues until it finds a measurement that another parameter has not used again. In this case, the measurement that finally corresponds to the P4 parameter is M1.

An additional process was added (Αθανασίου, 2009) to calculate explicitly the less sensitive parameters based on the Jacobian matrix. First, the sum of the absolute values of each parameter, called L1-norm, is calculated. The parameters are then sorted according to their L1 norm value and grouped into clusters, the number of which is selected by the user. The number of measurements for every parameter is predefined for each cluster and is proportional to the ranking. The number of measurements chosen for parameters with low L1-norm (poorly resolved) is much higher than those with high L1-norm values (well resolved).

3. A FLEXIBLE PROTOCOL GENERATION ALGORITHM

The algorithm generated to achieve this thesis' scope will be presented and explained in this chapter. The algorithm was developed in Matrix Laboratory (MATLAB) and is partly based on an existing algorithm provided by P. Tsourlos. To be more user-friendly and accessible, a graphic user interface designed by a Matlab App designer was also included.

The code's primary purpose was to create a full and propose some optimized protocols for diverse geometries of borehole-surface electrodes. This capability was further updated to include the possibility of generating protocols for geometries between two dipping boreholes. The algorithm's presentation is divided into two parts: the theoretical analysis of the algorithm and the practical. The former describes all the theory that formed the base for the generated algorithm, and the latter includes a short description of the graphic user's interface windows. More specifically, the steps followed to produce full and optimized datasets are presented on the flow chart of Figure 3.1.

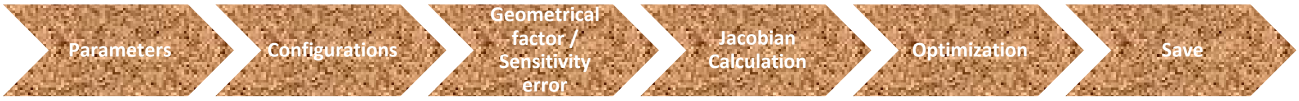

Figure 3.1: Flow chart that presents the steps that were followed for the production of the full and optimized datasets.

3.1 Theoretical analysis

The algorithm initiates with the insertion of some parameters, such as the number of electrodes that will be utilized, the coordinates of the first electrode, the electrode spacing, and the degrees of inclination so that the desired geometry can be formed. With this information, it is possible to calculate the coordinates of the electrodes. The electrodes that will be inserted into the borehole and the ones at the surface/second borehole are independent, meaning that the electrode coordinates are joined in a matrix while being calculated separately. In this way, the mentioned values could be unequal, and the possibility of different inclinations between two boreholes could be feasible.

Consider an arbitrary coordinate system of «x» and «z» axes. The coordinates of the first borehole electrode correspond to the shallower placed electrode, and the calculation of the rest borehole's electrode coordinates occurs according to this point, the spacing and the degrees of inclination. The same is applied in the case of a second borehole. As for the surface electrodes, the first electrode has the smaller «x» value (i.e., x=0) and the rest are calculated according to the spacing.

While calculating the electrode coordinates matrix, a unique ID number is appointed to each electrode and will be used in the next step. In the case of a borehole-surface array, by default, the numeration starts from the deepest borehole electrode and continues until the farthest surface electrode.

Similarly, in a borehole-borehole array the numeration initiates from the deepest left borehole's electrode to the deepest second borehole's electrode. The spacing in every borehole could vary, and the degrees of inclination can be between 0 and less than 180 degrees.

The second step involves the generation of the full protocol. The measurements are collected with the available arrays. Since there are no standard arrays for borehole-surface measurements, the cross-hole arrays are applied, considering the surface to be a second borehole. The arrays included are the pole-tripole, bipole-bipole equatorial, bipole-bipole diagonal, dipole-dipole and in-line multi-gradient in the borehole and the surface / second borehole, separately. A schematic illustration for a borehole-surface measurement was created for each configuration, with 12 electrodes each and the same spacing, «a», to both borehole and surface. Two current electrodes (A and B) and two potential electrodes (M and N) illustrate the arrangements and how the measurements are acquired. The symbol «-» will indicate the division of the electrodes in the first borehole and the surface / second borehole.

For the pole-tripole array, the configuration (B-NMA and NMA-B), that was proposed by Goes & Meekes (2004) and referred to in a previous chapter (2.2) was applied. Also, the configuration B- AMN and AMN-B were used, where the current poles are situated in the borehole and at the surface (Figure 3.2). The parameters that the user can alter are the current step for every iteration and the maximum potential dipole separation from the source electrodes (1a, 2a, ..., etc.).

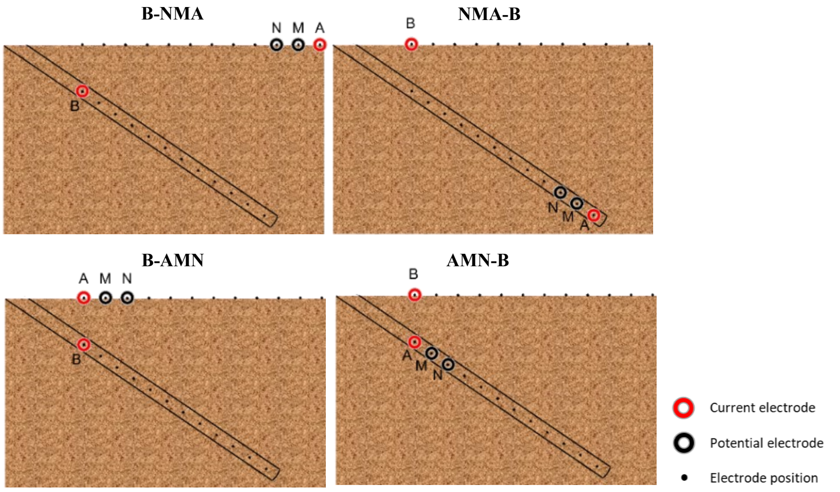

Figure 3.2: Illustration of a borehole-surface measurement with the pole-tripole array and the different configurations.

Other arrays that the user can choose are the bipole-bipole equatorial and diagonal. The configuration used is the BN-AM (Figure 3.3). The current electrodes are placed again on cross-symmetric positions, and the potential dipole recedes at farthest distances. Different maximum separations of the two pairs can be selected. After collecting these measurements, the current electrodes move to the next step, and the potential electrodes move away. The discrepancy between the equatorial and diagonal configurations is that in the latter, one of the potential electrodes, instead of moving simultaneously with the other, remains fixed in its position and only the second one moves to further distances (again, the opening of the electrodes can vary) and vice versa.

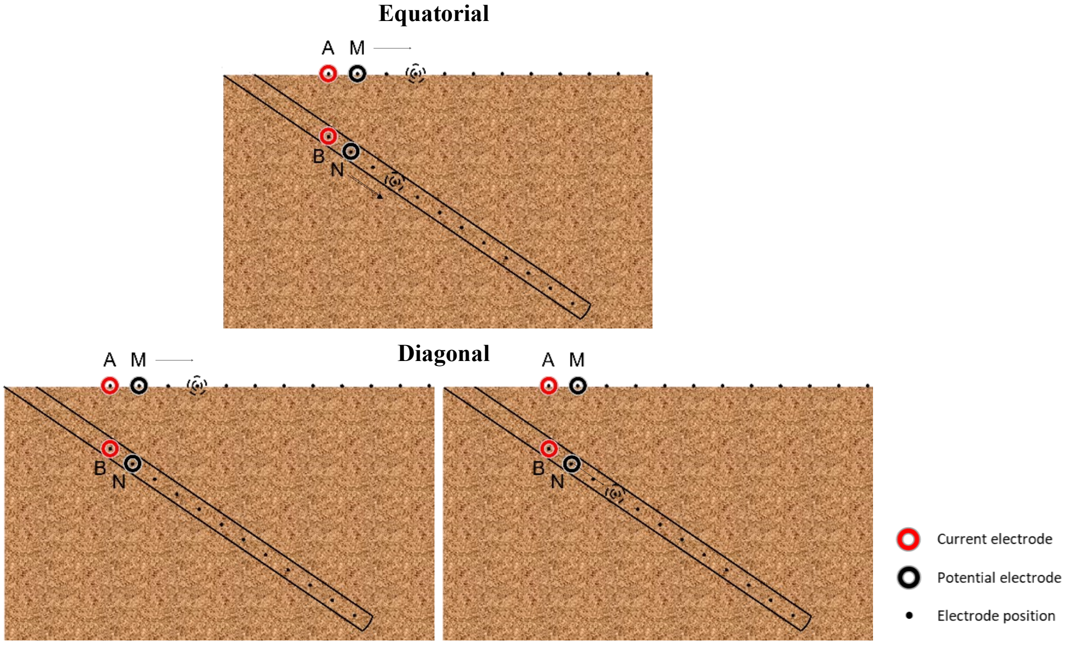

Figure 3.3: Illustration of a borehole-surface measurement with the equatorial (top) and diagonal (bottom) bipole-bipole array.

The dipole-dipole array is available only for borehole-surface measurements since the configuration used was the MN-AB (Figure 3.4), with the current electrodes always on the surface. The user can define the maximum separation of the current and potential electrodes from each other. The current and the potential electrodes from the first position, where they are at a distance equal to one spacing, «a», move one step at a time until their last position. A second sequence will start but with the current electrodes at a distance equal to two spacings, «2a», three spacings, «3a», etc. The same will happen if the maximum potential separation would advance.

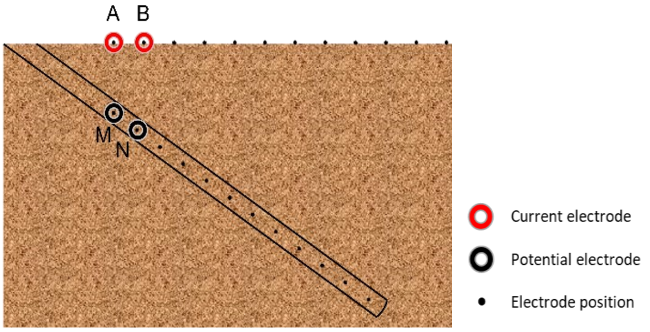

Figure 3.4: Illustration of a borehole-surface measurement with the dipole-dipole array.

Lastly, the final arrays are the in-line multiple gradient at the surface and in the borehole separately as indicated in Figure 3.5. This routine continues with electrode A, which is stable in its position, and then another sequence begins with the movement of this electrode. The process ends when the desired measurements have been taken.

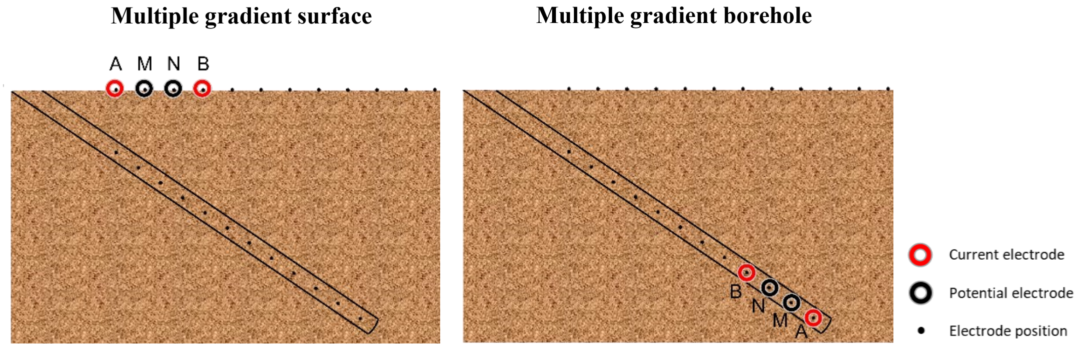

Figure 3.5: Illustration of a borehole-surface measurement with the multiple-gradient array. The measurements are collected separately in the borehole and surface, as it is indicated in the figure.

The measurements generated by the chosen configurations are then evaluated for their geometric factor and sensitivity error. The geometric factor of each one of the quadrupole measurements is calculated, and all those over a given threshold are rejected. The user can choose between the option to input an arbitrary threshold value or calculate a threshold from the instruments and soil's properties using the equation:

$$\text{Resulting threshold} = \frac{Source\ Voltage \cdot Minimum\ expected\ resistivity}{Voltage\ accuracy\ \cdot Contact\ resistance} \qquad 3.1$$

where the source voltage and voltage accuracy are related to the employed instrument, and the minimum expected resistivity and contact resistance are dependent on the region's geological formations. After choosing the threshold, the rejection of the measurements occurs.

A second filtering was also applied to the candidate measurements (Wilkinson et al., 2008). The concept of this filtering is to discard configurations that are very sensitive to positioning errors. This is an indication of a potentially "unstable" measurement that could contaminate the results of the inversion with noise.

The sensitivity error was calculated according to Wilkinson et al. (2008). Based on their research, when placing the electrodes, some errors occur in the geometry (i.e., uncertain positions, imprecise spacings, inaccurate depth) and thus in the geometric factor. The following equation gives the generalized geometric factor:

$$K = \left(\frac{4\pi}{\frac{1}{AM} - \frac{1}{BM} - \frac{1}{AN} + \frac{1}{BN} + \frac{1}{A'M} - \frac{1}{B'M} - \frac{1}{A'N} + \frac{1}{B'N}} \right) = \frac{4\pi}{H} \qquad 3.2$$

where, A and B are the current electrodes, M and N are the potential electrodes, AM is the distance of electrode A from M and A′M is the distance of M from the symmetrical point of A, considering the surface as the line of symmetry. The same is applied for the rest of the distances. The sensitivity, s, (Loke et al., 2014) of the geometric factor to errors is given by:

$$s = \left(\frac{\partial K}{\partial A}\right)^2 + \left(\frac{\partial K}{\partial B}\right)^2 + \left(\frac{\partial K}{\partial M}\right)^2 + \left(\frac{\partial K}{\partial N}\right)^2 \qquad 3.3$$

For the electrode A, which is placed in the position (x_a, y_a, z_a) the sensitivity error is:

$$\left(\frac{\partial K}{\partial A}\right)^2 = \left(\frac{\partial K}{\partial x_a}\right)^2 + \left(\frac{\partial K}{\partial y_a}\right)^2 + \left(\frac{\partial K}{\partial z_a}\right)^2 \qquad 3.4$$

An error in x_a will only affect the AM and AN distances so:

$$\frac{\partial K}{\partial x_a} = -\frac{4\pi}{H^2}\left(\frac{\partial H}{\partial AM}\frac{\partial AM}{\partial x_a} + \frac{\partial H}{\partial AN}\frac{\partial AN}{\partial x_a} + \frac{\partial H}{\partial A'M}\frac{\partial A'M}{\partial x_a} + \frac{\partial H}{\partial A'N}\frac{\partial A'N}{\partial x_a}\right) \qquad 3.5$$

where,

$$\frac{\partial H}{\partial AM} = -\frac{1}{AM^2} \qquad 3.6$$

$$AM^2 = (x_A - x_M)^2 + (y_A - y_M)^2 + (z_A - z_M)^2 \qquad 3.7$$

$$\frac{\partial AM}{\partial x_a} = -2(x_A - x_M) \qquad 3.8$$

Similar equations will hold for the rest of the distances and points (y_a, z_a). These equations apply to 3D investigations, but since this thesis concerns 2D surveys, the “y” dimension is ignored, and only x and z contribute to the sensitivity calculations. The geometrics’ factor relative error is then defined as:

$$Re = \frac{s}{K} \qquad 3.9$$

According to Wilkinson et al. (2008), the removed measurements had estimated relative error Re $\geq$ $5\mathrm{m}^{-1}$. Since the uncertainties in the array depth were ~1cm, this limit equates to geometric factors of ~5 per cent. For the created algorithm, the sensitivity error corresponds to the error that would occur if all the electrodes had 3% displacement on their expected position. The borehole electrodes may be displaced in the horizontal and vertical distance, which is considered by assuming the error above in both directions. Instead of eliminating measurements as Wilkinson et al. (2008) proposed, a threshold value was chosen (Λούβαρης, 2020). The threshold for the accepted relative error values is selected according to each geometry.

The next step is the calculation of the Jacobian matrix. A regular grid of «x» and «z» points is formed based on the electrode coordinates. This grid corresponds to the parameters for which the Jacobian matrix will be calculated. The Jacobian matrix is calculated for every accepted measurement and every parameter. Also, the cumulative Jacobian (L1-norm, Αθανασίου (2009)) for each parameter is calculated.

Some points (parameters) can be eliminated to define a more specific area of interest near and around the electrodes. Effectively, the process attempts to limit the region of interest only to parameters which exhibit a cumulative sensitivity above a given threshold. For this reduction of points, the median of the cumulative Jacobian was used. All the values less than the median of the cumulative Jacobian or the median multiplied by a given value are disqualified, and only the rest of the values remain. After this elimination and when plotting the remaining points, the areas of low expected sensitivity are rejected from the optimization procedure.

In the following, the optimization based on the method proposed by Αθανασίου (2009) was used but with some modifications. The first change is that, as mentioned above, after calculating the Jacobian matrix and the L1-norm, there was the possibility of eliminating some parameters of the Jacobian matrix that were considered less sensitive. Secondly, the optimization occurs so that the resulting number of optimized measurements can be controlled. This was achieved by automatically calculating the clusters, depending on the desired number of the final measurements, which were chosen between three possible percentages concerning the number of measurements of the full protocol. The available percentages are of 25%, 50% and 75% of the full protocol, meaning that if the total measurements of the full protocol are for example, 10000, the optimized protocol of 25% will choose the most appropriate number of clusters so that after the optimization the final measurements are approximately 2500, etc.

More specifically, an iterative process was created to find the most appropriate number of clusters that would eventually lead to an optimized protocol with the chosen percentage of full measurements. For this iterative process, many clusters were tested, and the one that would result in measurements closer to the desired percentage was finally chosen. The following equation calculated the cluster length:

$$cluster\_length = floor\left(\frac{P_{max}}{i}\right) \qquad i = 1,2,3,\ldots,50 \tag{3.10}$$

where, Pmax is the total number of the parameters of the “new” Jacobian and «i» is the cluster examined each time. Then, for each iteration, meaning for each of the 50 different clusters, a temporary variable was created which stored the total number of the measurements that would be enlisted to each cluster if the chosen cluster was the examined one. Finally, the cluster with the smallest deviation from the desired number of final measurements is selected.

After completing all these processes, the full and optimized protocols are saved into output files as protocols, which can then be uploaded to the instruments (*.txt for Syscal and *.org for ABEM-Terrameter) or can be used to generate synthetic data (*.A2D for the DC_2DPro program) to test the performance of the protocols.

3.2 Application of the algorithm

3.2.1 Parameters

Initially, the user can choose between borehole-surface or borehole-borehole array and then input the appropriate information to form the desired geometry. For this purpose, there are two panels, one for the borehole electrodes and one for the surface (Figure 3.6) or the borehole 2 (Figure 3.7) electrodes. After inserting the parameters and clicking the ‘Preview’ button, the electrode coordinates are calculated and plotted along with their ID number on the graph. Examples of measurements are shown in Figure 3.6 and Figure 3.7 for a borehole-surface and borehole-borehole configuration, respectively. Note that surface electrode IDs have been reversed because the borehole’s tip is closer to the last surface electrodes. The ID number is essential when making the cable connections in the field.

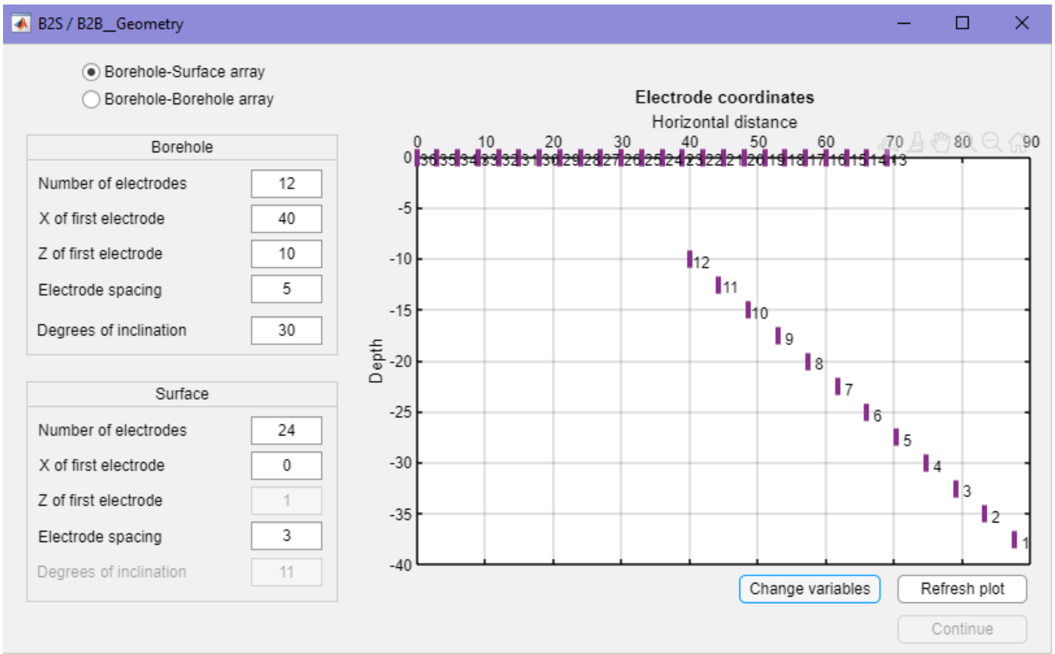
B2S / B2B__Geometry

● Borehole-Surface array
○ Borehole-Borehole array

Borehole
Number of electrodes: 12
X of first electrode: 40
Z of first electrode: 10
Electrode spacing: 5
Degrees of inclination: 30

Surface
Number of electrodes: 24
X of first electrode: 0
Z of first electrode: 1
Electrode spacing: 3
Degrees of inclination: 11

Figure 3.6: Geometry window. The user can add the appropriate information so that the desired geometry could be calculated and implemented.

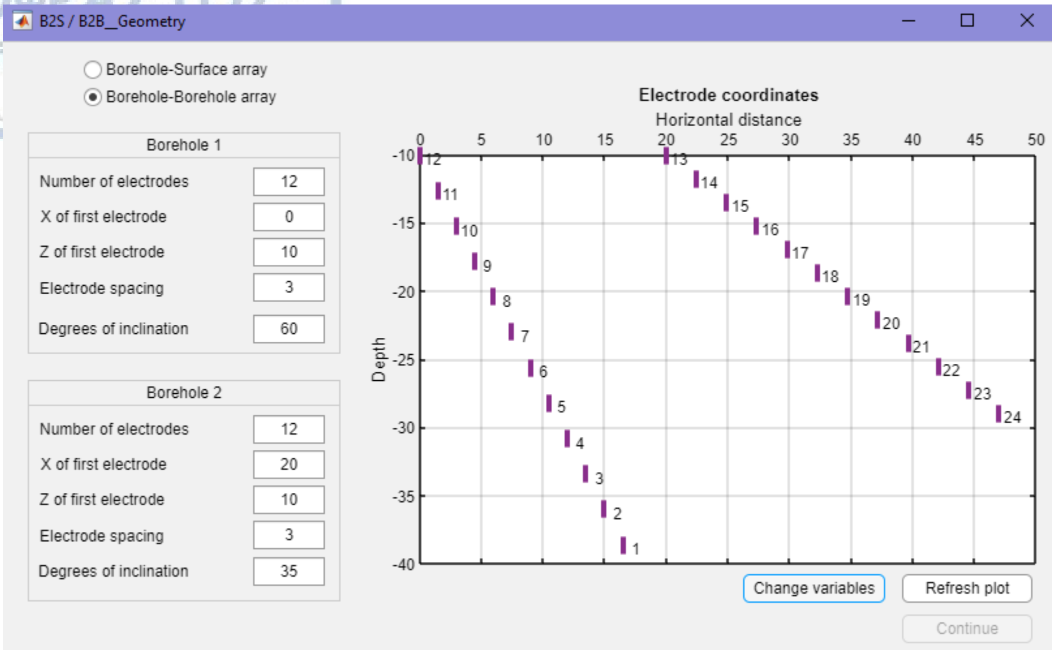

B2S / B2B_Geometry

○ Borehole-Surface array
● Borehole-Borehole array

Borehole 1

Number of electrodes	12
X of first electrode	0
Z of first electrode	10
Electrode spacing	3
Degrees of inclination	60

Borehole 2

Number of electrodes	12
X of first electrode	20
Z of first electrode	10
Electrode spacing	3
Degrees of inclination	35

Figure 3.7: Example of the geometry window when the borehole – borehole array is selected.

3.2.2 Configurations

The process continues with the user choosing one or more of the given arrays (Figure 3.8). The available arrays are the 1) pole-tripole, 2) bipole-bipole equatorial, 3) bipole-bipole diagonal, 4) dipole-dipole, 5) multi-gradient in the borehole and finally 6) multi-gradient in the surface. The dipole-dipole is only available in borehole-surface measurements. A matrix with all the quaternary

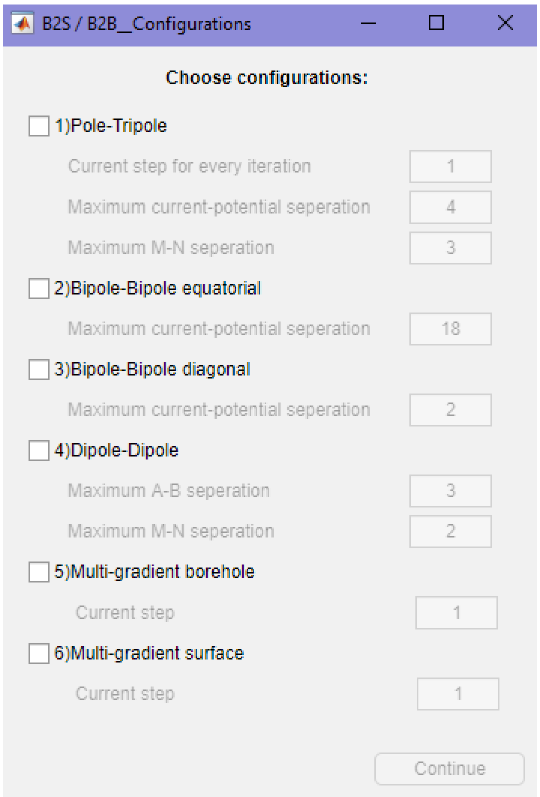

B2S / B2B_Configurations

Choose configurations:

☐ 1)Pole-Tripole

Current step for every iteration	1
Maximum current-potential seperation	4
Maximum M-N seperation	3

☐ 2)Bipole-Bipole equatorial

Maximum current-potential seperation	18

☐ 3)Bipole-Bipole diagonal

Maximum current-potential seperation	2

☐ 4)Dipole-Dipole

Maximum A-B seperation	3
Maximum M-N seperation	2

☐ 5)Multi-gradient borehole

Current step	1

☐ 6)Multi-gradient surface

Current step	1

Figure 3.8: Configuration window. The user selects the desired configurations.

measurements is calculated depending on the chosen configurations and the variables that the user can interfere with. This matrix contains the ID of the four electrodes utilized each time for the measurement.

3.2.3 Geometric factor / Sensitivity error

Then, the user can eliminate some measurements due to geometric factors (Figure 3.9). This can be realized with two options. The user can input an arbitrary threshold value or calculate the threshold with equation 3.1, in which case some more variables should be added. When clicking the 'Reject measurements' button, all the measurements with higher threshold values are dismissed, and their percentage is shown. The user can also choose whether the rejection of some more measurements due to sensitivity error will be applied. The relative error value (Re) of each quaternary measurement appears in the histogram, and then the user can choose a threshold that will be deemed reasonable to dismiss all those values that are out of charts. Again, the percentage of the rejected measurements can be seen.

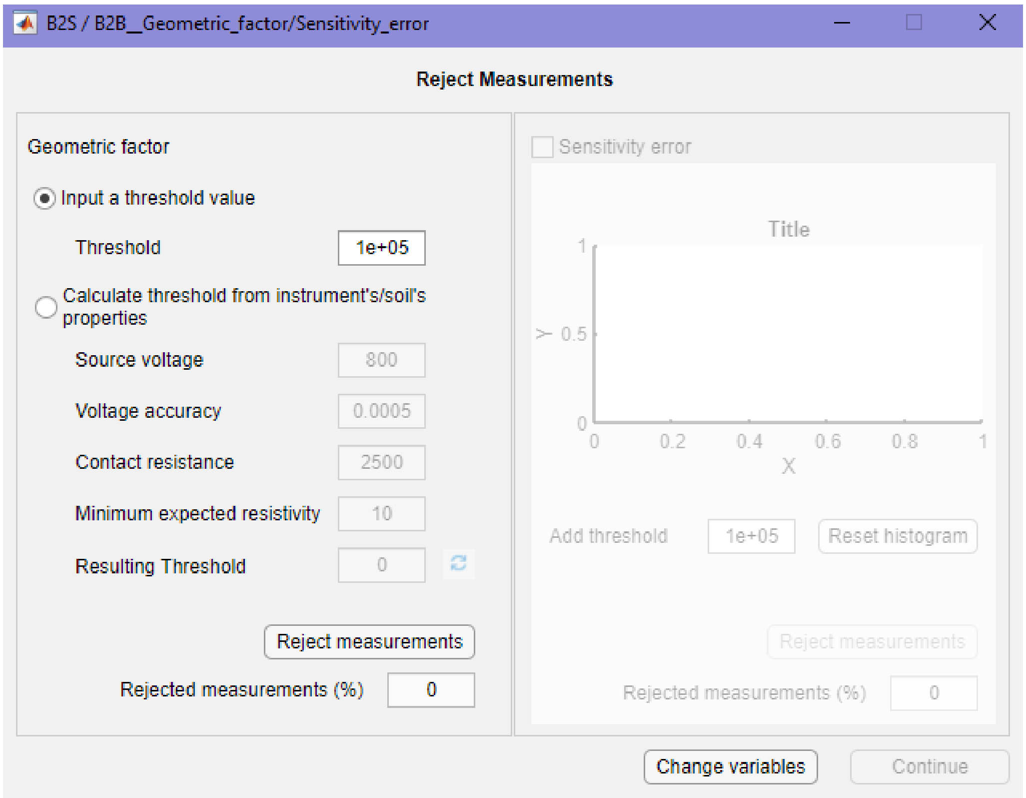

B2S / B2B__Geometric_factor/Sensitivity_error

Reject Measurements

Geometric factor

● Input a threshold value

Threshold: 1e+05

○ Calculate threshold from instrument's/soil's properties

Source voltage: 800

Voltage accuracy: 0.0005

Contact resistance: 2500

Minimum expected resistivity: 10

Resulting Threshold: 0

Rejected measurements (%): 0

☐ Sensitivity error

Add threshold: 1e+05

Rejected measurements (%): 0

Figure 3.9: Geometric factor and sensitivity error window, where the user can eliminate some of the measurements.

3.2.4 Jacobian calculation

The next step is to calculate the Jacobian matrix (Figure 3.10). Once again, there is a choice between using the default grid or creating a new one. In the first option, the resolution of the cartesian grid affects the step for the in-between points. For example, if the 0.5 resolution is chosen, it will produce approximately quadripole points compared to selecting "resolution 1". The second choice was added because the default grid might not be preferable since the geometries that may be used are theoretically unlimited. The user, depending on the electrode coordinates, needs to input the minimum desired «x» and absolute «z» value to indicate the top left corner of the grid, the step for the calculation of the in-between points and finally, the desired maximum «x» and absolute «z» value for the completion of the grid. The minimum «x» value does not have to be equal to the exact coordinates but may be smaller to cover the surrounding area. The same is applied to the maximum values.

Then, the Jacobian matrix is calculated following the selected parameter's elimination. The rejection degree depends on the user and how strict or not the chosen threshold would be. The presented examples in the following chapter use three different thresholds: a) low threshold, where only a few points are eliminated (10% of the median cumulative Jacobian), b) medium, where the threshold is set to be 50% of the median cumulative Jacobian and c) a high threshold where the median cumulative Jacobian is multiplied by 1.5 and much more points are dismissed.

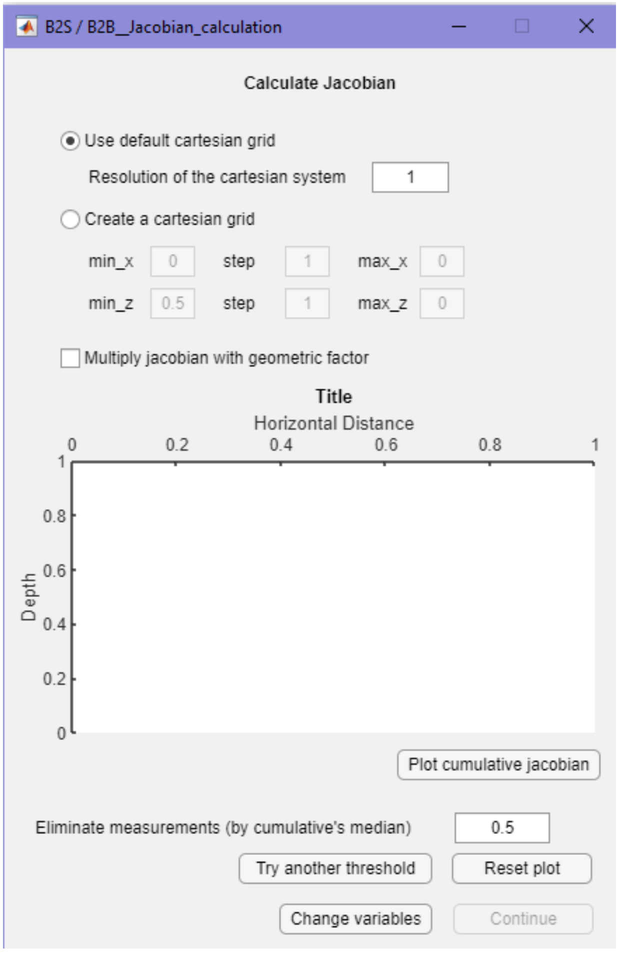

B2S / B2B_Jacobian_calculation

Calculate Jacobian

● Use default cartesian grid

Resolution of the cartesian system: 1

○ Create a cartesian grid

min_x: 0 step: 1 max_x: 0

min_z: 0.5 step: 1 max_z: 0

☐ Multiply jacobian with geometric factor

Eliminate measurements (by cumulative's median): 0.5

Figure 3.10: Calculation of the Jacobian matrix window. The Jacobian matrix is calculated for the desired grid and some of the parameters can then be eliminated to define a more restricted area.

3.2.5 Optimization

Optimization is the process after which the final protocol contains only those measurements of the entire protocol that are considered more valuable and necessary for depicting the targets in the investigated area. In Figure 3.11 the generated window for the optimization is presented. The user can choose between the three available percentages and how the parameters will be assigned into clusters (linear or quasi-linear option). Then follows the plot of the cumulative Jacobian of the optimized dataset. Sometimes, with this way of cluster calculation, the resulting cluster may be 1, which is not preferable, and to avoid this, a less dense grid (fewer parameters) should be employed, or perhaps some of the choices could be altered.

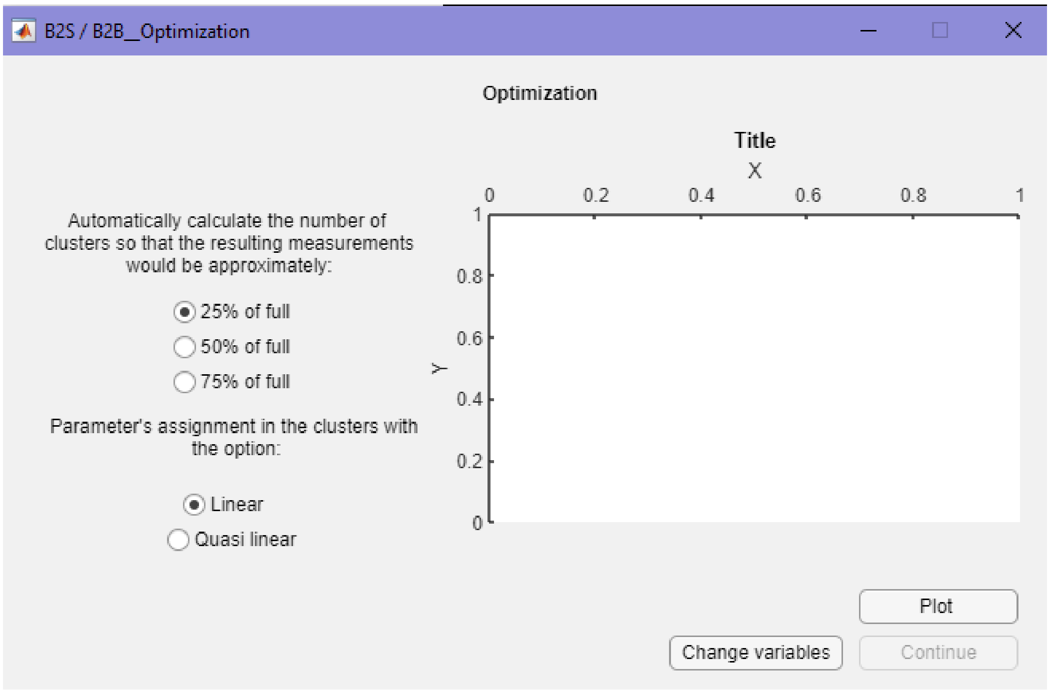

Automatically calculate the number of clusters so that the resulting measurements would be approximately:

● 25% of full
○ 50% of full
○ 75% of full

Parameter's assignment in the clusters with the option:

● Linear
○ Quasi linear

Figure 3.11: Optimization window.

3.2.6 Save

After all these processes, the user can finally save the full and optimized files (Figure 3.12). The user has to input some further information that will be valuable. One is the region's name that will be referred to in the produced files.

The number of «skipped cable_2 electrodes» is related to the cable connected to the second borehole electrodes or perhaps to surface electrodes. As already mentioned, the numbering of the ID's starts at the bottom of the first borehole and goes up to the last surface electrode or the electrode of the second borehole. But if it is impossible to insert the cable in the second borehole fully and some of the cable outputs remain outside, a problem in the numeration will appear. That's why a variable is used to skip these electrodes.

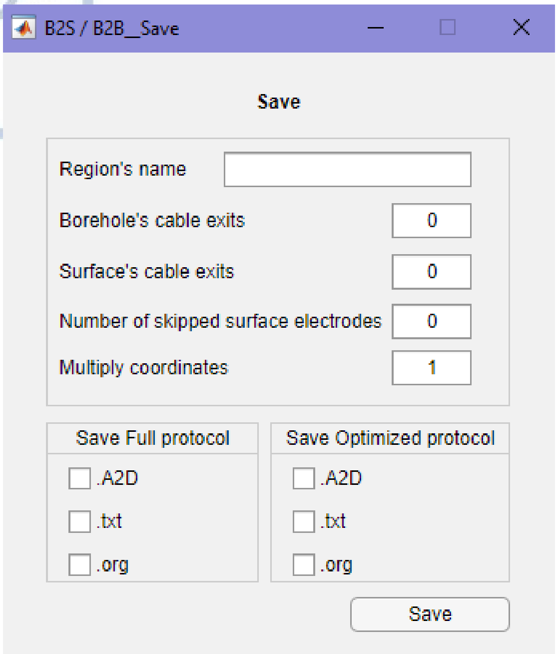

Save

Region's name

Borehole's cable exits 0

Surface's cable exits 0

Number of skipped surface electrodes 0

Multiply coordinates 1

Save Full protocol
- ☐ .A2D
- ☐ .txt
- ☐ .org

Save Optimized protocol
- ☐ .A2D
- ☐ .txt
- ☐ .org

Figure 3.12: Save window. The generated files are saved.

3.3 Data processing

Each instrument recognizes a specific format, so the uploaded protocols should be compatible with this form. As mentioned above, the available exports of the algorithm are *.a2d, *.org and *.txt files of the full and optimized data following an appropriate format. To acquire the measurements for the Syscal pro instrument, this generated *.txt file must be converted to a protocol (*.sqz) readable by the instrument. This is feasible with the upload of the *.txt file on the Electre Pro Software, where the user can also interfere with different parameters. One of them is the allowance of gap fillers. With the selection of «creation of standard sequence», the generated protocol is in the appropriate format to be uploaded to the instrument.

After that, the measurements are obtained. With the completion of the data acquisition, the type of file exported from the instrument is *.bin. This information is downloaded using another processing software, the Prosys II. This software displays all the measurements with the positions (x, y, z) of each electrode (A, B, M, N) and the resistance, the deviation, the potential difference, the injected current of each measurement, etc. These can be submitted to an initial process. For instance, the deletion of the gap-fillers inserted in a previous step should occur, since they are not actual measurements and the extermination of bad data could make the provided information more optimal. An example of the application of the extermination of "bad" data is shown in Figure 3.13, where some of the deleted data that seem to diverge from the gathered points appear in red.

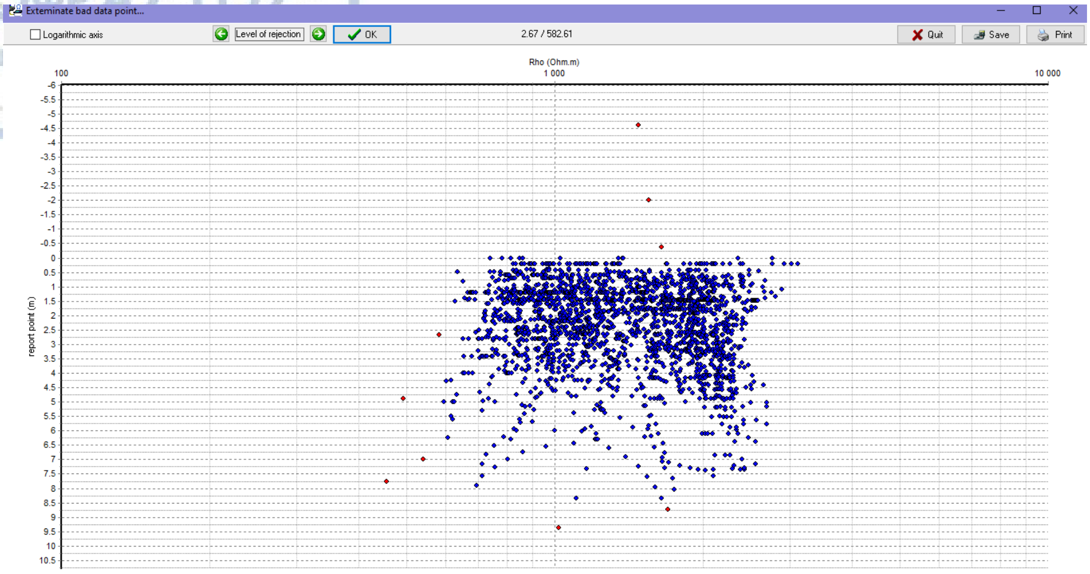

Figure 3.13: Data proccessing, bad data extermination using the software Prosys II.

Since the *.bin file is not readable from the software that will be used for the inversion (DC_2DPro), another process should occur. An algorithm was coded in Matrix Laboratory based on an existing available algorithm. Taking this code and making some adjustments, the *.bin files that include the desired information could be read, and the apparent resistivity of each measurement could be determined. The exported file of this algorithm is of type *.A2D that is readable from the DC_2DPro inversion software. Also, another algorithm was created for the optimized protocol to retrieve only the resistivity values that correspond to the optimized measurements from the full protocol since only the full protocol was measured in the field.

4. EVALUATION WITH SYNTHETIC AND EXPERIMENTAL DATA

This chapter includes the evaluation of the protocols produced with the algorithm over synthetic and experimental data. After creating the exported files, using all the available configurations, they were tested before applying the algorithm to real data. So, many synthetic models of various geometries went through the inversion process to test the effectiveness of the full and optimized datasets in locating different targets. Three different threshold values for the defined area of sensitivity and three different optimized datasets were created for each geometry to determine which would be the most appropriate. Finally, some models were tested in an experimental tank in the lab to investigate the algorithm's applicability in models where the conditions are not ideal, like in the synthetic models, and noise may affect the results.

4.1 Synthetic models

After the generation of the algorithm, the results of the full and optimized protocol had to be tested. For this reason, some synthetic models were created and inverted using the DC_2DPro software. The process of this evaluation is the following. The *.a2d files of the full and optimized measurements are inserted into the software. Then, the user can modify the half-space by adding modelling properties, e.g., bodies, layers or other formations that could have geological significance with various resistivity values. This model should be the final “image” after the inversion of full and optimized data. The models were examined over the defined area of sensitivity, the number of the final optimized data and the behaviour of different geometries and targets were tested. Many models were assessed, but only some of them will be presented and discussed.

Models with the same geometry will be examined for different threshold values (low, medium, high) and three optimized datasets (approximately 25%, 50% and 75% of the full). For these models, 20 surface and 20 borehole electrodes with a spacing of 5m were considered. The borehole’s inclination, defined clockwise from the surface, is 30° with the first electrode at 10m depth. In a half-space with resistivity 100 Ohm-m, there are 3 conductive blocks (10 Ohm-m) (Figure 4.1 a-c). The first and the second blocks are in the same position for the three models, but the location of the third one is altered. The first one is at 5m depth and 15m horizontal distance, having dimensions 5x5m. The second is at 40m depth and 35m horizontal distance, measuring 15x15m. The third one, with dimensions 20x20m, is placed in three different locations a) 15m depth / 70m horizontal distance, b) 25m depth / 70m horizontal distance and c) 20m depth / 75m horizontal distance, to evaluate the capability of the optimized datasets with different threshold values to detect it. The blue colour bar of Figure 4.1, indicates the low resistivity areas (i.e., the conductive blocks) whereas the lilac, red colour, shows the high resistivity areas (i.e., the half-space).

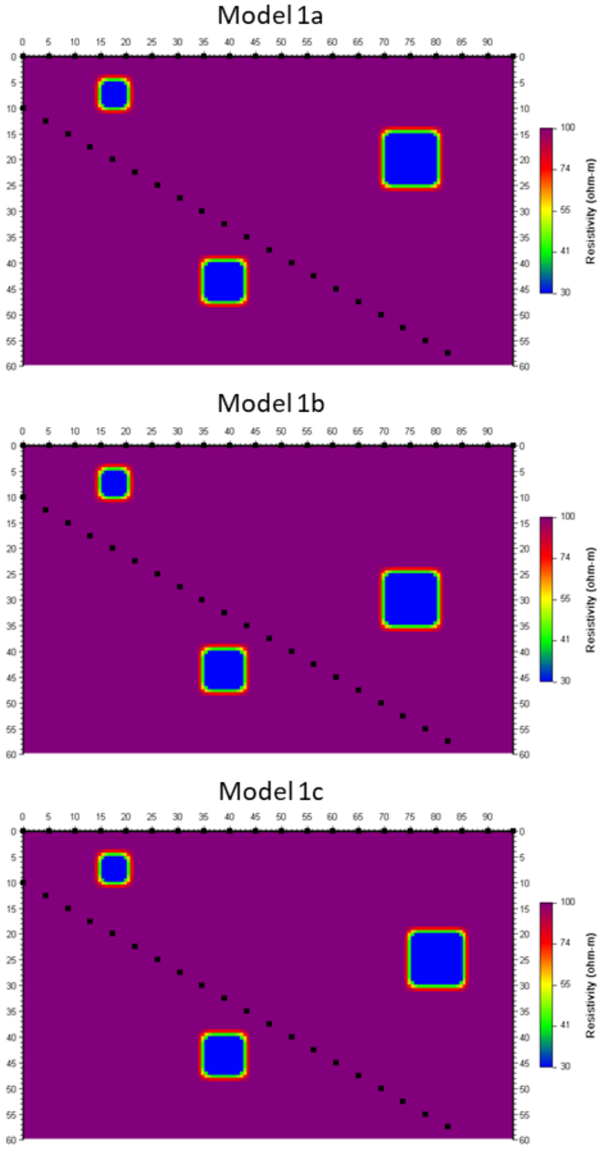

Figure 4.1: Synthetic model 1 with a resistive half-space of 100 Ohm-m and three conductive blocks (10 Ohm-m). The first block of dimensions 5x5m is positioned at depth z=5m and horizontal distance x=15m, the second block (15x15m) is at z=40m and x=35m and the third one (20x20m) is situated in three positions a) z=15m, x=70m, b) z=25m, x=70 and c) z=20m, x=75m.

The inverted results of the full and the three optimized protocols with the three threshold values of each model (Figure 4.1 a-c), with 6 iterations and the L1 norm option at DC_2DPro, are shown in Figure 4.2, 4.3 and 4.4, respectively. In each figure, on the left, the synthetic model appears and follows the inverted results of the full protocol with 9202 measurements. Each of the three columns corresponds to the same percentage of optimized data, containing approximately the same number of measurements and each row to a specific threshold value. At the top of each figure, the number of measurements and the used clusters are mentioned. The areas noted with a grid in the optimized models correspond to the assumed trusted areas of each one of the thresholds (low, medium, high). Also, the

% difference in the inverted image of the full and each optimized protocol compared to the original synthetic model was calculated. The values are shown in the highlighted at the top right box of each figure.

Model 1a:

For this model (Figure 4.2), with the increasing percentage of the optimized datasets, the number of measurements rises, and the image (75% of the data) tends to resemble the results of the full protocol more. Also, with this increase in the measurements, the artefact that appears near the third block is not intense. The models with 50% of the data also manage to achieve a valid representation. Since the measurements are approximately 50% less, acquiring them would theoretically take half the time in the field. The models with 25% data can locate the third block (on the right), but its boundaries are not well identified, and this percentage should not be preferred for this environment. The % difference values between the models also confirm these conclusions since the difference rate decreases as we move to the optimized protocol of 75%.

As for the threshold, it seems that as it proceeds to higher values, more measurements participate, but without an apparent improvement in the results. On the contrary, the targets appear weaker, especially at the bottom and on the right. This is visible to both 25% and 50% optimized datasets, whereas on the 75%, the difference is not so noticeable. Except for these subtle changes, the different threshold values do not seem to affect the inversion process significantly since the targets in some models are reconstructed, although they are placed out of the supposedly trusted area. Despite that, the threshold could be valuable in determining which of the proposed trusted areas is more appropriate for each geometry. For this specific geometry only, it is apparent that the low threshold is the best fit since all the targets are included in the specified area, and the artefact is excluded. The other thresholds are stricter and eliminate points in regions that are trustworthy.

Model 1b:

For this position of the third block (Figure 4.3), it appears that none of the models can depict the boundaries of the third block as clearly as they did in their first position. This probably occurs because the target is far from the surface electrodes. The models compared to each other do not differ significantly. Still, once again, the models with the high threshold produce a weaker reconstruction even though they manage to detect the blocks. This is also evident by the calculated % errors between the original and reconstructed models. Also, the 50% and 75% models have better resolution since more measurements are employed. The artefact on the right is not so intense relatively to model 1a, and once again, it tends to get weaker as the percentage increases.

Model 1c:

In this position (Figure 4.4), the third block is not depicted as accurately as in the previous models, not even in the full protocol. There is an artefact attached to it that alters entirely its boundaries. The optimized 50% and 75% datasets can locate the target more clearly without apparent variability between the different thresholds. Also, the percentages that show the % differences of each optimized protocol with the initial synthetic model are similar, except for the optimized protocol of 25%, especially with the medium and high threshold, which provides more increased values and fails to identify the block’s shape. This model shows that a part of the block crosses the untrusted area, as the low threshold indicates, and for this reason, an artefact appears attached to it and could be mistaken as an actual target.

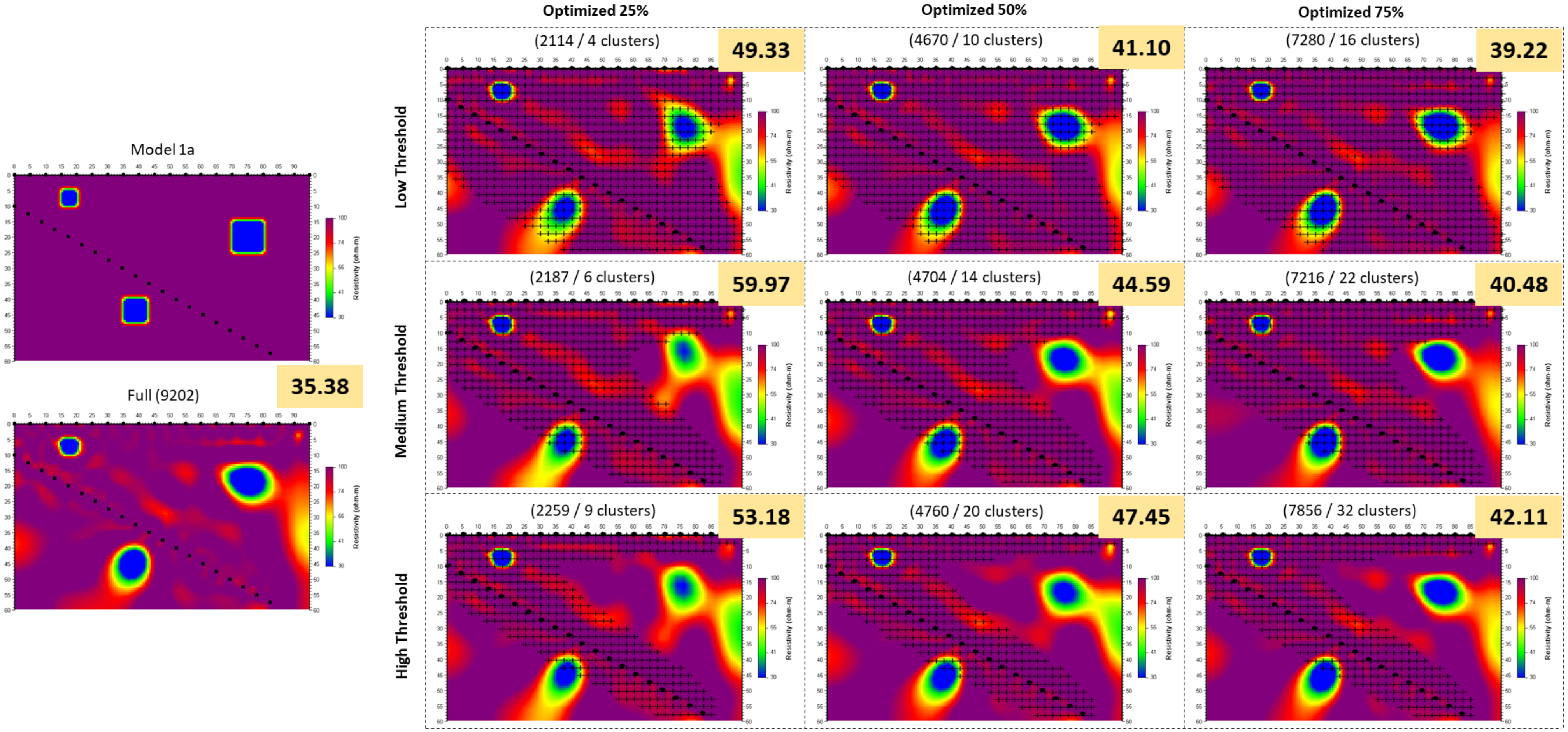

Figure 4.2: Inverted results of the full protocol of model 1a and three optimized datasets (25%, 50%, 75% of the full) with three thresholds (low, medium, high). On top of each model there is the number of measurements and the clusters used for the optimization. The noted area in the optimized models corresponds to the area of sensitivity of each threshold.

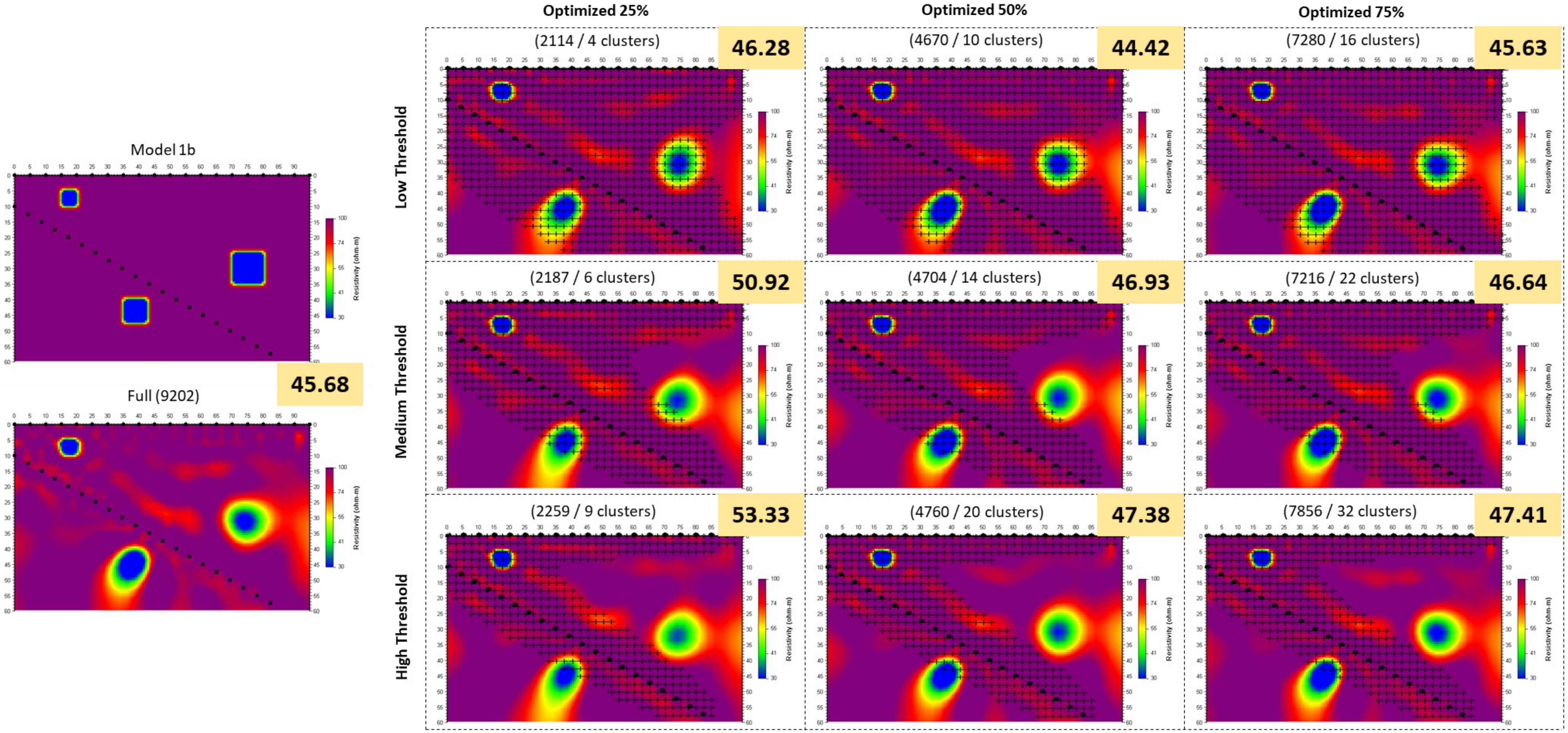

Figure 4.3: Inverted results of the full protocol of model 1b and three optimized datasets (25%, 50%, 75% of the full) with three thresholds (low, medium, high). On top of each model there is the number of measurements and the clusters used for the optimization. The noted area in the optimized models corresponds to the area of sensitivity of each threshold.

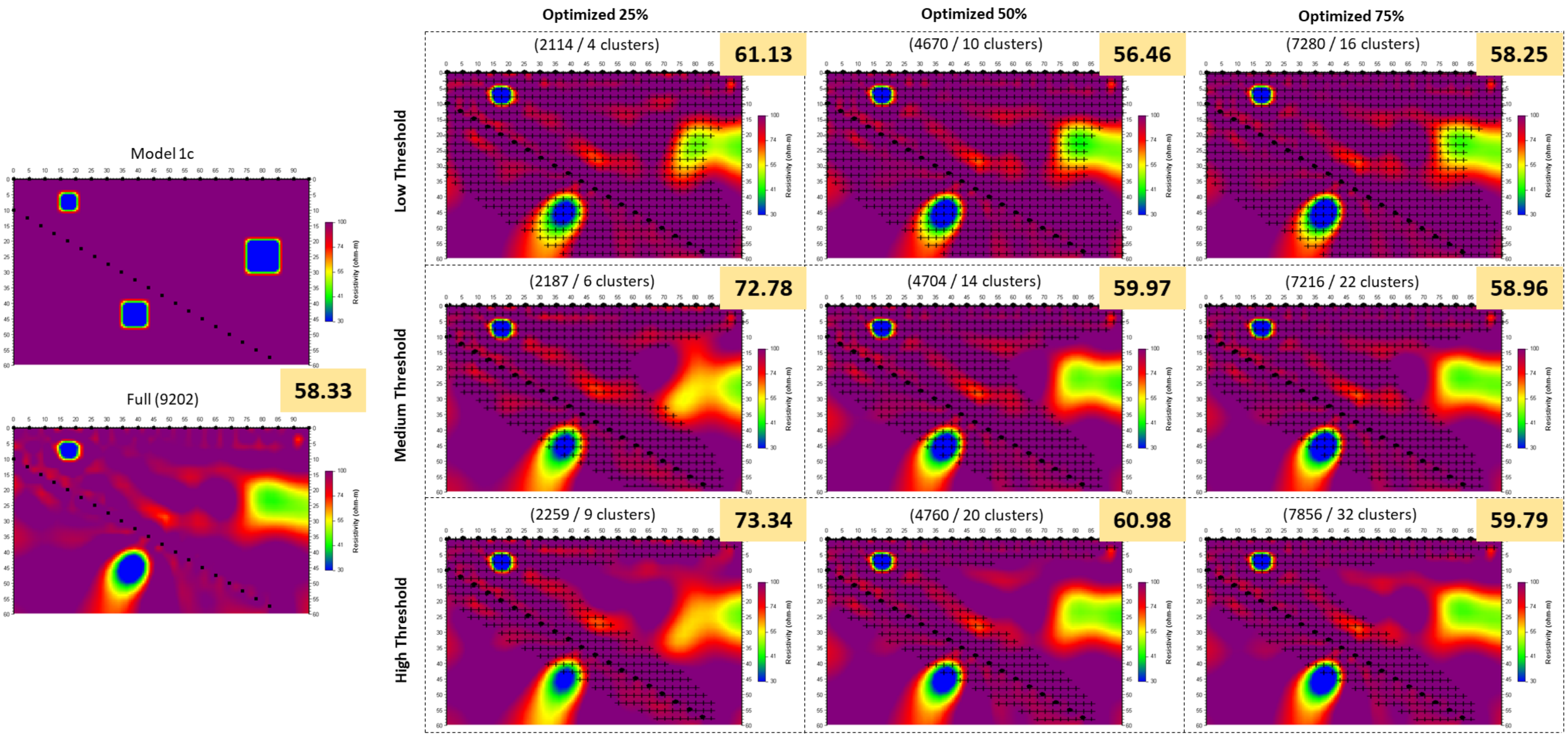

Figure 4.4: Inverted results of the full protocol of model 1c and three optimized datasets (25%, 50%, 75% of the full) with three thresholds (low, medium, high). On top of each model there is the number of measurements and the clusters used for the optimization. The noted area in the optimized models corresponds to the area of sensitivity of each threshold.

For the same geometry, another synthetic model (model 2) was created (Figure 4.5 a-c), but this time, with a conductive half-space (50 Ohm-m) and resistive blocks (100 Ohm-m) of the exact dimensions and in the same positions as the above three models. These models aimed to examine the inversion behaviour in another geological background. The process was identical to that of the previous models.

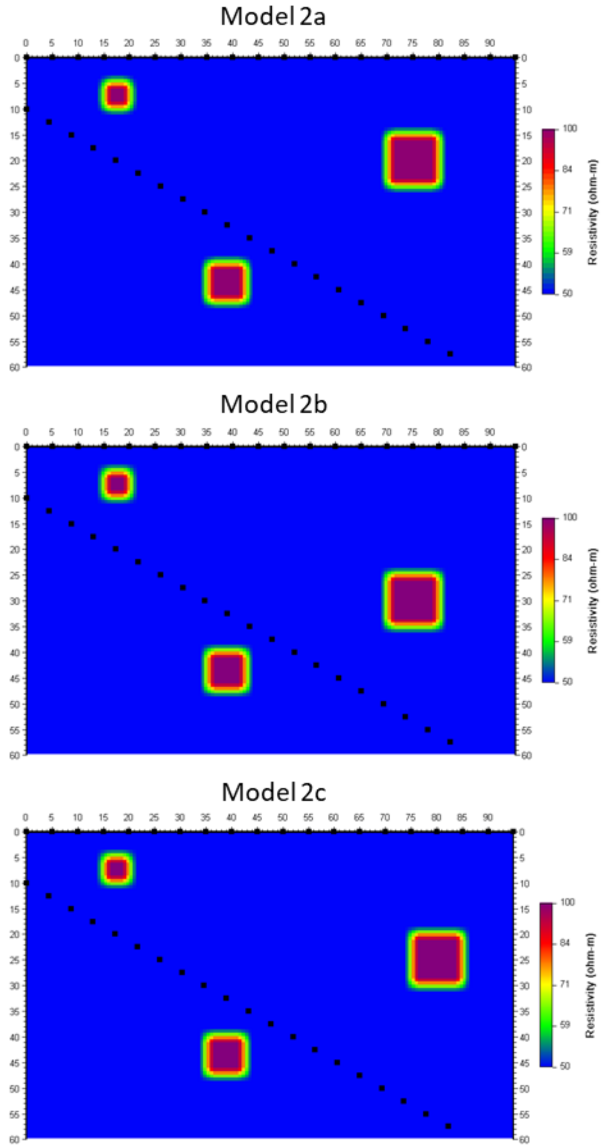

Figure 4.5: Synthetic model 2 with a conductive half-space of 50 Ohm-m and three resistive blocks (100 Ohm-m). The first block of dimensions 5x5m is positioned at depth z=5m and horizontal distance x=15m, the second block (15x15m) is at z=40m and x=35m and the third one (20x20m) is situated in three positions a) z=15m, x=70m, b) z=25m, x=70 and c) z=20m, x=75m.

<u>Model 2a</u>:

For this model (Figure 4.6), the targets seem to be reconstructed without being contaminated by artefacts. The first block, between and close to the surface and the borehole, is again detected accurately by all the models. All models locate the second block, but its boundaries are somehow disturbed. The third block is located in the correct position, but its shape is a bit blurred in the optimized dataset of 25%. The other datasets produce results very similar to the one obtained from the full protocol, with no noticeable differences between the three thresholds. This is also apparent in the percentage of the model difference, which is systematically much lower than in the errors observed for model 1, as fewer artefacts appear here.

Model 2b:

For this position of the third block (Figure 4.7), all models manage to locate the targets, but the third block is more weakly presented compared to model 2a. This probably happens due to the fact that this block is more distant from the surface electrodes. The different thresholds do not significantly affect the depiction of the targets, and only the optimized protocol of 25% with the high threshold provides blurrier results. We could assume, that all the optimized datasets with the low threshold, provide adequate results close to the full protocol.

Model 2c:

These models (Figure 4.8) struggle even more to locate the third block accurately and with discrete boundaries. Still, contrary to the first model (Figure 4.4), where an artefact appeared, and the target was distorted, the results are relatively better in this geological background. Furthermore, in those figures, the discrepancy between the different thresholds is more apparent with careful observation and with the assistance of the highlighted values that indicate the differences in the images. The most optimized datasets fail to detect the blocks finely, with only the optimized protocol of 50% with the low threshold managing to recreate the synthetic model adequately.

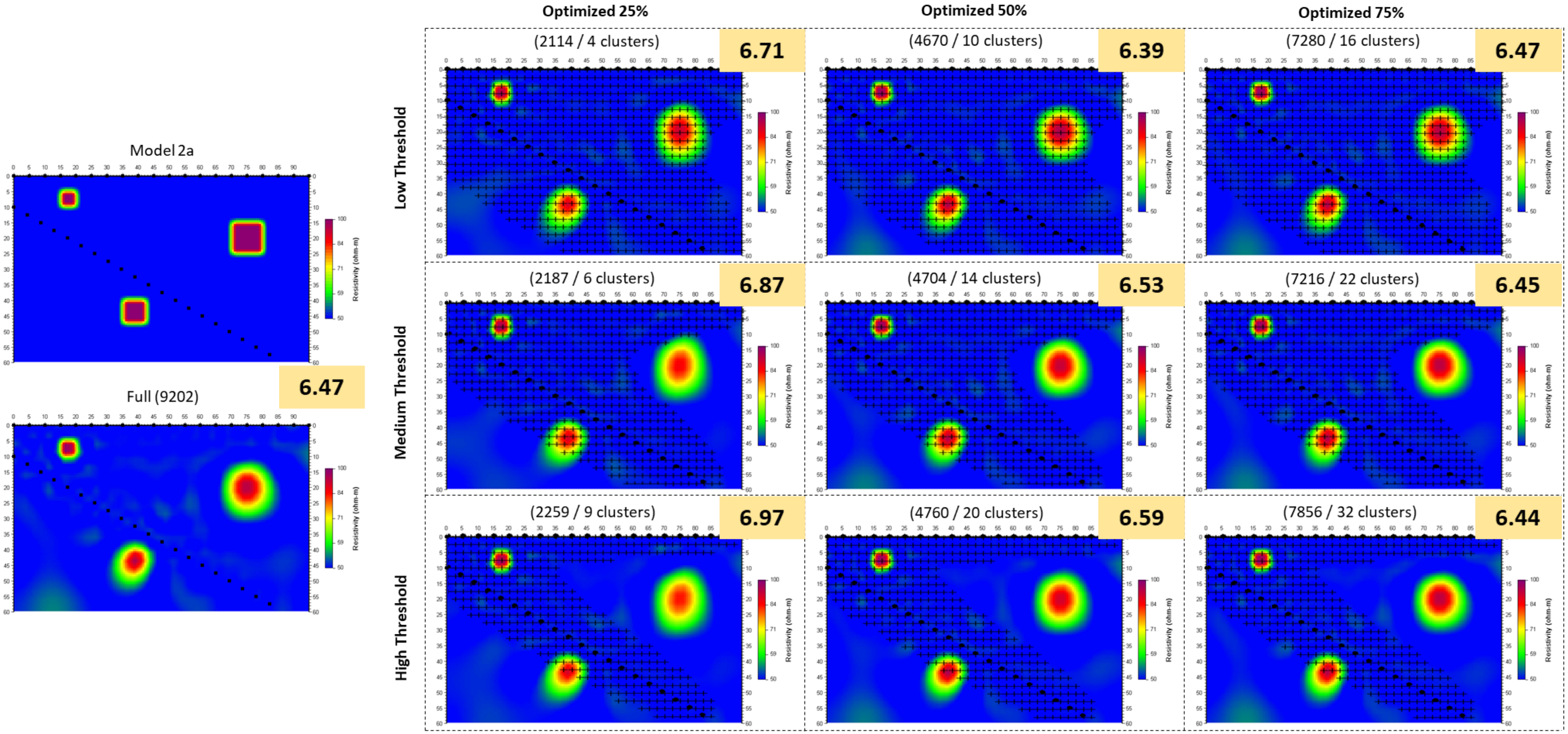

Figure 4.6: Inverted results of the full protocol of model 2a and three optimized datasets (25%, 50%, 75% of the full) with three thresholds (low, medium, high). On top of each model there is the number of measurements and the clusters used for the optimization. The noted area in the optimized models corresponds to the area of sensitivity of each threshold.

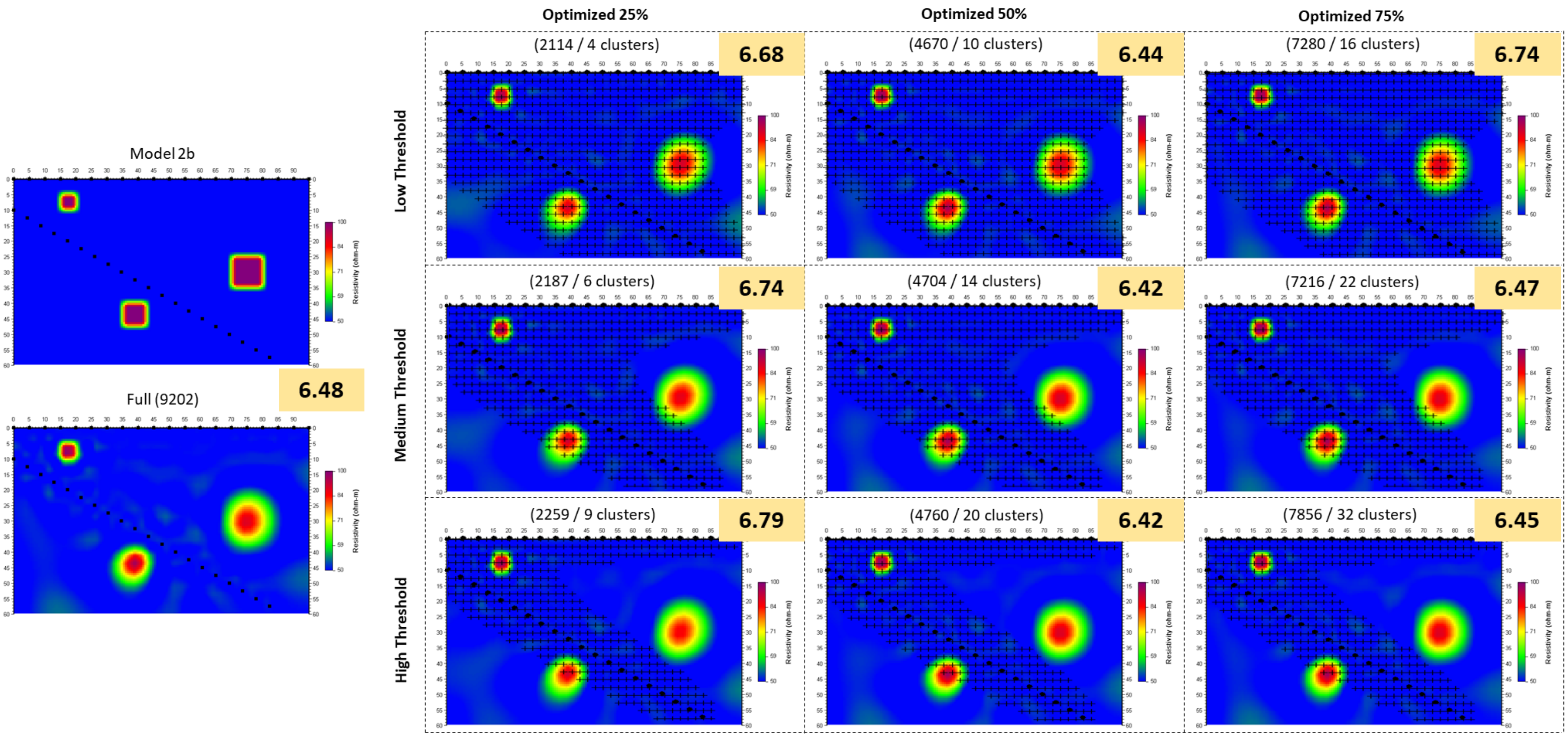

Figure 4.7: Inverted results of the full protocol of model 2b and three optimized datasets (25%, 50%, 75% of the full) with three thresholds (low, medium, high). On top of each model there is the number of measurements and the clusters used for the optimization. The noted area in the optimized models corresponds to the area of sensitivity of each threshold.

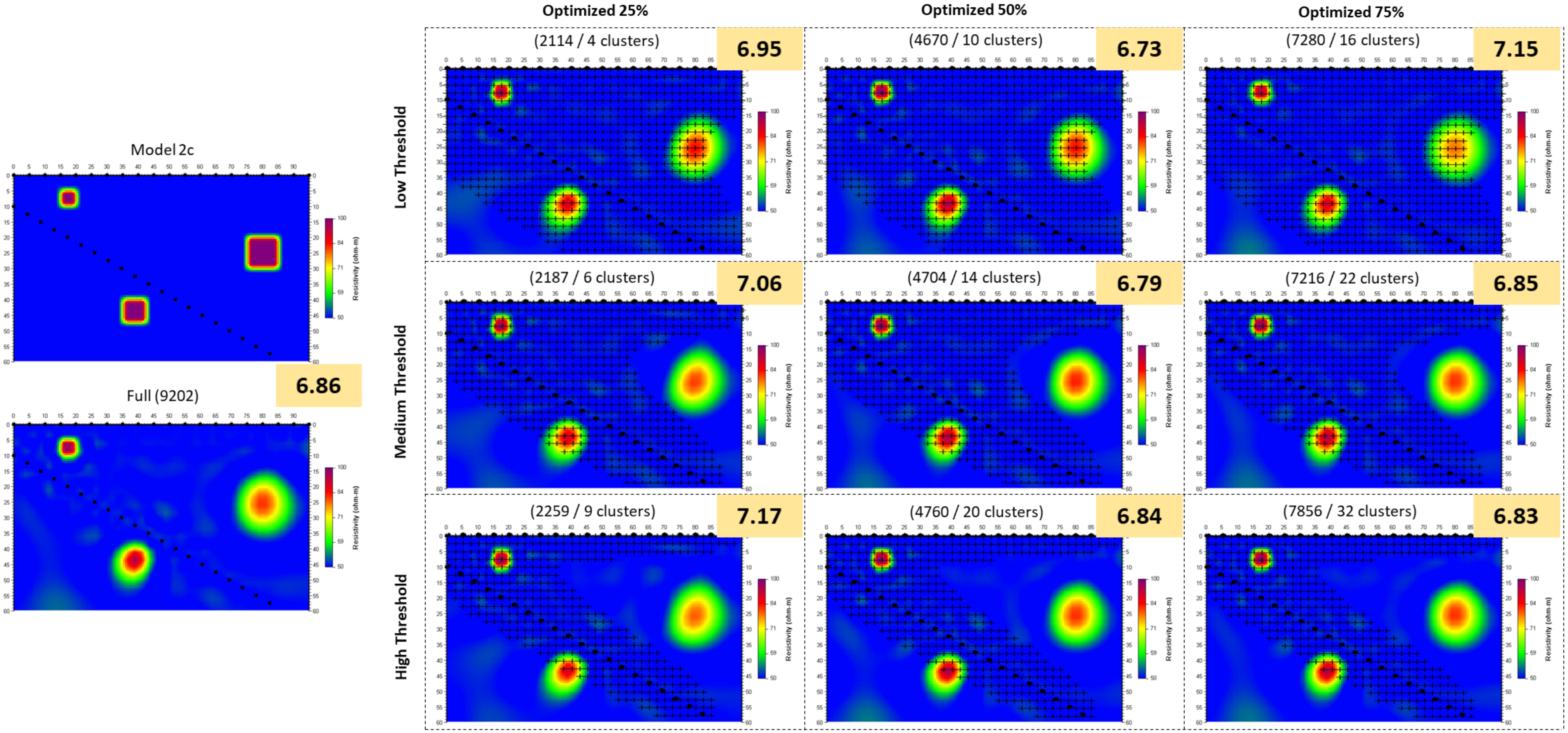

Figure 4.8: Inverted results of the full protocol of model 2c and three optimized datasets (25%, 50%, 75% of the full) with three thresholds (low, medium, high). On top of each model there is the number of measurements and the clusters used for the optimization. The noted area in the optimized models corresponds to the area of sensitivity of each threshold.

Two more models were examined except for models 1 and 2. The same geometry was applied for a more objective comparison. In a resistive half-space (100 Ohm-m), there is a conductive inclined layer (10 Ohm-m) starting at 10m depth and horizontal distance of 92.5m advancing towards the borehole until the depth of 60m or more (model 3, Figure 4.9). This layer could resemble a fault zone. Similarly, in a conductive half-space (50 Ohm-m) there is the same inclined layer, only this time it is resistive (100 Ohm-m) and could resemble a dyke (model 4, Figure 4.9). The inverted results of the full and the optimized models of 25%, 50% and 75% will be presented for the two models using the same three thresholds (low, medium, high).

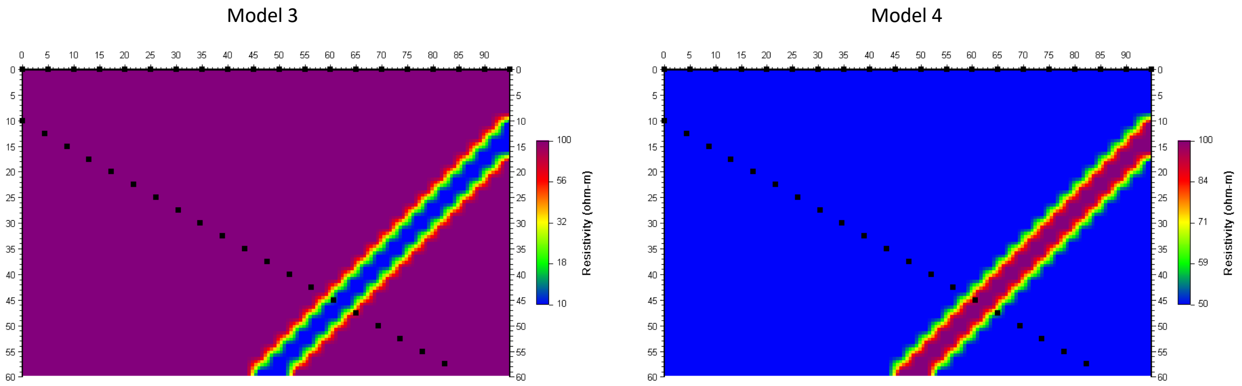
Model 3
Model 4

Figure 4.9: Synthetic models of a conductive line (10 Ohm-m) in a resistive half-space (100 Ohm-m) (Model 3) and a resistive line (100 Ohm-m) in a conductive half-space (50 Ohm-m) (Model 4).

Model 3:

From the inverted results of all the different models (Figure 4.10), it is evident that in the area where the “fault” crosses the borehole appears to be the most detailed representation of the target. In the region below the borehole and at some depth, the model fails to represent the “fault’s” continuation accurately. In the area above the borehole and between the surface, the continuation of the fault zone becomes blurrier at the part where it crosses the untrusted area, as indicated by the low threshold deemed more appropriate by the previous models.

Model 4:

In these models (Figure 4.11), the resistive target has a visibly better reconstruction quality than the previous conductive model. It seems that all the models fail to depict the “dyke” continuation at ~15-25m depth and ~80-85 horizontal distance, where it seems to be interrupted. Especially in the optimized results of 75%, the line appears more intensely split, creating a block at its swallower part, which could lead to false interpretation if the fact that this region is not to be trusted was not considered.

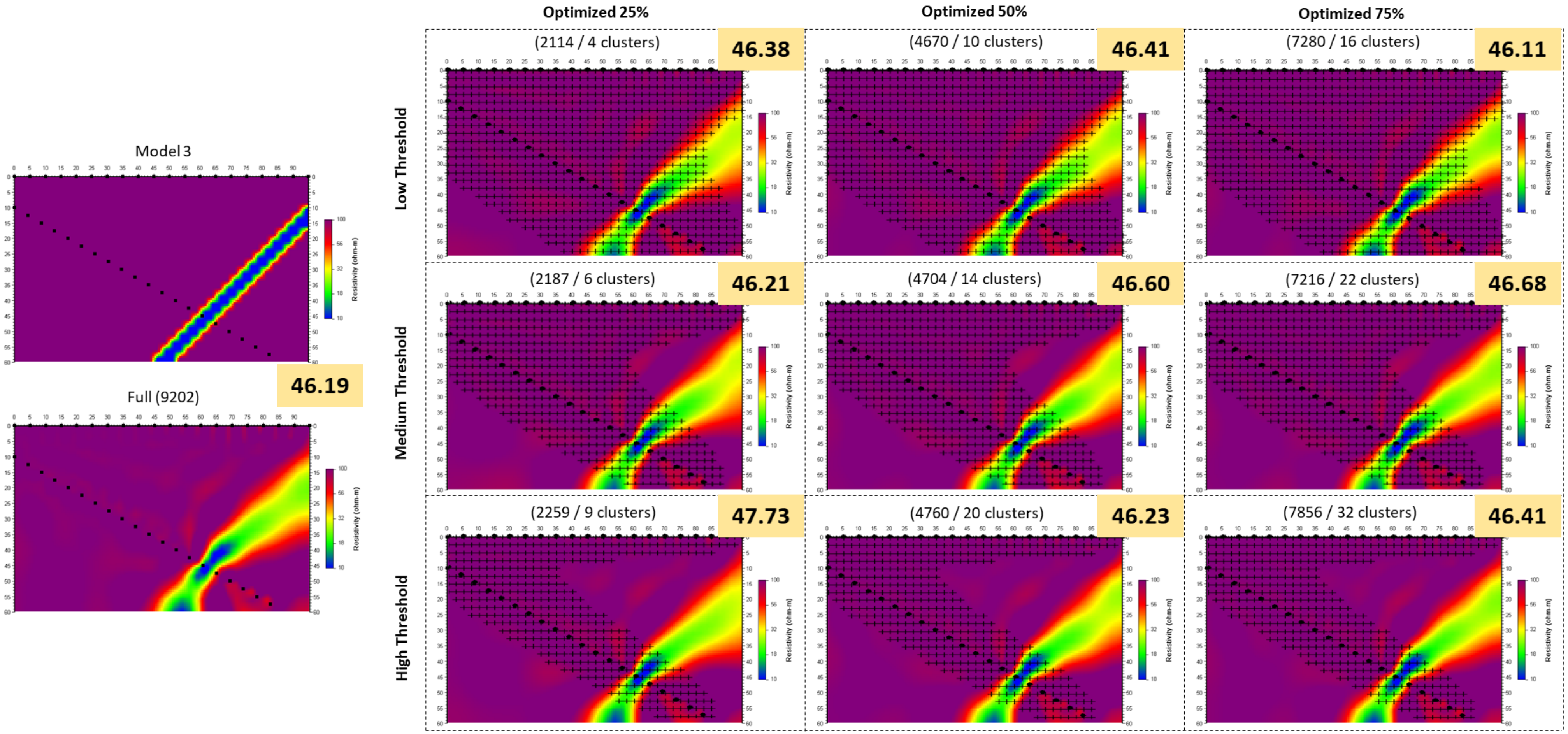

Figure 4.10: Inverted results of the full protocol of model 3 and three optimized datasets (25%, 50%, 75% of the full) with three thresholds (low, medium, high). On top of each model there is the number of measurements and the clusters used for the optimization. The noted area in the optimized models corresponds to the area of sensitivity of each threshold.

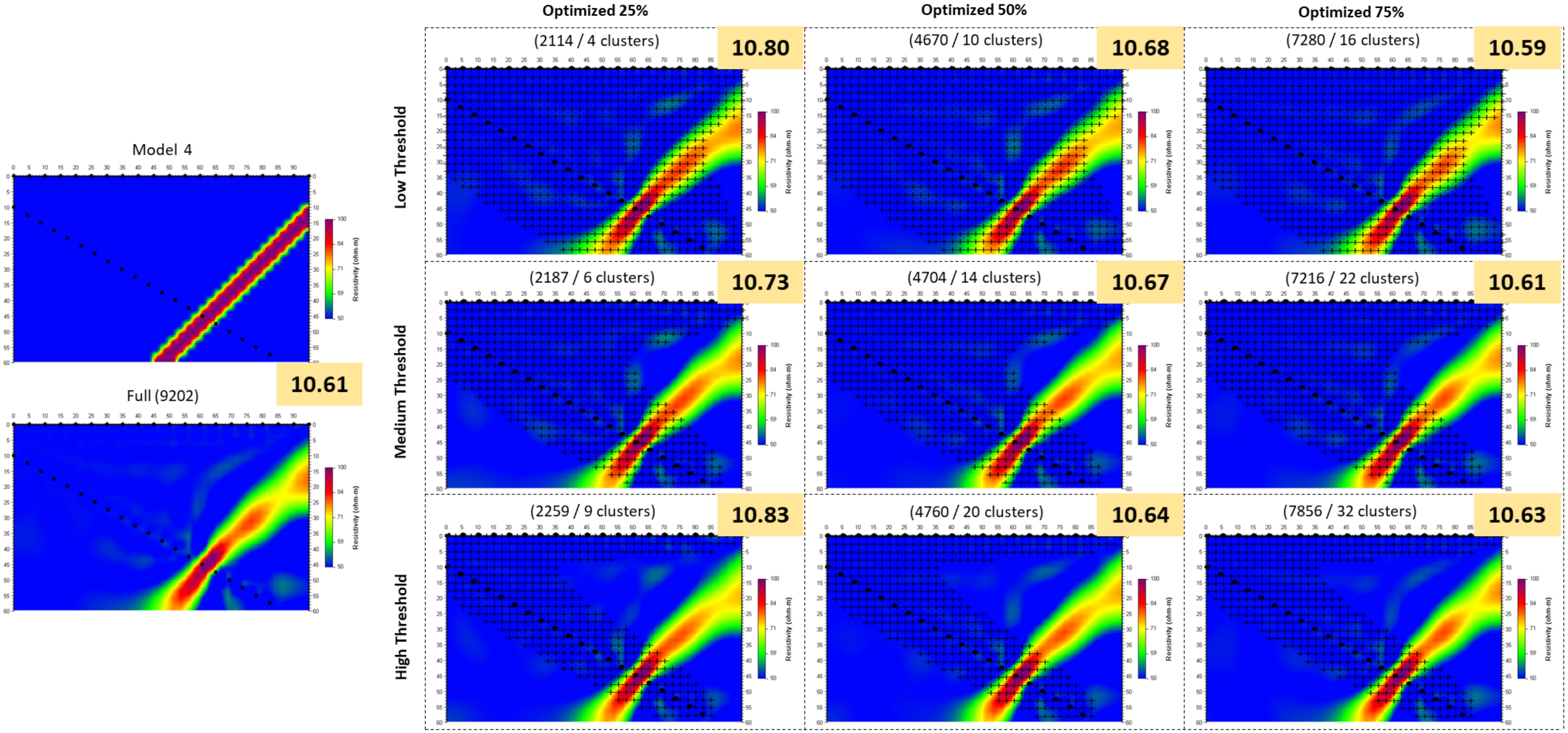

Figure 4.11: Inverted results of the full protocol of model 4 and three optimized datasets (25%, 50%, 75% of the full) with three thresholds (low, medium, high). On top of each model there is the number of measurements and the clusters used for the optimization. The noted area in the optimized models corresponds to the area of sensitivity of each threshold.

After evaluating these models over their defined area of sensitivity and the number of optimized measurements, an examination of the algorithm's flexibility for different geometries over the same geological background was deemed necessary. The model is a half-space with a resistivity of 500 Ohm-m, including a highly resistive (5000 Ohm-m) block with 10x10m at 10m depth dimensions. Also, two conductive formations (50 Ohm-m), starting from 5m depth and dipping with a random inclination, are included. The electrodes used are 40 altogether, 20 at the surface and 20 at the borehole, with a spacing 5m. The created optimized protocol for each geometry chosen to be presented, is this of 25%, to examine the «worst-case scenario» and the threshold value was the medium, as it was deemed preferable for the investigated geometries.

For the first geometry (Figure 4.12), the borehole was vertical, with the first electrode at 10m depth and 35m horizontal distance from the origin. The full protocol consisted of 10365 measurements. The resulting optimized protocol has 2492 measurements divided into 8 clusters. After the inversion of the data with 6 iterations and the L1 norm option at DC_2DPro, the results are shown in Figure 4.13 a-b.

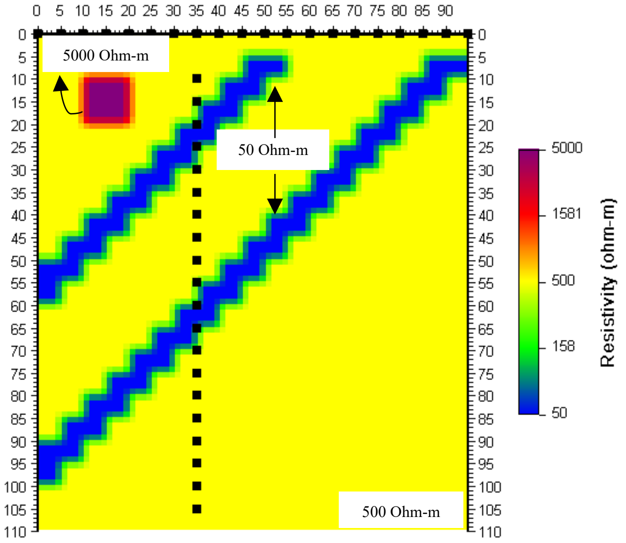

Figure 4.12: Synthetic model with half-space 500 Ohm-m, one resistive block (5000 Ohm-m) and two conductive lines (50 Ohm-m) resembling fault zones. The electrodes were placed with 5m spacing in the surface and at a vertical borehole.

Apparently, for this geometry, the areas with good sensitivity are at the first meters and around the borehole electrodes, where the targets are depicted more clearly. Both the full and optimized protocol detects the block and the fault zones especially in the areas where they cross the borehole electrodes. It is worth mentioning that around the borehole electrodes, some artefacts appear with resistivities a bit higher than expected. Similar artefacts are created below the fault lines. So, before the interpretation, there should be a general consideration of the lightened areas of the investigated region.

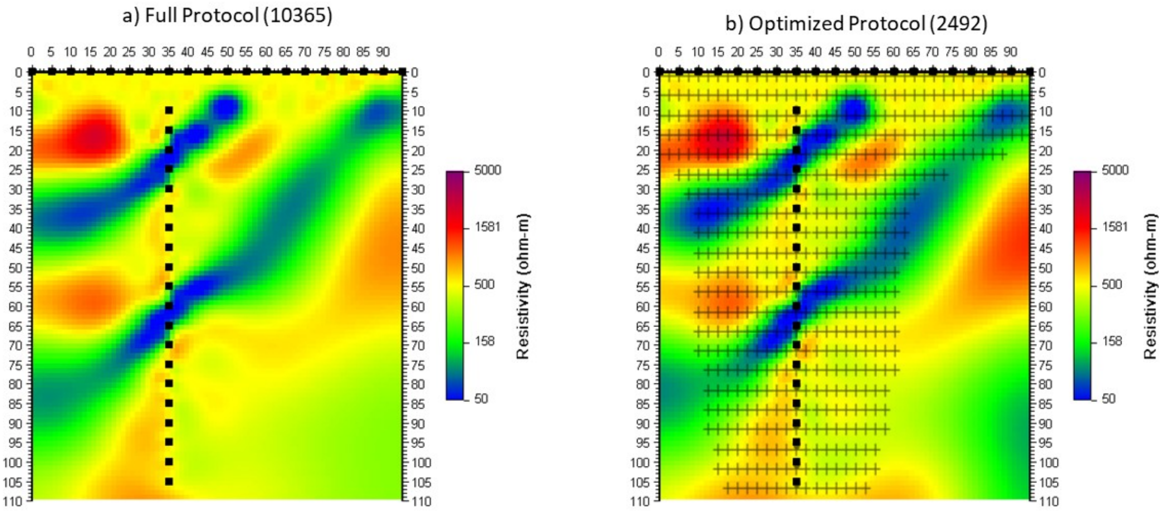
a) Full Protocol (10365)

b) Optimized Protocol (2492)

Figure 4.13: Inverted results of the a) Full and b) Optimized protocol.

Another geometry that was used with the same model is this of Figure 4.14, where there are two boreholes of the same inclination (40°) over a horizontal distance of 25m, with 20 electrodes each and 5m spacing between them. Their first electrodes were at 10m depth. The full protocol had 8936 measurements and the optimized 2252, divided in 8 clusters with the linear option. After the inversion with the abovementioned properties, the full and optimized results are shown in Figure 4.15 a-b.

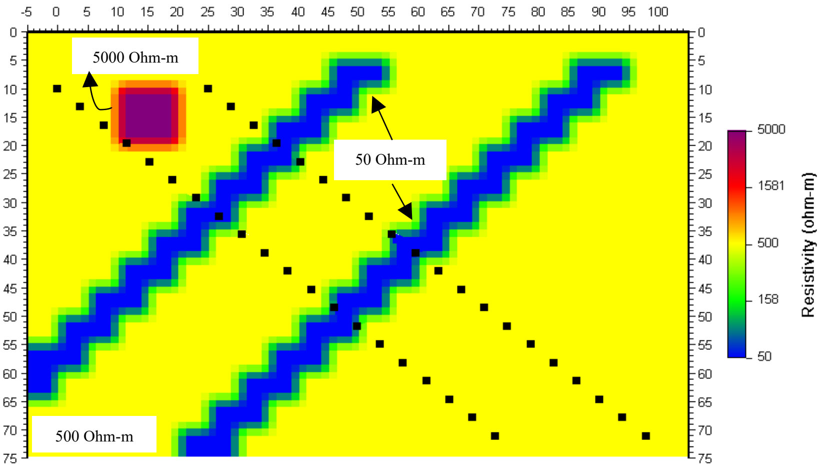

Figure 4.14: Synthetic model with half-space 500 Ohm-m, one resistive block (5000 Ohm-m) and two conductive lines (50 Ohm-m) resembling fault zones. The measurements took place in two parallel boreholes with inclination 40°.

For this geometry, the trusted area is expected to be mostly between the two boreholes and very closely around them. Once again, the targets are visibly detected with high accuracy both in the full and optimized data, especially in the regions where the fault lines cross the borehole electrodes, while at a greater distance from the borehole, the continuation of the layers is not accurately depicted. The sensitive area appears more restricted this time due to the implemented geometry. The optimized protocol impressively resembles the entire protocol with only a few visible discrepancies, so it may be assumed that for this specific geometry, the «worst-case scenario» is more than capable to detect the targets accurately.

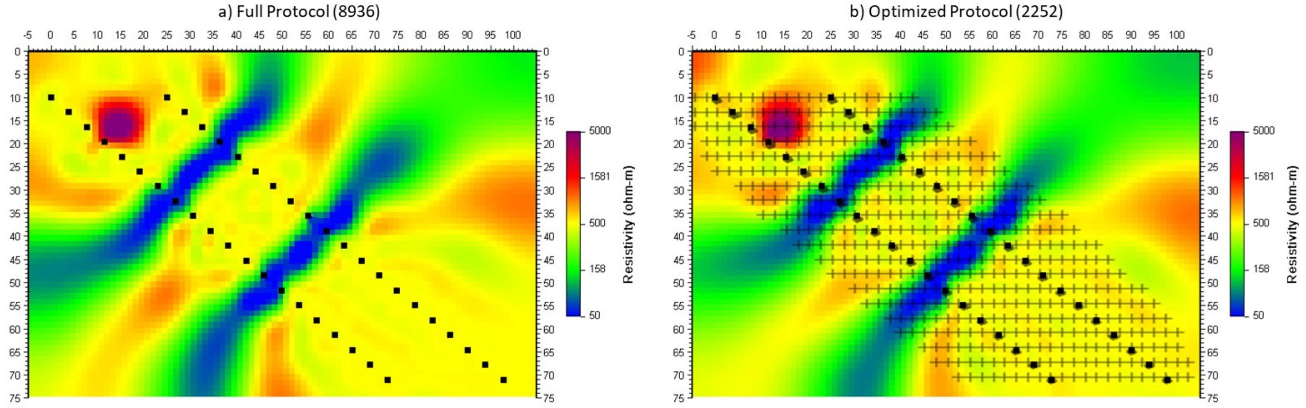
a) Full Protocol (8936)

b) Optimized Protocol (2252)

Figure 4.15: Inverted results of the a) Full and b) Optimized protocol.

Also, another geometry was implemented with the borehole horizontal and at a vertical distance of 25m from the surface electrodes (Figure 4.16). For this geometry, the full protocol had 9542 final measurements, and the optimized protocol of 25% had 2120, divided into 2 clusters with the linear option. The inverted results of the full and optimized protocol, with the same inversion properties as the other models, are shown in Figure 4.17.

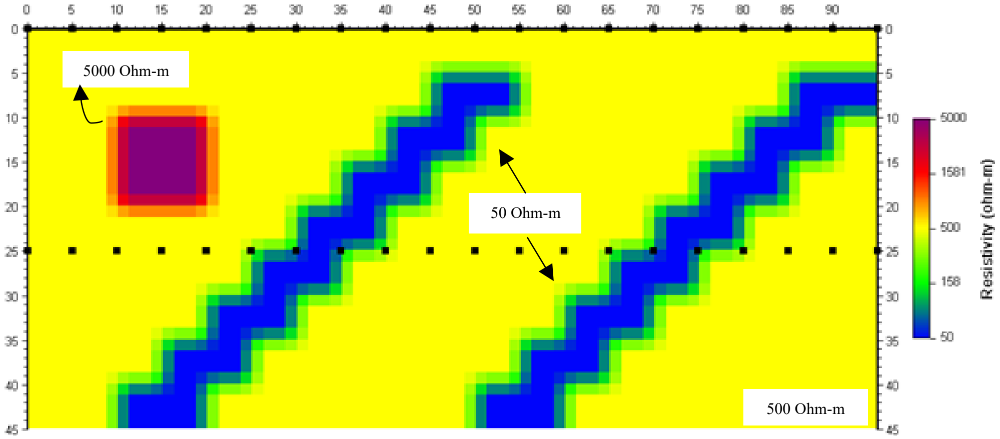

Figure 4.16: Synthetic model with a half-space of 500 Ohm-m, one resistive block (5000 Ohm-m) and two conductive inclined layers (50 Ohm-m) resembling fault zones. The measurements occurred between the surface electrodes and a horizontal borehole's electrodes, that had a vertical distance of 25m from the surface.

For this geometry, the expected area of high resolution is between the borehole and the surface. This is also apparent since the DC_2DPro software proposes the depth of investigation at 30m and excludes the greater depths. Both the full and the optimized protocols manage to detect the targets quite accurately (Figure 4.17). The optimized protocol of 25% was created with a medium threshold. Since the previous models showed that the threshold value does not affect the inversion significantly, the trusted area of the model was deemed the one depicted in the figure and results from using a less strict threshold that eventually shows as trusted, all the area between the electrodes.

a) Full Protocol (9542)

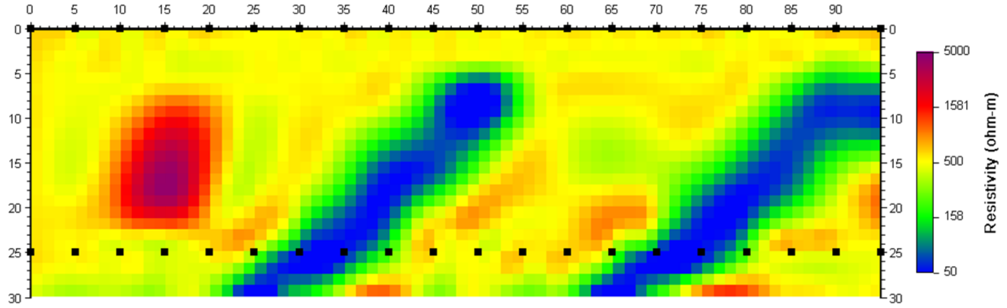

b) Optimized Protocol (2120)

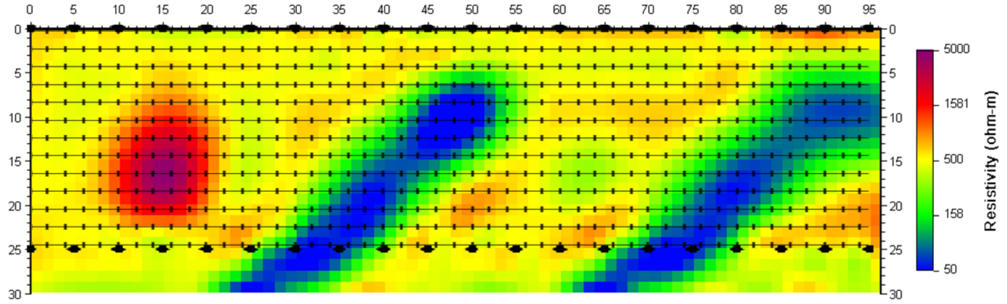

Figure 4.17: Inverted results of the a) Full and b) Optimized protocol.

Finally, an arrangement of electrodes in two boreholes with different degrees of inclination was examined (Figure 4.18). The boreholes at the left and right had an inclination equal to 80° and 110°, respectively (measured clockwise from the surface). Both are at 10m depth and over a horizontal distance of 60m measured from the shallower electrodes. Each has 20 electrodes with a spacing of 5m. The full protocol has 9408 measurements and the optimized 2346. After the inversion with the abovementioned properties, the full and optimized protocol results are the following (Figure 4.19 a-b).

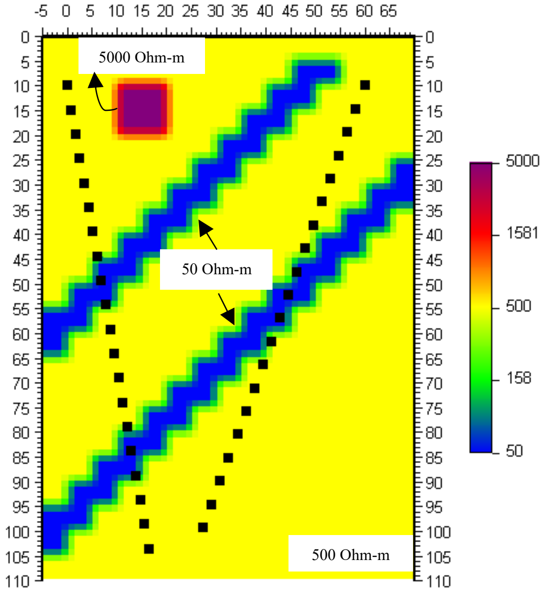

Figure 4.18: Synthetic model with half-space 500 Ohm-m, one resistive block (5000 Ohm-m) and two conductive lines (50 Ohm-m) resembling fault zones. The geometry used, was two boreholes of different inclination (80° left, 110° right).

For this arrangement, the area with good sensitivity is expected to be around the boreholes. In the first meters (<25m depth), due to the more considerable distance between the boreholes, the resistive block and the continuation of the fault appear blurry in both figures. The targets appear clearly in larger depths where the boreholes converge, and their horizontal distance reduces. The optimized protocol once again seems to have similar results to the full, with only some differences.

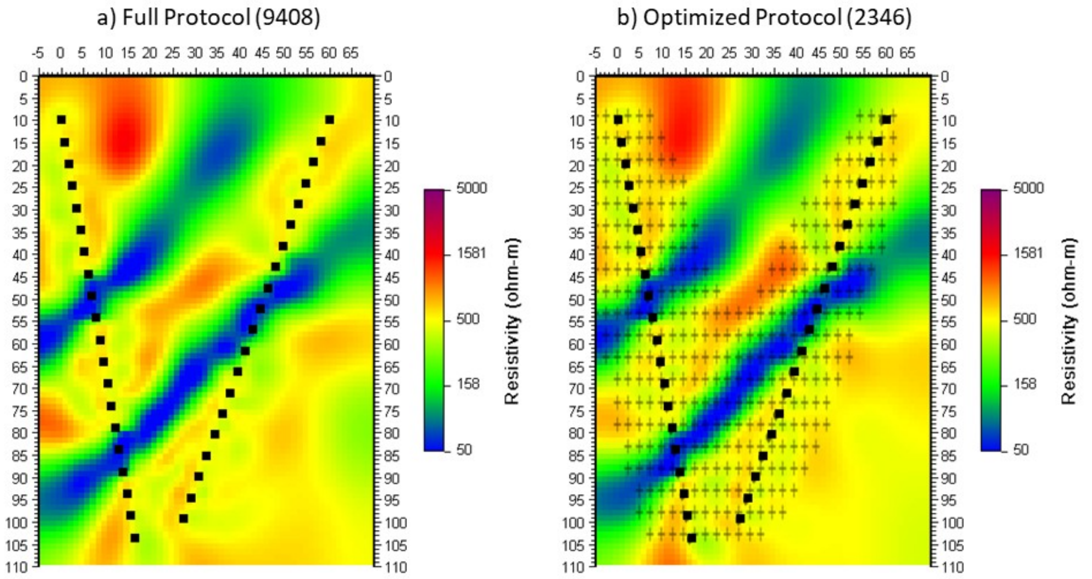

Figure 4.19: Inverted results of the a) Full and b) Optimized protocol.

If there were also surface electrodes, the entire area between the boreholes would probably be better depicted. This hypothesis was tested by adding 16 surface electrodes with a spacing 5m, and the results of the full (15100 measurements) and optimized dataset are shown in Figure 4.20 a-b. The full protocol combines three datasets, meaning the measurements between the two boreholes and the measurements

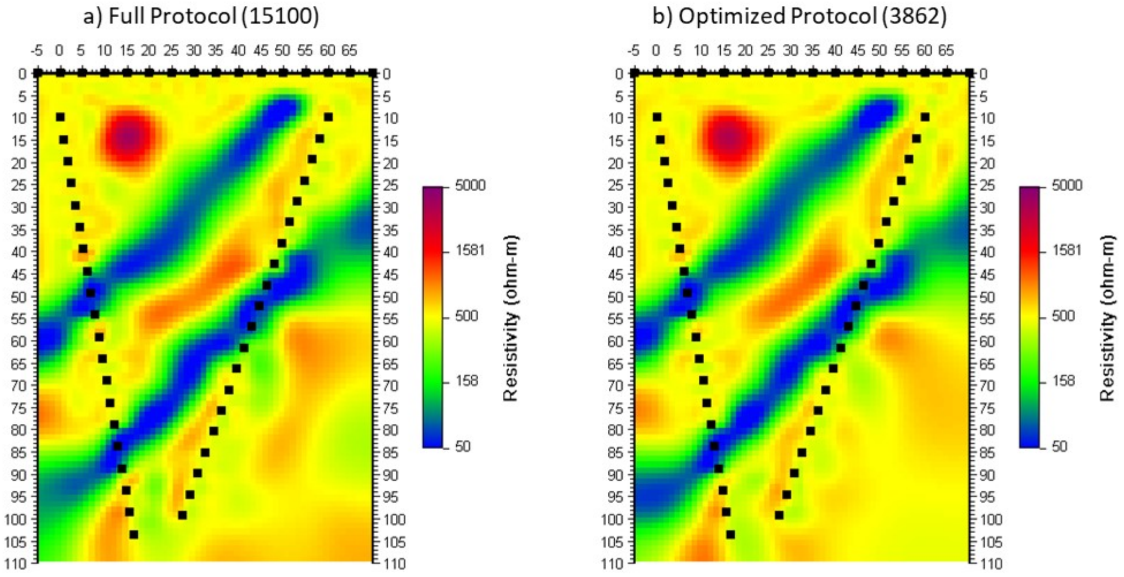

Figure 4.20: Inverted results of the a) Full and b) Optimized protocol with the added surface electrodes.

of the first borehole-surface and the second borehole-surface. That is the reason why there are so many measurements. These combined protocols were created individually and then merged, taking care not to include repeated measurements. It's obvious now that the block is precisely detected without distortion in its shape, and also, the upper fault zone is more finely formatted. The rest of the area has the same presentation since the surface electrodes can only increase the resolution until a specific depth. Again, the optimized dataset significantly resembles the imaging of the full protocol.

4.2 Laboratory experiments

In addition to the synthetic models, some experiments were conducted using a plastic tank with dimensions 125 cm x 80 cm x 90 cm (length x width x height) filled with tap water up to 60cm. The base for the surface and borehole electrodes was a plastic double "rail", cut in two pieces of approximately 1m (part of the structure is shown in Figure 4.21). These two pieces, after some modifications, were joined in their edge with a plastic screw so that they are on the same vertical plane and with the ability to form various angles.

Also, a part of the "borehole's" plastic was cut so that only one rail would remain to avoid its presence influencing the measurements. Plastic nodes were added to these rails and filled with silicone in their circular edge so the nails (electrodes) could pierce them and stay relatively stable. This structure was chosen since the double rail was stiff and would not curve and because the nodes could be moved at different distances but also stay firm in place when screwed.

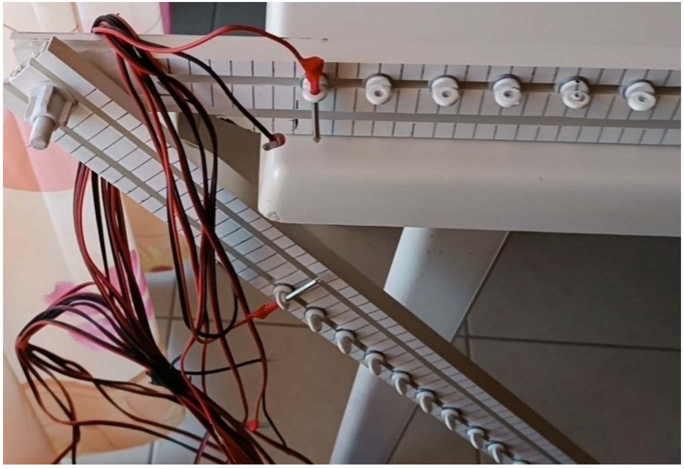

Figure 4.21: The structure for the surface and borehole's electrodes.

For these experiments, 2 multi-electrode cables with 24 exits were utilized. The electrodes were placed in the "borehole" and at the "surface", 12 each, spacing 3cm. Their position was approximately in the middle of the tank to avoid the influence of the surroundings. The borehole's inclination was 35° for all the measurements. The first borehole and surface electrodes were situated on the same horizontal distance (0m) with the former at ~14cm depth. The water's resistivity was calculated at approximately 30 Ohm-m. The conducted experiments had as targets 3 items: a resistive plastic water bottle (0.5L) full of sand to increase the weight, a conductive fragment of pyrite rock, and a conductive metallic block. These targets were sunk in the water, each fixed at different depths and distances.

For each target, a full and three optimized protocols with final measurements of approximately 25%, 50% and 75% of the measurements of the full protocol were created using a medium threshold value. Only the full protocol was measured in the lab, and the optimized protocols were extracted afterwards from the full protocol. The software used for the inverted results was the DC_2DPro. The x and z axes were multiplied by x100 to convert the meters (0.03m) into centimeters (3cm). This did not affect the geometric factor since the modification occurred after its calculation. This scaled depiction was applied because the software did not respond well to decimal values. So, all the results will be presented in a scaled manner.

Before the experiments with the targets, some measurements were acquired in the homogenous environment with just the water to confirm its resistivity. The inverted results of the full protocol, composed of 2428 measurements, are shown in Figure 4.22. It seems that most of the space in between the borehole and the surface electrodes has a resistivity of ~30 Ohm-m. However, some regions have lower and higher resistivity values, especially on the right and at the bottom left of the figure. These changes were anticipated since these areas are probably out of the trusted area. Still, some distortions that appear near the electrodes may be due to the dispositions of the nails, which were not precisely perpendicular.

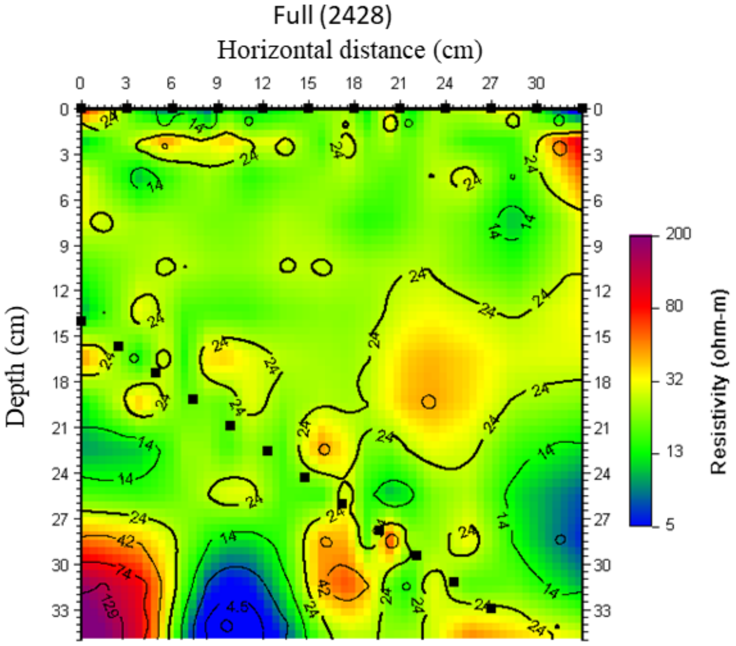

Figure 4.22: Inverted results of the full protocol of a homogenous environment (water).

For the next experiment, the water bottle of dimensions 20cm x 6cm (height x diameter) was placed horizontally over the bottom of the tank and vertically to the construction. Its centre was 15cm from the first surface electrode, and its top was 8cm from the water’s surface (Figure 4.23). The inverted results of the full and three optimized protocols (25%, 50%, 75%) with the medium threshold will be presented (Figure 4.24 a-d). In the full protocol (Figure 4.24 a), there is a distinct increase in the resistivity in the middle of the tomography. This is where the bottle was inserted, meaning this protocol managed to detect it. It appears with resistivity >50 Ohm-m, in contrast to the environment with resistivity around or less than 30 Ohm-m. Once again, some artefacts are present on the right, at the bottom of the tomography, and in the middle with similar positions as in the previous example, i.e., at a depth of 3m and in horizontal distances 6-9m and 21-24m.

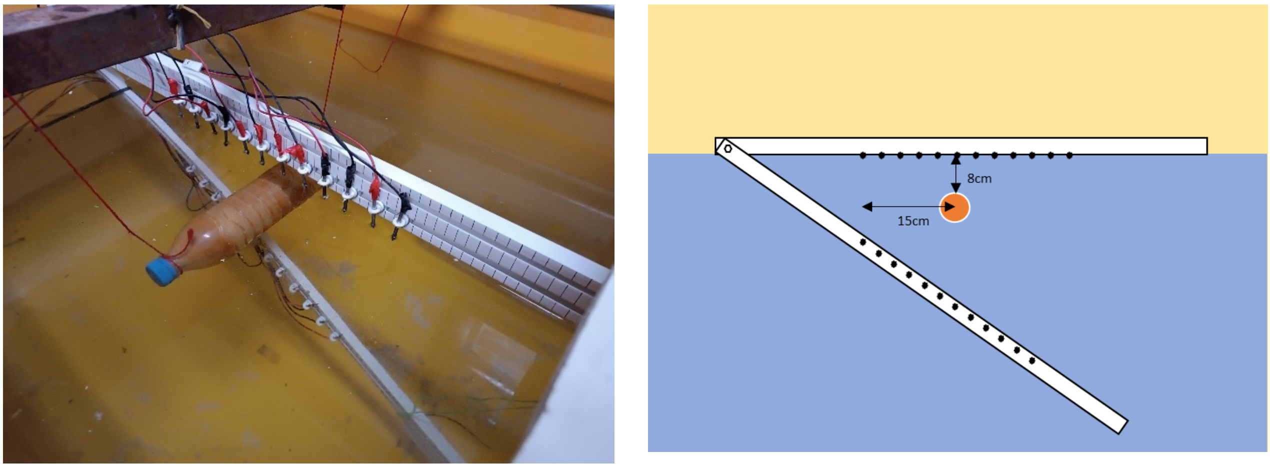

Figure 4.23: The experiment’s setup, with the bottle as a resistive target (on the left). A 2D illustration of the experiment (on the right).

The optimized dataset of 25% (Figure 4.24 b) fails to discriminate the target accurately. The chosen measurements are not enough to depict the target. There seems to be a region of higher resistivity where the bottle was inserted, but an artefact is also associated with it, creating a disturbed shape. The optimized dataset of 50% (Figure 4.24 c) manages to detect the bottle and has a better representation than the data of 25%. The best protocol is the one that uses 75% of the measurements (Figure 4.24 d) with 1706 measurements, where the target is in the correct position at approximately 6cm depth. Again, the contrast between the bottle and the environment is clear, and the figures' artefacts are less intense. As the medium threshold indicates, the trusted area includes the target and excludes the artefacts.

The following experiment had a portion of pyrite (Figure 4.25) of irregular dimensions as a target. Its dimensions were approximately 10 x 9cm (width x height). The rock’s centre was located at a distance of 11cm and at a depth of 8cm from the water’s surface to its top. The inverted results of the full and three optimized protocols (25%, 50%, 75%) with the medium threshold will be presented (Figure 4.26 a-d). The full protocol has 2428 final measurements and seems to detect a target of low resistivity starting at 6cm depth, although the rock was expected at 8cm depth. The shape of the rock, as the low resistivity area outlines it, appears more distorted than anticipated. Once again, some artefacts on the right of the figure out of the high-resolution areas.

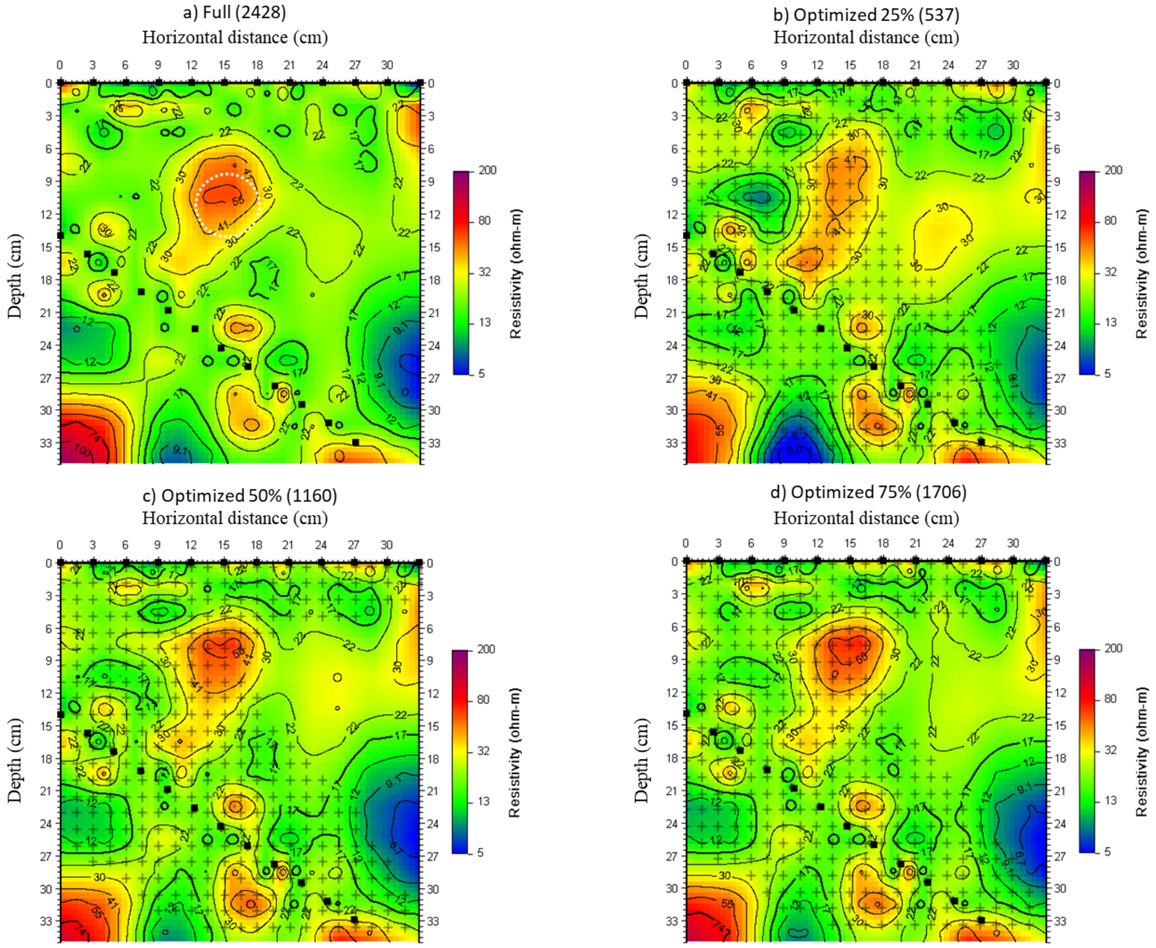
a) Full (2428)

b) Optimized 25% (537)

c) Optimized 50% (1160)

d) Optimized 75% (1706)

Figure 4.24: The inverted results of the a) full and optimized datasets of b) 25%, c) 50% and d) 75%, with the bottle as a target. On the brackets appear the total measurements of each dataset. The dotted circle on the full protocol represents the target.

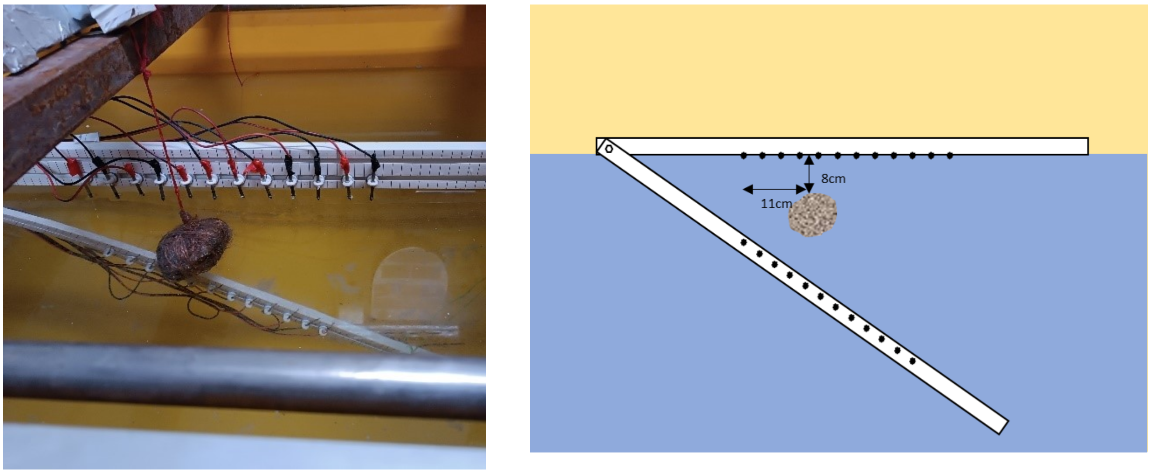

Figure 4.25: The experiment's setup, with the pyrite rock as a conductive target (on the left). A 2D illustration of the experiment (on the right).

The optimized dataset of 25% has a different appearance from the target. Due to the lower number of measurements, the image is not that detailed, and that's probably why the target appears with greater dimensions. The optimized datasets of 50% and 75% resemble the image of the full protocol, with artefacts in similar positions.

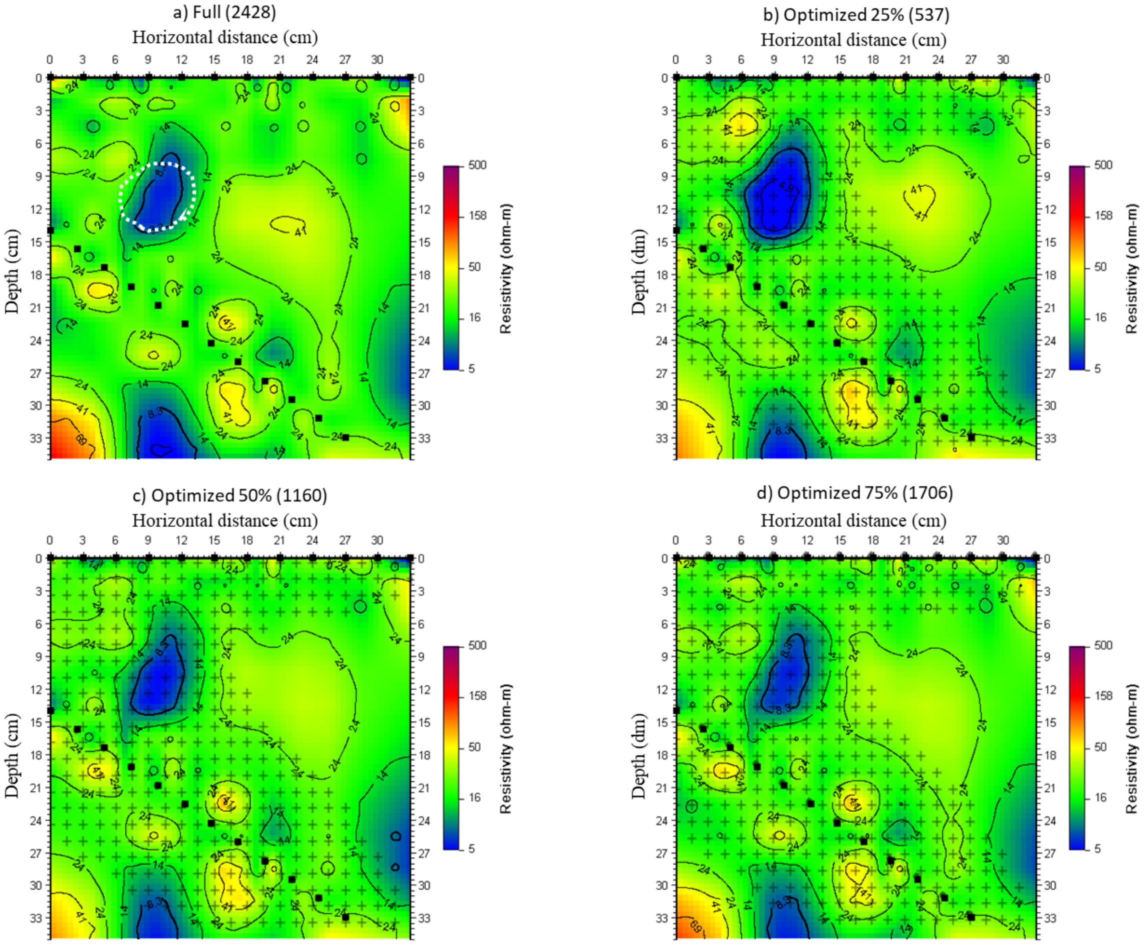

Figure 4.26: The inverted results of the a) full and optimized datasets of b) 25%, c) 50% and d) 75%, with a metallic block as a target. On the brackets appear the total measurements of each dataset. The dotted line on the full protocol represents the target.

Finally, the last target was a conductive circular metallic block with a hole in its centre. Its top edge was situated at 8cm depth from the water's surface and at 15cm horizontal distance, with a random inclination since fixing it at a particular angle was difficult (Figure 4.27). The inverted results of the full and three optimized protocols (25%, 50%, 75%) with the medium threshold will be presented (Figure 4.28). The measurements can identify this block as a conductive target in the full inverted results. Some artefacts are present below the borehole and on the right of the figure, which was expected based on the previous experiments.

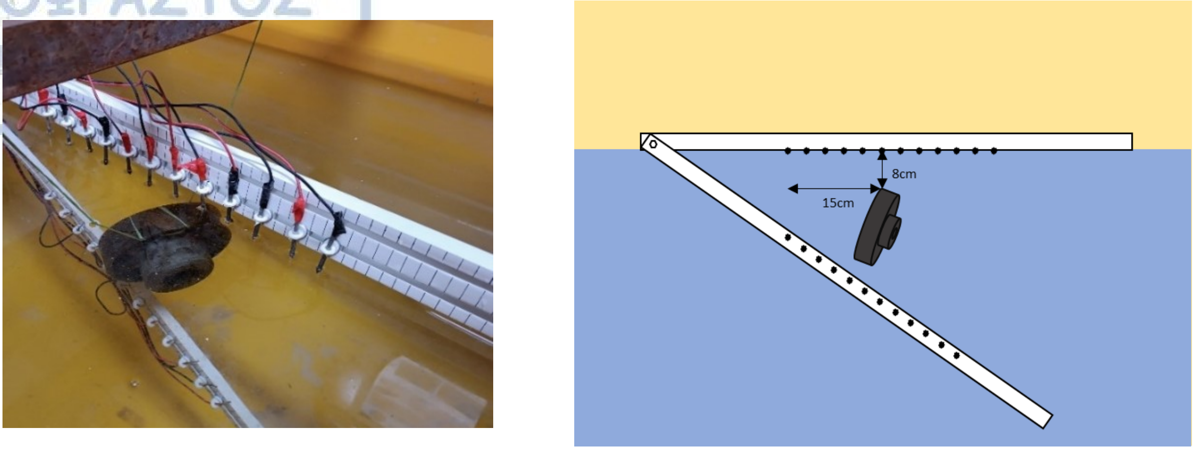

Figure 4.27: The experiment's setup, with a metallic block as a conductive target (on the left). A 2D illustration of the experiment (on the right).

The optimized protocol of 25% this time gives results closer to the full protocol than the previous models. The optimized 50% and 75% results significantly approach the imaging of the full protocol and locate the target more clearly. It is worth mentioning that in all the models, a target of high resistivity value appears near the conductive target at 21-24cm horizontal distance and in 9-12cm depth, which is considered an artefact out of the trusted area of this model.

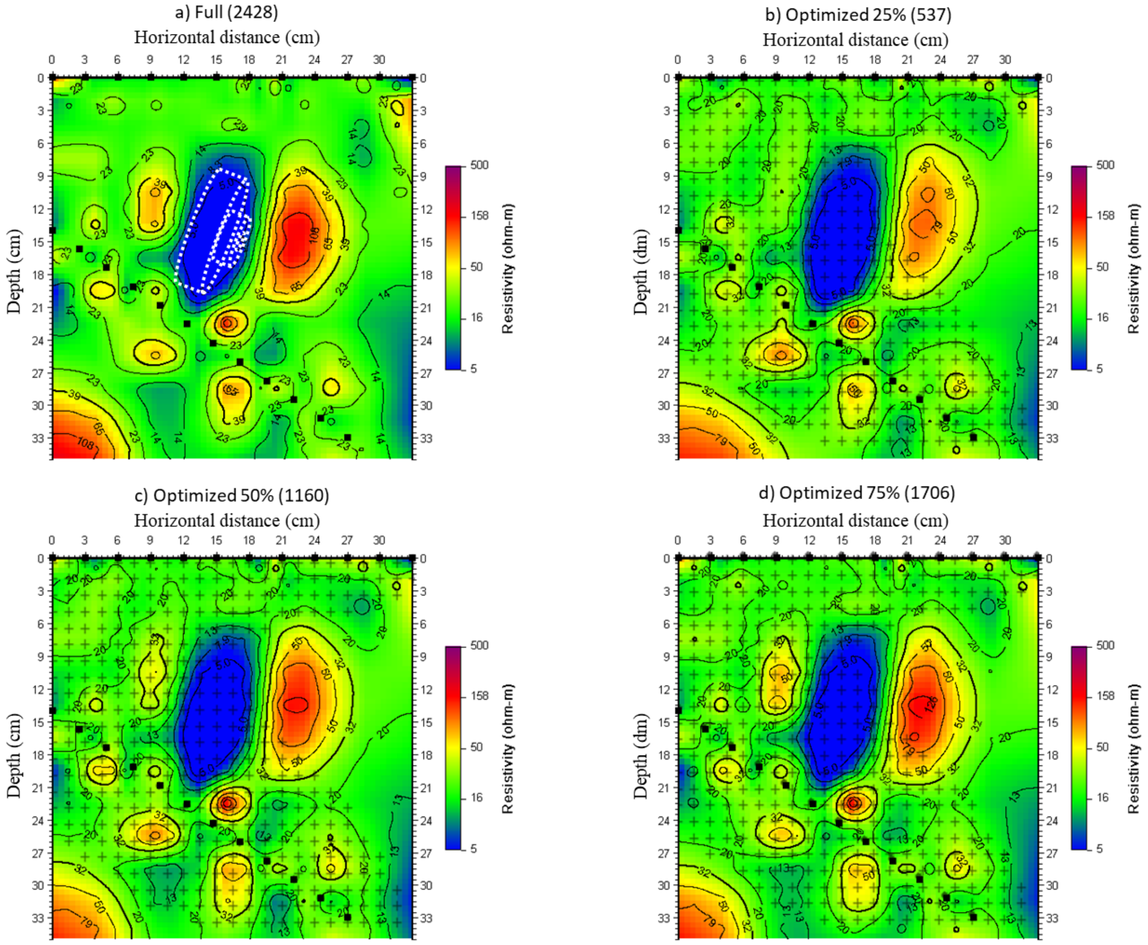

Figure 4.28: The inverted results of the a) full and optimized datasets of b) 25%, c) 50% and d) 75%, with a metallic block as a target. On the brackets appear the total measurements of each dataset. The dotted line on the full protocol represents the target.

4.3 Concluding remarks

According to both the synthetic and the experimental models that were presented, the following conclusions could be drawn:

- The algorithm can deal with various geometries and produce the full protocol and three optimized datasets.
- As the percentage of the measurements participating in the optimized protocols increases, the final inverted results are improved and closer to the reconstruction produced by the full protocol.
- The optimized datasets of 50% and 75% do not differ drastically, and the percentage of 50% is generally considered capable of reconstructing the tested models. Also, this protocol would require fewer resources when used in the field. The optimized dataset of 25% struggled to reconstruct the targets in some cases; however, for some models (mostly resistive), it worked pretty well and could approach the imaging of the full protocol.
- The different threshold values have no significant influence on the inversion process, as in some models, the targets were reconstructed even though they were outside the considered trusted area. Still, it seems a valuable tool in determining which of the examined trusted areas are more appropriate for each geometry.

So, it can be assumed that both the threshold and the optimized datasets depend on the geometry of the borehole-surface or borehole-borehole configuration and the chosen cartesian grid. So far, an optimum value for the measurement threshold or the most appropriate optimized dataset cannot be suggested due to the abundance of the different geometries that can be encountered. This problem can be partially solved by creating synthetic models for the desired geometry, with different values of the above parameters, to monitor their behaviour and recommend a trusted area and the most appropriate optimized protocol.

5. FIELD MEASUREMENTS

Besides applying the algorithm to synthetic and experimental models, the opportunity for its implementation in field measurements was given. This was achieved as part of a project carried out in the monument of the Rotunda church in Thessaloniki (Figure 5.1). Several boreholes were drilled into the monument's walls for maintenance purposes, marked with purple circles in the figure. This enabled the possibility to further investigate the interior of the wall's status in terms of moisture content, which threatens its preservation. Since the main purpose of this thesis is not to determine the wall's condition but to test the protocols generated by the algorithm and its utility in surveys with inclined boreholes further, only the results of two boreholes will be presented and discussed in this chapter.

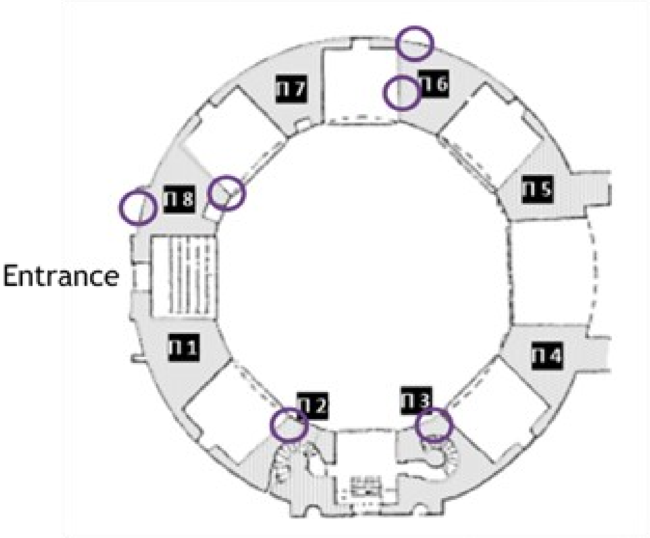

Figure 5.1: Top view of the monument of Rotund church in Thessaloniki. The purple circles indicate the walls that the measurements occurred.

5.1 Results

The walls were used as the reference plane, where the surface-borehole measurements were accomplished. The surface electrodes were placed on the wall, and the investigated area was a vertical or horizontal slice through the wall. Some boreholes were drilled approximately vertically to the walls, and others with another inclination. All the drilled boreholes had a diameter of 30cm and a length of 3m. Small nails with a mixture of wet bentonite for enhanced contact were employed as surface electrodes. The number of electrodes varied according to the capability of inserting them. The borehole electrodes were placed in a 3m PVC pipe construction (Figure 5.2). The plastic pipe was cut per 15cm (first electrode at 15cm), and the 18 cable's exits were attached to it, using aluminium foil tape with conductive adhesive to ensure the coupling of the electrodes with the wall's interior. Conduct was further enhanced with the injection of small quantities of water around the borehole during the measurement.

Figure 5.2: The PVC pipe construction that was used for the support of the borehole electrodes.

Only some of the tomographies will be presented to evaluate the applicability of the generated algorithm. In all tomographies, the designated electrode IDs start from the borehole electrodes, where the deepest into the wall is the number 1. So, electrodes with ID 1-18 correspond to borehole electrodes, with the 18th closer to the tip of the borehole. The surface electrode IDs start from 25 since the instrument had two 24-channel exits. Also, the numeration of the surface electrodes is initiated from the external electrode closer to the borehole's tip, and the inclination of the borehole is measured clockwise from the appointed zero-point marker. Lastly, the inverted results are scaled; since the DC_2DPro did not respond well to decimal points, the measured distances (m) were converted to decimeters (dm).

One of the tomographies occurred in the interior of the Rotunda church. A picture of the field measurements is presented (Figure 5.3), where the dashed yellow line indicates the horizontal line where the measurements took place. The position of the surface electrodes is pointed with red circles, and the arrow points to the borehole's tip. The investigated area is a slice through the wall parallel to the ground (Figure 5.4). The number of installed electrodes was 36, with 18 surface electrodes at the wall spaced 30cm apart, and 18 in the borehole spaced every 15cm. Two of them were skipped because the one at the surface could not be placed in the correct position due to a cavity in the wall, and the one in the borehole exhibited high contact resistance values. For this ERT section, the corner of the wall near the borehole was considered the origin. The borehole was situated at a horizontal distance 1.05m from the corner and formed an angle of 48° with the surface electrodes. The «shallowest» borehole electrode (18th) was at 12cm vertical distance from the «surface».

Except for the full protocol, the optimized datasets of 25%, 50% and 75% for three thresholds (low, medium and high) will be presented to test the algorithm's effectiveness in real data. The original full protocol with all available configurations comprised 8513 measurements, including gap fillers. The total final number of the protocol after skipping 2 electrodes, rejecting gap-fillers and exterminating bad data was 6047. The inverted results of the full protocol had an RMS error of 7.2% and are presented in Figure 5.5.

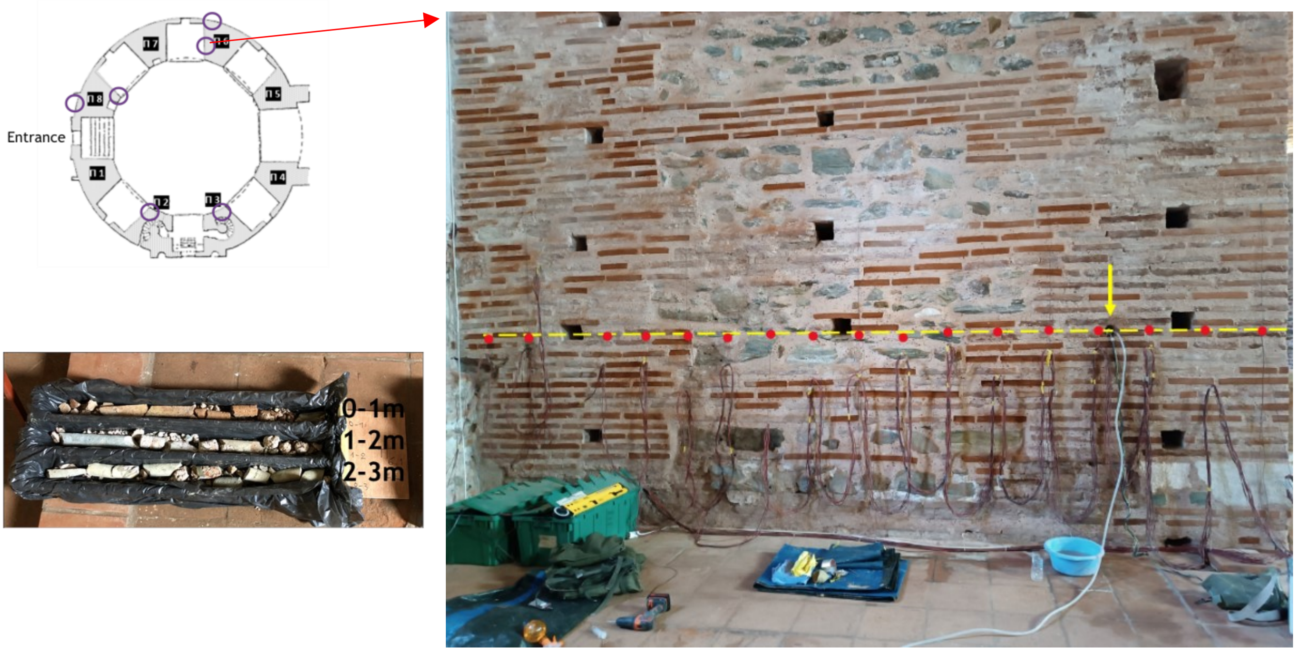

Figure 5.3: Photograph of the investigated wall (on the right). The dashed yellow line indicates the reference plane where the surface electrodes (red dots) are situated. The arrow points to the tip of the borehole. On the top left corner there is the top view of the monument and on the bottom corner a picture of the borehole's core.

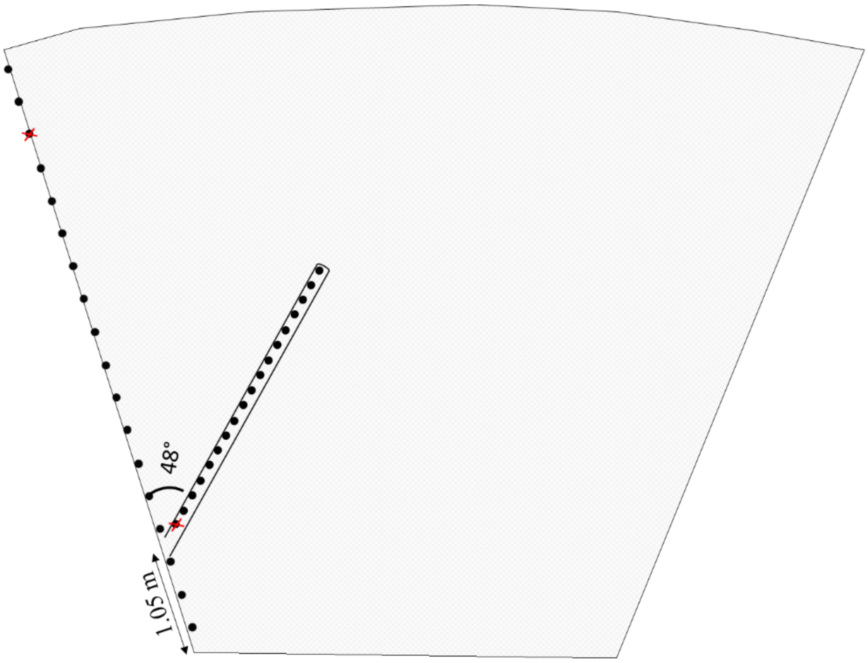

Figure 5.4: Top view of the investigated area. The surface and borehole electrodes are noted with black circles and the boreholes inclination is 48°. Two electrodes were skipped and are indicated with red cross.

According to the inverted results of the full protocol, a zone with relatively low resistivity values around 50-100 Ohm-m appears near the borehole. Locally, there are areas with even lower resistivities, 10-30 Ohm-m, which could indicate that the material in this area is disturbed and possibly more prone to contain moisture. The core log of the borehole shows the existence of mixed material of masonry bricks and mortar for the first 1m, while the deeper parts (1-3m) comprise of greenschist blocks. A more resistive block appears at around 9-12dm and at depth 7dm with resistivity values around 250 Ohm-m, which could be more compact. In greater depth (18-21dm) and around 10-18dm horizontal distance, appears a body of high resistivity ~1000 Ohm-m, which could be a solid block or a generated artefact since it is a bit distant from the borehole and the surface electrodes.

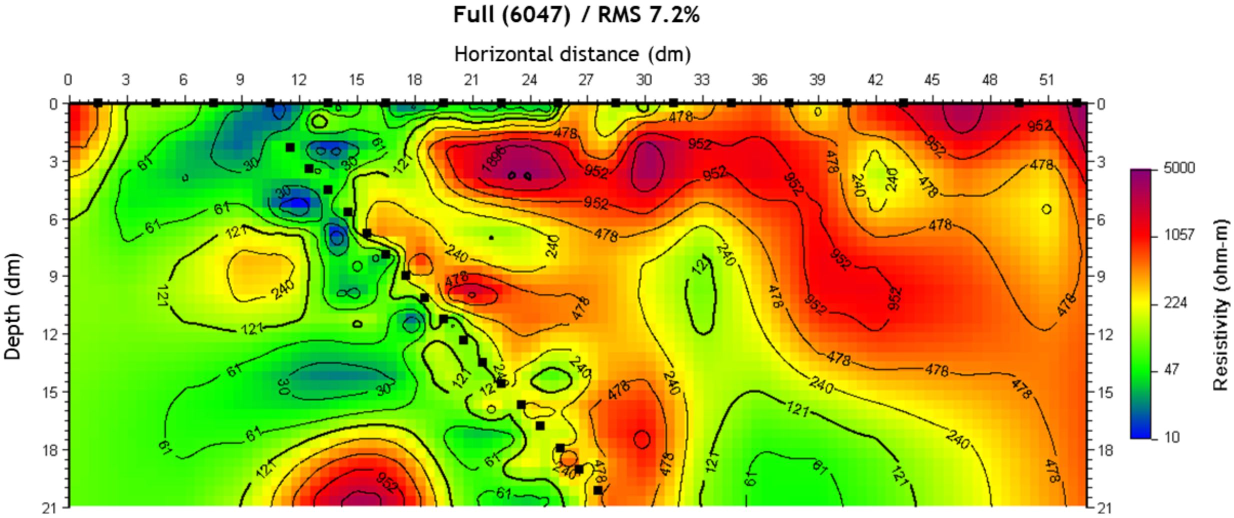

Figure 5.5: Inverted results of the full protocol.

On the right of the borehole is a very resistive material (>1000 Ohm-m), which probably corresponds to undisturbed and solid rock. These are probably blocks of green schist that are also apparent at the exterior of the wall in the middle of the photograph (Figure 5.3), where there is a discrepancy between the construction blocks that could justify these higher resistivity values. This material seems to continue in greater depth.

To define the trusted area of the model, a synthetic model was compiled (Figure 5.6) for the exact measurements and similar targets for this particular geometry. The forward model was calculated for the full and the three optimized protocols with the different threshold values. Since this synthetic model was meant to be realistic, the findings can be used to assess the actual data results.

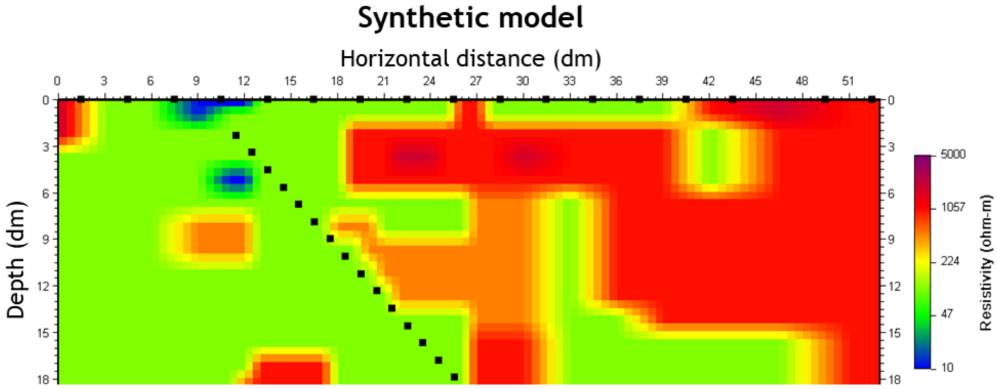

Figure 5.6: Synthetic model that resembles the target of the full protocol.

The inverted results of the full protocol are shown in Figure 5.7. According to these results, the full protocol can accurately represent the synthetic model, except for the lower right corner, where the resistive target cannot be detected. Thus, this region is outside of the trusted area. Interestingly, the resistive target between 11-18dm horizontal distance and >15dm depth, suspected to be an artefact, appears in the inverted image of the full protocol. Therefore, it is inside the trusted area of this geometry.

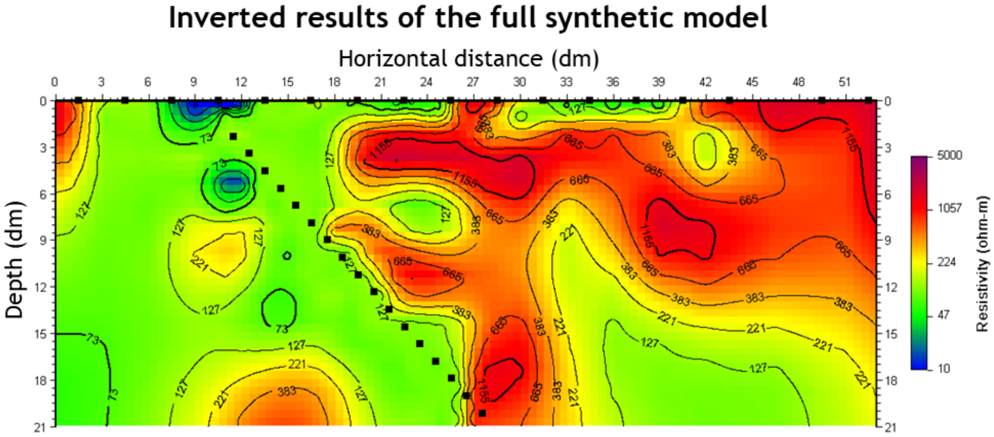

Figure 5.7: Inverted results of the full synthetic model.

According to the inverted results of the synthetic optimized datasets (Figure 5.8), it is evident that the one that approaches the initial synthetic model with utmost accuracy is the 75% optimized data set with the medium threshold. No artefacts appear, and the targets are in the correct position. All other models recreate the space between the borehole and the surface electrodes well but exhibit artefacts. It could be inferred that although the optimized protocol with the medium threshold provides the best-inverted results, the trusted area should be less strict because the resistive area on the bottom left is detected by all the models, meaning it's a valid target. So, for this specific geometry, it could be suggested that the low threshold indicates the trusted area.

After this process and having estimated the most appropriate optimized protocol and threshold using the synthetic models, the actual optimized protocols can now be evaluated for the real data. The inverted results of the optimized protocols appear in Figure 5.9. On top of each figure, the number of the final measurements and the RMS error are noted. It is worth mentioning that the algorithm did provide the optimized protocols with measurements at around 25%, 50% and 75% of the full protocol, but due to the processes followed (i.e. skipped electrodes, bad data) and the fact that the protocols were created before the actual measurement, the final number of the remaining measurements is way decreased. In each of these models, the area of expected sensitivity was noted.

Synthetic models

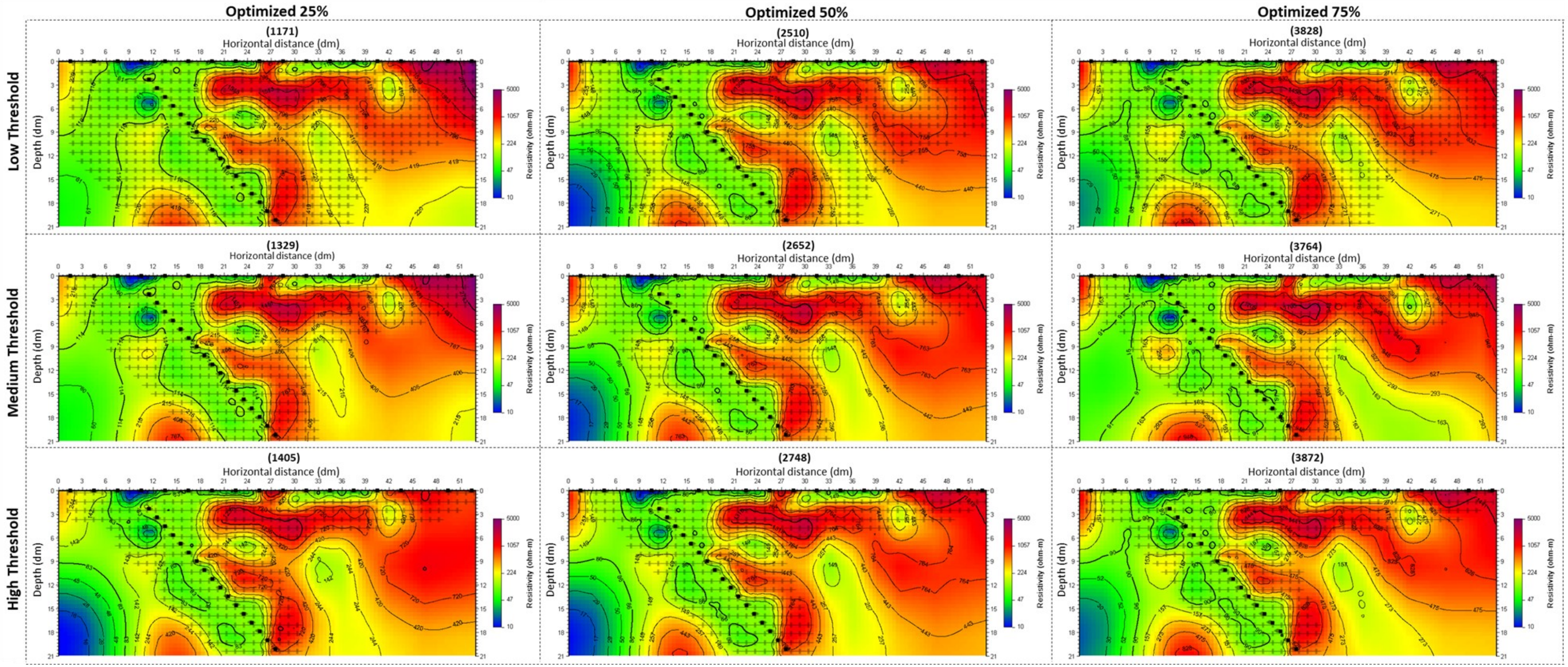

Figure 5.8: Inverted results of the synthetic optimized protocols with final measurements of approximately 25%, 50% and 75% of the full protocol with three different thresholds (low, medium, high). The crosses on the optimized models represent the trusted area that corresponds to each threshold value.

Real data

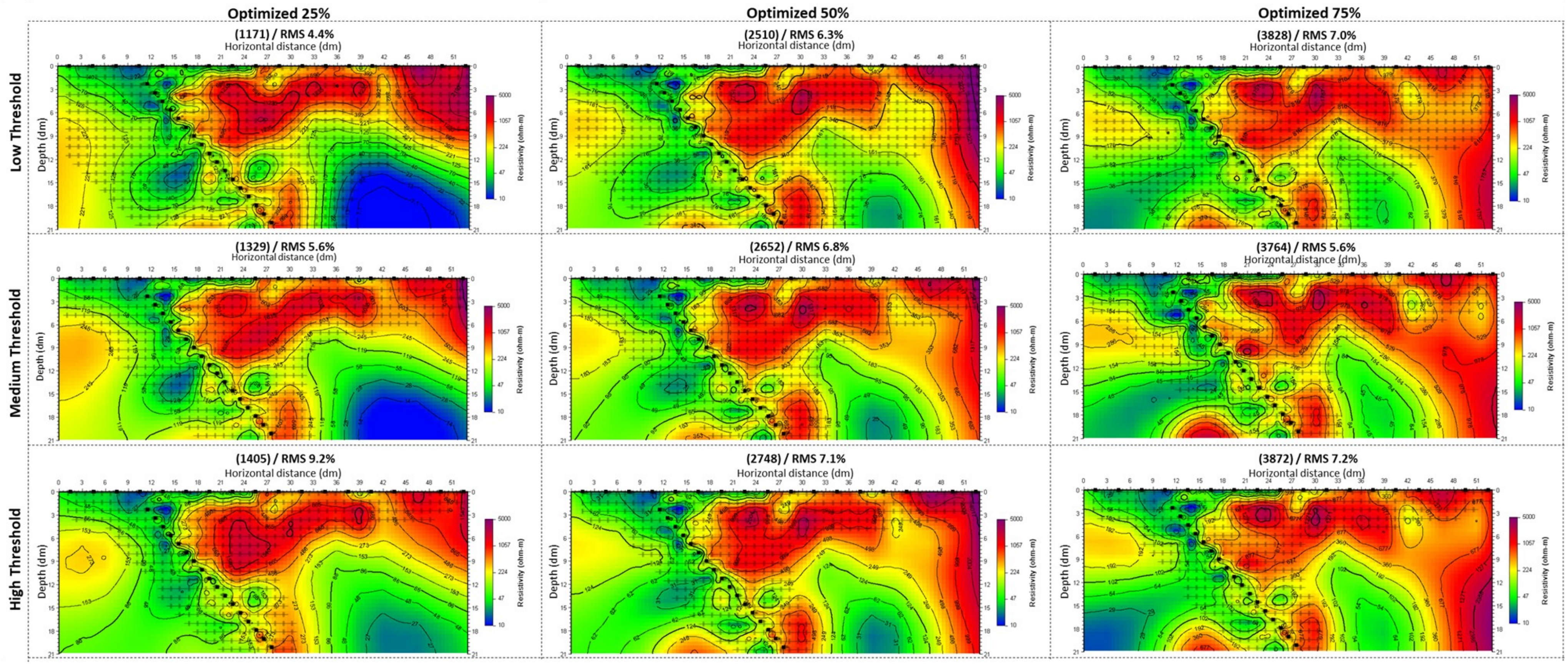

Figure 5.9: Inverted results of the real data of the optimized protocols with final measurements of approximately 25%, 50% and 75% of the full protocol with three different thresholds (low, medium, high). The crosses on the optimized models represent the trusted area that corresponds to each threshold value.

The inverted results of the 75% optimized data significantly resemble the full protocol's inversion, especially the one with the medium threshold. On the left of the borehole is the region with low resistivities, whereas on the right is compact material with high resistivities. The boundaries of the formations are blurrier compared to the full protocol.

The inverted results of the 50% optimized data differ slightly from the results of the full protocol, especially in the area of the resistive target to the right. Despite that, these models give a reasonable area reconstruction and detect the low resistivity zone. In the inverted results of the 25% optimized dataset, the image is fairly distorted, especially on the right corner, where at depth ~12 dm, a very conductive artefact is depicted, which is not present in other models. To be fair to these two cases of optimized datasets, it should be pointed out that the resulting number of measurements is way lower than even half of the full protocol, so no good resolution should be expected.

The same borehole was used for another measurement where the surface electrodes were placed on another side of the same column (Figure 5.10). For the surface electrodes, only ten could be placed per 30cm. All the borehole electrodes participated in the measurements this time, including the one dismissed in the first tomography. The first surface electrode was at a 12cm distance from the corner, which was closer to the borehole. The borehole was calculated to form a 57° (clockwise) angle with the new electrode line. Since the reference point of the axes was chosen to be the corner of the column and the two sides of the wall form an obtuse angle, the first borehole electrode had a negative «x» coordinate. The top view of the measurement is also available (Figure 5.11).

Figure 5.10: Photograph of the investigated wall (on the right). The dotted yellow line indicates the line of the surface electrodes (red dots). The arrow points to the tip of the borehole. On the top left corner there is the top view of the monument.

The original full protocol had 3613 measurements, including gap-fillers. The final protocol after all the processes had a total of 3040 measurements. The inverted results with an RMS error of ~10.8% are presented in Figure 5.12. This time, the low resistivity zone is on the right of the borehole, the same area discussed above. Except for that, there are regions of low resistivity near the surface electrodes, especially in distances 0-3dm with depth ~2-9dm but also at 12-27dm horizontal distance and depth around 6dm, that are prone to contain moisture.

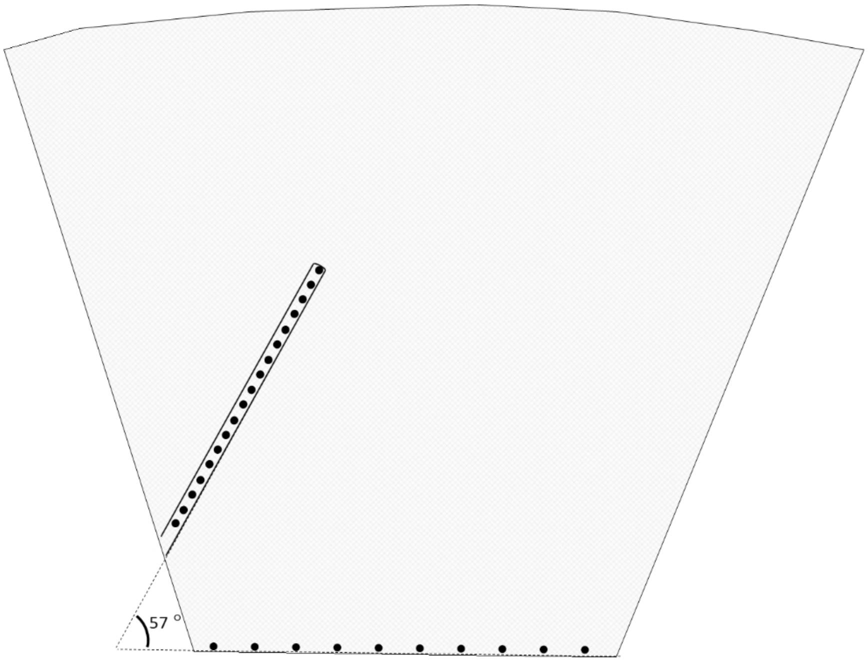

Figure 5.11: Top view of the second measurement that occurred with the same borehole at another side of the investigated column. The surface and borehole electrodes are indicated with black circles and the borehole created an angle of 57° with the surface electrodes.

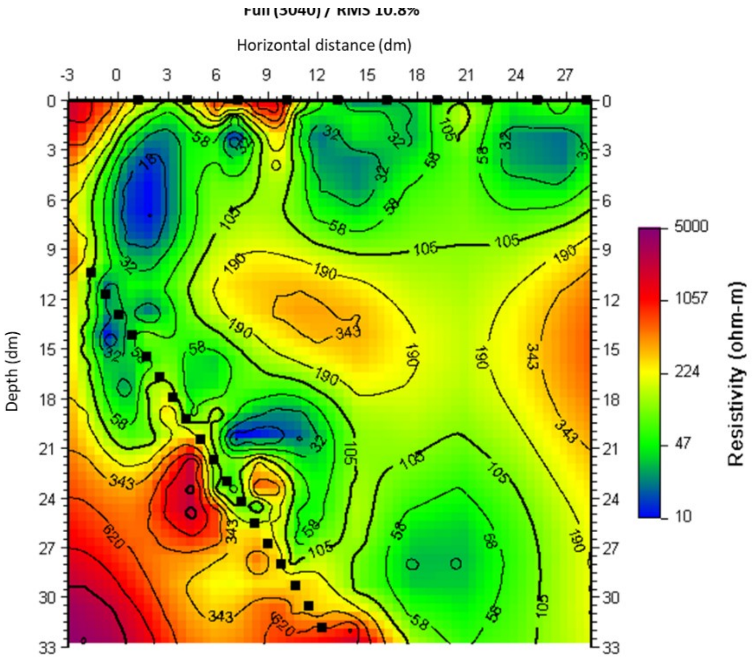

Figure 5.12: Inverted results of the full protocol.

It is also apparent that in the middle of the figure, there is a block with resistivity >170 Ohm-m that possibly corresponds to undisturbed or drier material. On the top left of the figure is an area of high resistivity. This is where the wall ends, so this region is filled with air, which explains the high resistivity. On the bottom left of the borehole, at around 21-27dm depth and 2-7dm horizontal distance, an area of high resistivity is present and probably corresponds to compact material observed in the first tomography. The deeper block at the corner, with even higher resistivity, could probably be an artefact since it is removed from the borehole and was not observed in the first tomography.

The inverted results of the optimized protocol of 75% with the medium threshold and RMS error of ~11% are shown in Figure 5.13. The total measurements were 2401, but after some rejections, only 2293 participated in the inversion process. The imaging of the optimized protocol is similar to that of the full model. A significant part of this tomography seems to be subjected to moisture with low resistivities. It is worth mentioning that the optimized model provides more artefacts, especially on the bottom right and left corner.

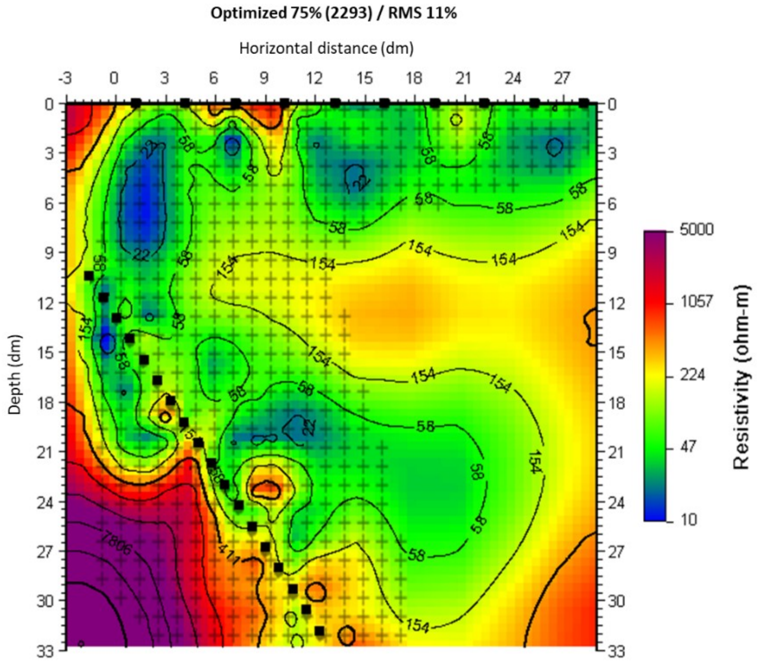

Figure 5.13: Inverted results of the optimized protocol of 75%.

This second tomography enlightened areas that the first one could not evaluate and improved the conclusions of a significant part of this column. To better depict the investigated column (top view Figure 5.14), we combined these two datasets and inverted them all together. The inverted results of this combined full protocol with 8843 final measurements are shown in Figure 5.15. A new coordinate system was created, where the second wall's surface electrodes were vertical, and the surface electrodes of the first wall were imported as topography. Two more electrodes (with red X in the figure) were added to help the grid's appearance but were not included in the inversion process. The area of negative «x» coordinates with high resistivity values (lila colour) was added as apriori information since it is outside of the wall's boundaries and consists of air. The trusted area results from the combination of the trusted area of the two individual tomographies, and its boundaries are indicated with a white dashed line.

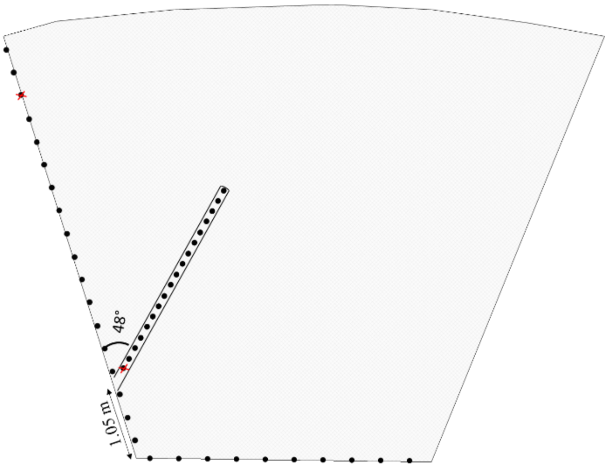

Figure 5.14: Top view of the combined tomographies.

According to these results, it is apparent that the area that probably contains the higher degree of moisture is near the second wall (vertical electrodes in the figure) until at around 60dm horizontal distance through the wall. The zone of low resistivities around the borehole comprises of material prone to contain moisture. Still, it may also be affected due to the insertion of a small quantity of water during the measurements. The other regions with high resistivity values correspond to the appearance of greenschist.

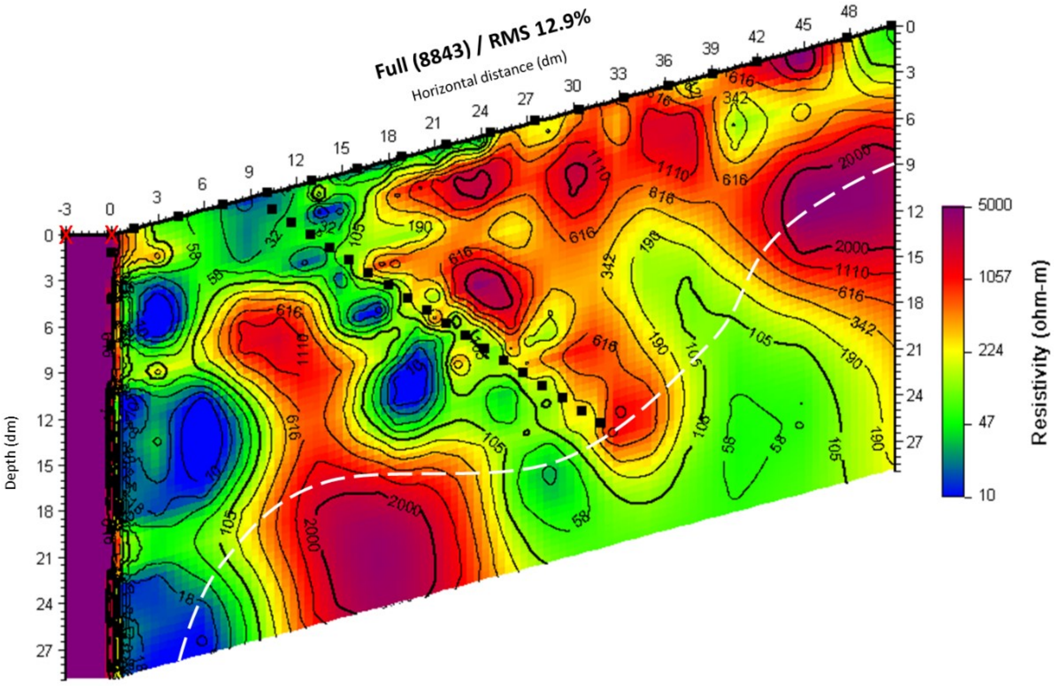

Figure 5.15 Inverted results of the combined protocol. The electrodes with the red X were added to improve the appearance of the results and were not included in the inversion process. The area on the left (purple color) was imported as a priori information with high resistivity because the end of the wall is at the vertical electrodes. The dashed white line outlines the trusted area.

Except for these two tomographies, another was contacted in a different monument column (Figure 5.16) with the surface electrodes vertical to the ground. So, the investigated area is a slice through the wall and perpendicular to the floor (Figure 5.17). This time, the borehole was almost vertical to the surface electrodes with an inclination of 92°. Again, 18 borehole electrodes were equipped with a spacing of 15cm. There were only 8 surface electrodes for this tomography since no more could be added to the wall. Their spacing was again 30cm. The borehole's tip was at a horizontal distance (in reality, vertical) of 1.25m from the bottom electrode.

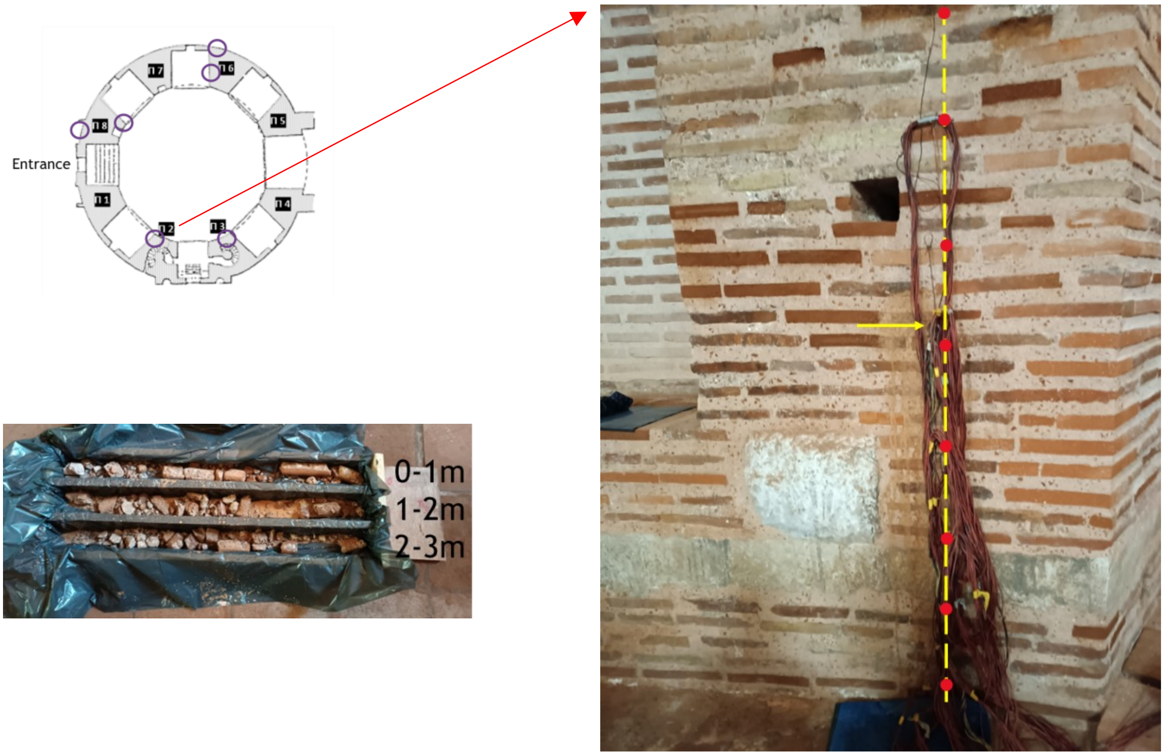

Figure 5.16: Photograph of the investigated wall (on the right). The dotted yellow line indicates the line of the surface electrodes (red dots). The arrow points to the tip of the borehole. On the top left corner there is the top view of the monument and on the bottom corner a picture of the borehole's core.

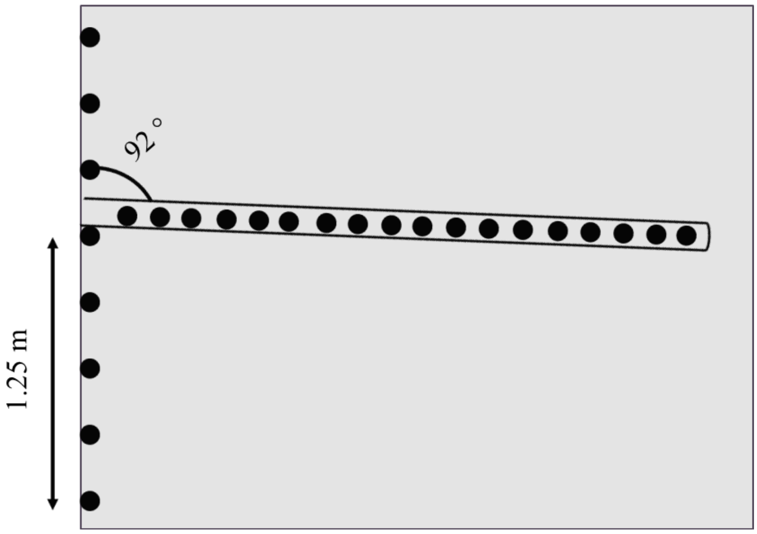

Figure 5.17: Schematic presentation of the investigated area. The surface and borehole electrodes are indicated with black circles and the borehole is almost vertical to the surface electrodes with inclination 92°.

The original protocol uploaded to the instrument consisted of a total of 2816 measurements, including gap fillers. All the placed electrodes participated in the investigation, and after the processing of the data, the final number of measurements was 2086. The inverted results of the full protocol with an RMS error of ~10.8% are shown in Figure 5.18. According to this, there is a region of relatively low resistivity values around the borehole at a horizontal distance of 6dm-21dm and until 6dm depth, where the area is more prone to containing high moisture. The resistivities are even lower at the beginning of the borehole in the first four electrodes. They may be influenced by the insertion of small quantities of water during the measurements.

Also, there is a resistive target between 3dm-6dm horizontal distance with visibly higher resistivity, caused by a marble block of the wall that also appears externally (Figure 5.16). Its continuation is apparent until at least 12dm depth. Below this target is a region with low resistivities that probably corresponds to an artefact since low resolution is expected at this part of the model. Finally, the interesting aspect is that around the borehole, at depths higher than 12dm, more resistive material appears, with resistivities greater than 500 Ohm-m. However, according to the core of the borehole (Figure 5.16) there is no change in the material, which leads to the conclusion that the material is more resistive because it is drier than the shallower regions. Furthermore, very close to the borehole, the resistivity values drop since the material was affected due to the drill and the water injected to the borehole.

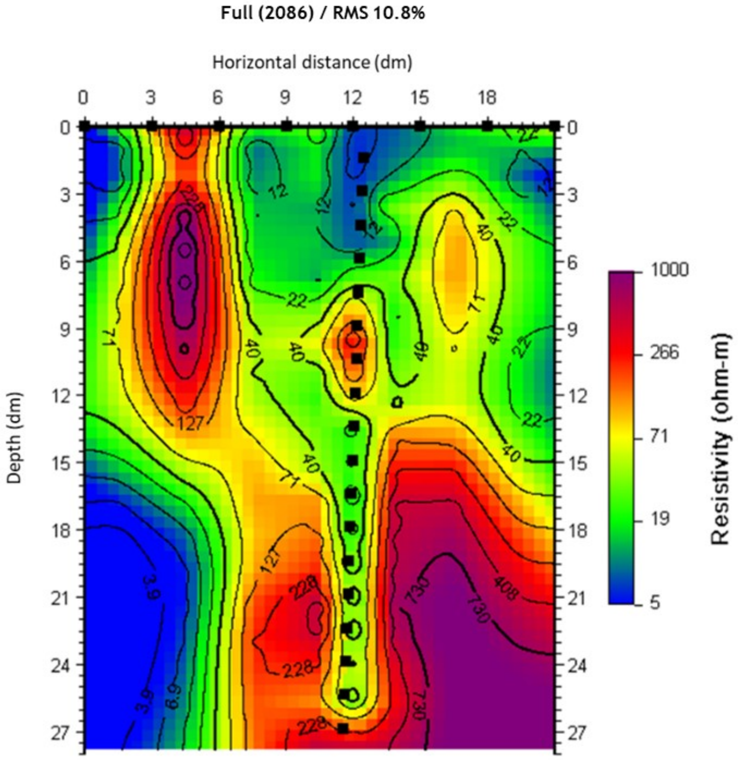

Figure 5.18: Inverted results of the full protocol.

Except for the full protocol, some optimized ones were again examined. Three optimized protocols were created with 25%, 50%, and 75% of the original full protocol measurements (2561 without the gap fillers). The trusted area of the models is depicted by a threshold deemed appropriate. The inverted results of each protocol are shown in Figure 5.19. The optimized protocol of 25% with 441 measurements and RMS error of ~5.8% shows an inversion image similar to the one created by the full protocol in the trusted area. Some discrepancies, i.e., the resistive artefact, appear on the left (6dm-12dm depth), but generally, the results are satisfying. As for the optimized protocol of 50% (1081 measurements, RMS error ~9,5%) and 75% (1977 measurements, RMS error ~10.2%) they generate an inversion image close to the one of the full protocol.

It is worth mentioning that compared to the first two tomographies, the number of measurements of these optimized protocols is near the actual 25%, 50% and 75% of the full protocol (2561 measurements) because no electrodes were skipped, so fewer data points were eliminated. These optimized datasets provide more accurate results with less artefacts than those of the first tomography. Since the optimized models are produced before the investigation, caution must be taken not to overestimate the number of measurements available after data processing. These results suggest that all these optimized models could be used to have a general overview of the investigated area.

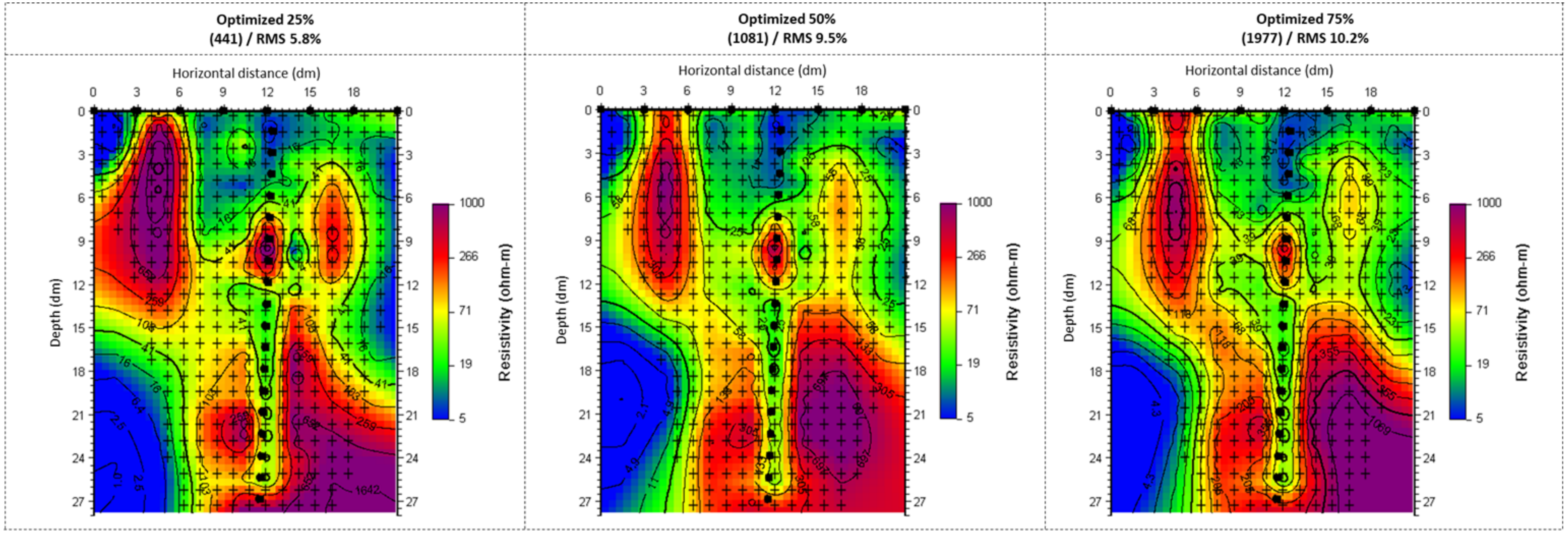

Optimized 25%
(441) / RMS 5.8%

Optimized 50%
(1081) / RMS 9.5%

Optimized 75%
(1977) / RMS 10.2%

Figure 5.19: Inverted results of the optimized protocols of ~25%, 50% and 75% of the full protocol. On top of each image, the number of measurements used for the inversion and the RMS error is referred. The crosses on the optimized models represent the area of high sensitivity appointed by the threshold value that deemed more appropriate for this geometry.

5.2 Concluding remarks

Considering all the above, it can be said that the designed algorithm can produce full and optimized protocols capable of supporting measurements between borehole-surface and borehole-borehole arrays. The user can modify different parameters to obtain the final protocols. According to the tested synthetic models, experimental models and real data, the following conclusions can be conducted:

- The threshold, which is added to the norm of the Jacobian and was supposed to show the trusted area of the model, does not seem to affect the inversion significantly since some targets of the synthetic models were detected. However, they were out of the trusted area. For this reason, the threshold is only valuable in determining the most appropriate trusted area for a specific geometry.
- The results suggest that no universal threshold value would indicate the trusted area of every possible geometry and environment. This value differs for every case and can only be decided empirically. An investigation using synthetic models is recommended.
- The final number of measurements of the optimized protocols depends on the number of measurements of the full protocol. More specifically, three percentages are available: the 25%, 50% or 75% of the full protocol. The 50% and 75% optimized datasets provided better results in most examined models, producing results quite close to the full protocols. In most cases, the optimized protocols of 25% showed increased artefacts even though they could provide a general overview of the examined area.
- In real data, where some of the electrodes were skipped due to technical issues, or some measurements were eliminated due to the process, sometimes the resulting number of measurements of the optimized datasets is not approximately 25%, 50% or 75% of the full protocol. This happens because the protocols were created before the measurement, considering all the available electrodes.

REFERENCES

Almpanis, A. (2018). *Cross-hole electrical resistivity tomography: Application of different electrode configurations within boreholes* (Master Thesis). Aristotle University of Thessaloniki.

Bing, Z., & Greenhalgh, S. (2000). Cross-hole resistivity tomography using different electrode configurations. *Geophysical Prospecting*, *48*, 887–912.

Dahlin, T., & Zhou, B. (2004). A Numerical Comparison of 2D Resistivity Imaging with Ten Electrode Arrays. *Geophysical Prospecting*, *52*, 379–398.

Ducut, J. D., Alipio, M., Go, P. J., Vicerra, R. R., Bandala, A., & Dadios, E. (2022). A Review of Electrical Resistivity Tomography Applications in Underground Imaging and Object Detection. *Displays*, *73*, 102208.

Fehdi, C., Nouioua, I., Belfar, D., Djabri, L., & Salameh, E. (2014). Detection of Underground Cavities by Combining Electrical Resistivity Imaging and Ground Penetrating Radar Surveys: A Case Study from Draa Douamis Area (North East of Algeria). *Environmental Earth Sciences*.

Goes, B. J. M., & Meekes, J. A. C. (2004). An Effective Electrode Configuration for the Detection of DNAPLs with Electrical Resistivity Tomography. *Journal of Environmental and Engineering Geophysics*, *9*, 127–141.

Griffiths, D. H., & Barker, R. D. (1993). Two-dimensional resistivity imaging and modelling in areas of complex geology. *Journal of Applied Geophysics*, *29*, 211–226.

Kim, J. H. (2017). *DC2DPro – User's Manual, KIGAM, KOREA.*

Leontarakis, K., & Apostolopoulos, G. V. (2013). Model Stacking (MOST) technique applied in cross-hole ERT field data for the detection of Thessaloniki ancient walls' depth. *Journal of Applied Geophysics*, *93*, 101–113.

Loke, M. H., & Barker, R. D. (1995). Least-squares deconvolution of apparent resistivity pseudosections. *GEOPHYSICS*, *60*, 1682–1690.

Loke, M. H., Wilkinson, P. B., Uhlemann, S. S., Chambers, J. E., & Oxby, L. S. (2014). Computation of optimized arrays for 3-D electrical imaging surveys. *Geophysical Journal International*, *199*, 1751–1764.

Martorana, R., Capizzi, P., D'Alessandro, A., & Luzio, D. (2017). Comparison of different sets of array configurations for multichannel 2D ERT acquisition. *Journal of Applied Geophysics*, *137*, 34–48.

Menke, W. (2018). In *Geophysical Data Analysis* (pp. 71–90). Academic Press.

Noel, M., & Xu, B. (1991). Archaeological investigation by electrical resistivity tomography: A preliminary study. *Geophysical Journal International*, *107*, 95–102.

Samouëlian, A., Cousin, I., Tabbagh, A., Bruand, A., & Richard, G. (2005). Electrical resistivity survey in soil science: A review. *Soil and Tillage Research*, *83*, 173–193.

Schmidt-Hattenberger, C., Bergmann, P., Labitzke, T., Wagner, F., & Rippe, D. (2016). Permanent crosshole electrical resistivity tomography (ERT) as an established method for the long-term CO2 monitoring at the Ketzin pilot site. *International Journal of Greenhouse Gas Control*, *52*, 432–448.

Sikandar, P., & Christen, E. (2012). Geoelectrical Sounding for the Estimation of Hydraulic Conductivity of Alluvial Aquifers. *Water Resources Management*, *26*.

Stummer, P., Maurer, H., & Green, A. G. (2004). Experimental design: Electrical resistivity data sets that provide optimum subsurface information. *Geophysics*, *69*.

Tsourlos, P. (1995). *Modelling, interpretation and inversion of multielectrode resistivity survey data.* (Phd, University of York). University of York.

Tsourlos, P., Ogilvy, R., Papazachos, C., & Meldrum, P. (2011). Measurement and inversion schemes for single borehole-to-surface electrical resistivity tomography surveys. *Journal of Geophysics and Engineering*, *8*, 487–497.

Wilkinson, P. B., Chambers, J. E., Lelliott, M., Wealthall, G. P., & Ogilvy, R. D. (2008). Extreme sensitivity of crosshole electrical resistivity tomography measurements to geometric errors. *Geophysical Journal International*, *173*, 49–62.

Wilkinson, P. B., Chambers, J. E., Meldrum, P. I., Ogilvy, R. D., & Caunt, S. (2006). Optimization of array configurations and panel combinations for the detection and imaging of abandoned mineshafts using 3D cross-hole electrical resistivity tomography. *Journal of Environmental and Engineering Geophysics*, *11*, 213–221.

Αθανασίου, Ε. Ν. (2009). *Ανάπτυξη αλγόριθμων για τη βέλτιστη στρατηγική μέτρησης και αντιστροφής δεδομένων ηλεκτρικής τομογραφίας.* (Διδακτορική Διατριβή). Αριστοτέλειο Πανεπιστήμιο Θεσσαλονίκης.

Λούβαρης, Π. Κ. (2020). *Μελέτη βέλτιστων μετρήσεων ηλεκτρικής τομογραφίας με διατάξεις ηλεκτροδίων τοποθετημένων στον τρισδιάστατο χώρο.* (Μεταπτυχιακή εργασία). Αριστοτέλειο Πανεπιστήμιο Θεσσαλονίκης.

Σιμυρδάνης, Κ. Α. (2013). *Ανάπτυξη τομογραφικών γεωφυσικών τεχνικών για τη μελέτη γεωτεχνικών και περιβαλλοντικών προβλημάτων.* (Διδακτορική Διατριβή). Αριστοτέλειο Πανεπιστήμιο Θεσσαλονίκης.